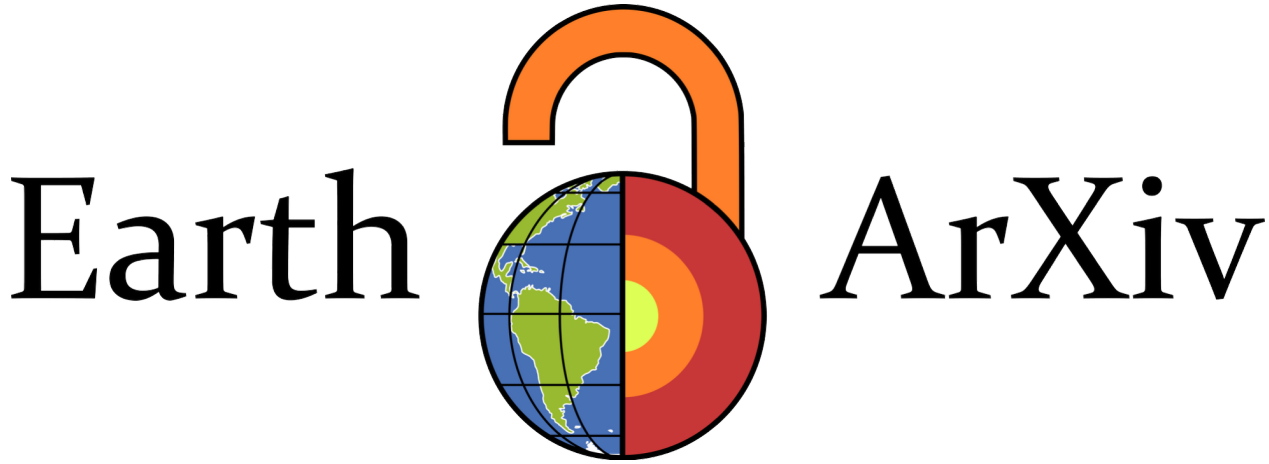

AUTHORS LIST: Neubeck A[1], Loukola-Ruskeeniemi K[2], Cameron V.[1], Rösel D.[3], Roud, S.[4], Jonathan A. Lewis[1], John Manrique Carreño[1], Buczko D[1], Bohlin M[5], Tranchet P-A[6], Almqvist B.[1]

[1]Department of Earth Sciences, Uppsala University, Sweden
[2]Geological Survey of Finland
[3]Department of Earth Sciences, University of Gothenburg, Sweden
[4]GFZ Helmholtz Center for Geosciences, Telegrafenberg, 14473 Potsdam, Germany
[5]Department of geological Sciences, Stockholm University, Sweden
[6]Institute of Geology, University of Hamburg, Germany

Nickel Isotope Systematics in the Talvivaara Paleoproterozoic Black Shale Deposit Reveal Mineralogy-Controlled Fractionation with a Preserved Biogenic Signal

Neubeck A[1], Loukola-Ruskeeniemi K[2], Cameron V.[1], Rösel D.[3], Roud, S.[4], Jonathan A. Lewis[1], John Manrique Carreño[1], Buczko D[1], Bohlin M[5], Tranchet P-A[6], Almqvist B.[1]

[1]Department of Earth Sciences, Uppsala University, Sweden
[2]Geological Survey of Finland
[3]Department of Earth Sciences, University of Gothenburg, Sweden
[4]GFZ Helmholtz Center for Geosciences, Telegrafenberg, 14473 Potsdam, Germany
[5]Department of geological Sciences, Stockholm University, Sweden
[6]Institute of Geology, University of Hamburg, Germany

Abstract

Nickel isotope systematics in sediment-hosted sulfide deposits are now more commonly used to infer redox and diagenetic processes, yet their potential to record biological signals and their preservation through diagenesis and metamorphism remains poorly constrained. Here we present micro-scale coupled δ^{60}Ni, δ^{34}S, δ^{13}C, REE pattern, and paleoproductivity proxy data from the Paleoproterozoic Talvivaara Ni-Zn-Cu-Co deposit, a ~2.1-1.9 Ga black shale associated with the Shunga Event at the end of the Great Oxidation Event. Our data potentially reveals how biological signals are selectively preserved or overprinted by mineralogical reorganization. The deposit is hosted by graphite-sulfide schists representing metamorphosed black shales deposited in a restricted, anoxic to euxinic basin and subsequently altered to upper-greenschist- to amphibolite-facies conditions. Through most of the drill core, Ni isotope systematics are governed by the pyrite-pyrrhotite-pentlandite reaction series where pyrite consistently hosts isotopically heavier Ni than coexisting pyrrhotite. This reflects mineralogy-controlled fractionation during diagenetic sulfidization and recrystallization. The heaviest δ^{60}Ni values in pentlandite-bearing intervals occur at depth, marking late-stage metamorphic Ni redistribution, with comparably heavy values also recorded in shallow pyrite-dominated domains through a distinct mineralogical control. In contrast, a discrete interval at 118.68-152.27 m depth preserves a coherent biogenic overprint, where coupled shifts toward light δ^{60}Ni (-0.43 to -0.03‰), strongly negative δ^{34}S (-10 to -13‰), elevated organic carbon contents, HREE-dominated REE patterns, strong P-Ni coupling, and anomalous paleoproductivity proxies collectively record intensified microbial sulfate reduction and organic matter degradation. While the multi-proxy convergence supports a biogenic interpretation, the δ^{60}Ni values alone overlap with abiogenic ranges, and the possible contribution of metal-dependent anaerobic oxidation of methane to Fe-S-Ni systematics in the deeper intervals cannot be excluded. Magnetic susceptibility independently confirms that this excursion reflects early diagenetic sulfide precipitation rather than metamorphic recrystallization or hydrothermal overprint. To our knowledge, this is the first direct micro-scale evidence for a preserved biogenic δ^{60}Ni signature in Paleoproterozoic black shales. These results demonstrate that bulk analyses systematically average over mineralogically distinct Ni pools, destroying transient biological

signals that are recoverable only through micro-scale, mineralogically resolved multi-proxy analysis.

1. Introduction

The Talvivaara Ni-Zn-Cu-Co deposit is located in eastern Finland near the Archaean-Proterozoic boundary (Figure 1). The basal layers consist of Archaean granites and granitoids, overlain by 2.1 Ga quartzite and arkose beds, succeeded by massive black shale sequences interlayered with calcium-silicate rock veins and capped by metaturbidites and mica schists (Loukola-Ruskeeniemi and Heino 1996). Between 2.10 Ga and 2.05 Ga, clastic sediments accumulated in a continental margin rift basin, devoid of syn-rift magmatic elements but with intercalated mafic and volcanic rocks (Kontinen and Hanski 2015; Loukola-Ruskeeniemi and Lahtinen 2013). Between 2.0 Ga and 1.95 Ga, extensional tectonics facilitated deposition of organic-rich black shales in a shallow, restricted, euxinic basin. Rifting caused significant thinning of the Archaean crust, ultimately exposing the lithospheric mantle and enabling formation of oceanic crust with pillow lavas erupted onto the exhumed basement. The Svecofennian orogeny subsequently influenced the region through ductile deformation and turbidite deposition. Rb-Sr dating (Pašava et al. 2019) constrains the age of the black shales to 2.1-1.9 Ga, associated with the global Shunga event marking the conclusion of the Great Oxidation Event (Melezhik et al. 2005). Subsequent metamorphism at 1.91-1.78 Ga altered the rocks to upper greenschist or amphibolite facies (Kontinen and Hanski 2015). Hydrothermal fluids derived from underlying volcanic activity introduced dissolved Fe and Ni into the basin (Loukola-Ruskeeniemi and Lahtinen 2013; Young et al. 2013), where reducing conditions facilitated precipitation of pyrrhotite, pentlandite, and fine-grained pyrite containing up to 0.5% Ni. The combination of metal-rich hydrothermal fluids, anoxic bottom waters, and organic-rich sediments resulted in a disseminated, sediment-hosted Ni deposit rather than a massive sulfide accumulation (Loukola-Ruskeeniemi and Heino 1996; Kontinen and Hanski 2015).

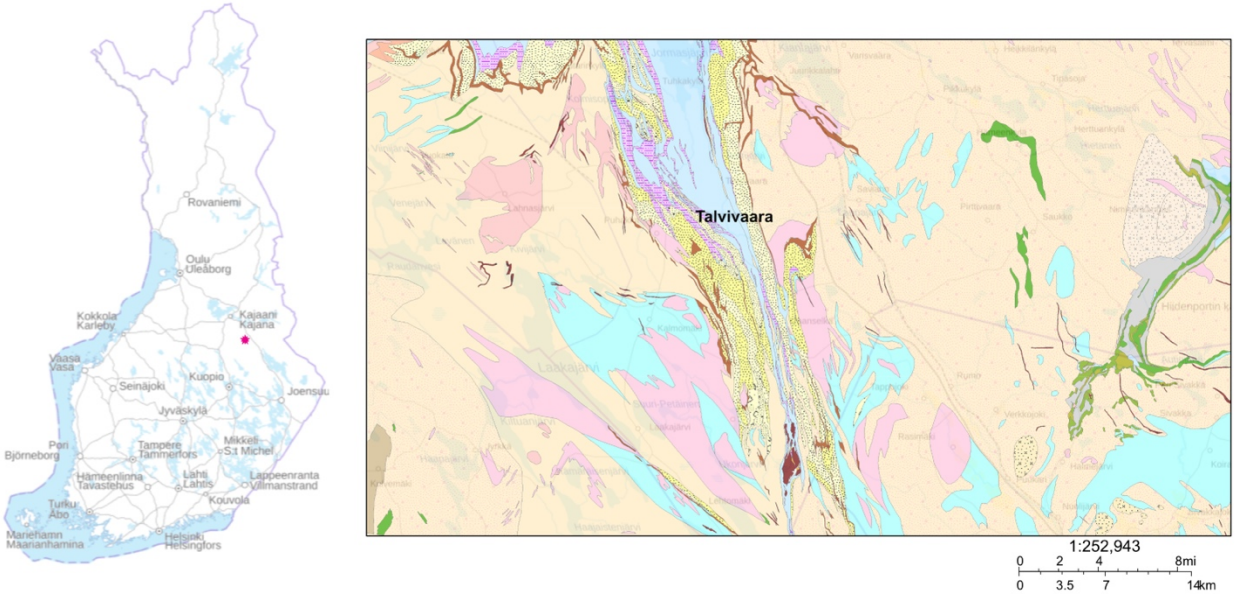

Fig. 1. *Map of Finland with Talvivaara marked with a red star (left) and a bedrock map of the Talvivaara outcrop (right. Bedrock geology was modified from the digital bedrock map database of Finland – DigiKP @ Geological Survey of Finland.*

Despite decades of geochemical study of Paleoproterozoic black shales, the conditions under which primary biological signals survive diagenesis and metamorphism in sulfide-rich systems remain poorly constrained. The Talvivaara Ni-Zn-Cu-Co deposit offers a uniquely tractable entry point into this problem. Its exceptional Ni enrichment, well-documented mineralogy, and association with the Shunga Event make it an ideal system in which to investigate the competing mineralogical and biological controls on Ni isotope systematics at the micro-scale. The deposit has been extensively characterized geologically and geochemically (Loukola-Ruskeeniemi and Heino, 1996; Loukola-Ruskeeniemi and Lahtinen, 2013; Kontinen and Hanski, 2015; Pašava et al., 2019), providing the mineralogical and stratigraphic framework needed to interpret isotopic data at the mineral scale rather than in bulk.

This study tests whether Ni isotope systematics in the Talvivaara black shales are controlled by mineralogical processes, particularly the diagenetic and metamorphic transformation of the pyrite-pyrrhotite-pentlandite assemblage, or by primary biological and hydrothermal inputs, and whether these signals can be distinguished at the micro-scale. Despite amphibolite-facies metamorphism, the exceptional Ni enrichment and well-constrained mineralogy of the deposit provide a rare opportunity to assess whether biogenic δ^{60}Ni signals are preserved, and under what conditions. The outcome of this study has thus direct implications for the use of Ni isotopes as biosignatures in ancient metamorphosed sedimentary systems.

2. Samples and Methods

The samples were selected from the southern Kuusilampi ore body, drill core 3344:329 (GTK-329 , Loukola-Ruskeeniemi and Lahtinen 2013). A total of 11 sample depths were investigated for δ^{60}Ni (Table 1). Of these, 9 depths yielded micromilled δ^{60}Ni analyses and 6 bulk analyses (Table 1, Fig.2); all 11 depths were analyzed for bulk Ni concentrations and geochemical proxies (Table 1). Two depths were analyzed for δ^{34}S by SIMS (Fig. 2), 7 depths for δ^{13}C and C% by EA-IRMS (Fig.3), and 9 depths for trace and major elements including REEs by LA-ICP-MS (Table S1, S2). EPMA point profiles and mineralogy were obtained for selected depths across the full core interval (Table S3, S4, Fig S1-S7).

2.1 Electron Microprobe Analysis (EPMA)

Polished rock pucks were prepared from the samples for mineral identification using optical microscopy. Mineral chemistry and elemental distribution were analyzed with a Jeol JXA8530F Hyperprobe Field Emission Electron Probe Microanalyzer (EPMA) at Uppsala University, Sweden. Point analyses (in profiles) using Wavelength-dispersive X-Ray Spectroscopy (WDS) were conducted with a 10 nA beam current, 15 kV accelerating voltage, and 10 s peak/5 s background counting times at beam diameter of 5 μm. Chemical composition maps were generated also with WDS at 15 kV accelerating voltage, 40 nA beam current, 100 ms dwell time, 4×4 μm step size, and 4 μm beam diameter. All WDS analyses were standardized using wollastonite (for Ca, Si), pyrophanite (for Mn), hematite (for Fe), NiO (for Ni), MgO (for Mg). Achieved detection limit ranges (in ppm, based on results from points analyses in profiles) were: 25-48 for Ca, 61-108 for Si, 72-96 for Mn, 68-96 for Fe, 66-85 for Ni and 34-55 for Mg.

2.1.1 Scanning Electron Microscope - energy dispersive spectrometer (SEM - EDS)

Imaging was conducted at Uppsala University, Sweden, an XL30 Scanning Electron Microscope (SEM) equipped with a field emission gun (XL30 SEM-FEG), an Oxford x-act energy dispersive

spectrometer (EDS), a backscatter electron (BSE) detector, and a secondary electron (SE) detector. All analyses were performed on uncoated samples.

2.2 δ^{60}Ni and δ^{34}S

Sample preparation (micromilling), purification, and isotope analyses followed the procedure described in Gueguen et al. (2013) and Neubeck et al. (2025). Rock powders were digested in mixed acids and spiked with a $^{61}Ni/^{62}Ni$ double spike to correct for instrumental mass bias and chemical fractionation. Nickel was purified using Ni-spec resin with dimethylglyoxime complexation (Gueguen et al. 2013), achieving near-quantitative yields. Isotope ratios were measured at Ifremer Centre de Bretagne (Brest, France) using a Thermo Scientific Neptune MC-ICP-MS, with NIST SRM 986 as the bracketing standard, BHVO-2 as secondary reference, and monitoring of Cu isobaric interferences (Moynier et al. 2007; Fujii et al. 2011; Gueguen et al. 2013; Neubeck et al. 2025). External reproducibility is better than ±0.1‰ (2SE) for samples >0.03 ppm Ni. The long-term external reproducibility of the method, assessed by repeated analysis of NIST SRM 986 processed through the full double-spike procedure across all measurement sessions, was ±0.09‰ (2SD, n = 66). Nickel isotope compositions are reported in δ^{60}Ni notation relative to NIST SRM 986:

$$\delta^{60}Ni\ (‰) = [(^{60}Ni/^{58}Ni_{sample})/(^{60}Ni/^{58}Ni_{SRM986})]* 1000 \qquad \text{Equation 1}$$

The data presented in this study are described using the $^{60}Ni/^{58}Ni$ ratio given as δ^{60}Ni. The Ni isotope compositions of samples were then calculated using the double spike calculation template from Gueguen et al. (2013). The NIST SRM 986 standard was passed through columns four separate times, yielding an average value and external reproducibility for the method.

In situ sulfur isotope analyses were made using the NORDSIM Ion Microprobe (Cameca IMS 1280, 10 µm lateral beam dimension, 1–2 µm depth dimension) at the Department of Geosciences, Swedish Museum of Natural History. The polished samples were mounted on a stainless-steel sample holder; sulfur isotope analyses targeted pyrite and pyrrhotite grains identified by prior EPMA mapping and were examined with SEM prior to Microprobe analysis. Data were normalized for instrumental mass fractionation using matrix-matched reference materials (Balmat and Ruttan for pyrites) which were mounted together with the sample mounts and analysed after every sixth sample analysis. Results are reported as per mil (‰) δ^{34}S.

2.3 δ^{13}C

Micromilled powders from sulfide and silicate microdomains were analyzed for δ^{13}C and total carbon (TC) using a Flash Elemental Analyzer coupled to a Thermo Fisher Delta V Advantage isotope ratio mass spectrometer (EA-IRMS) at Stockholm University Stable Isotope Laboratory. Approximately 0.2 mg of powder was used per analysis. International standards NBS-18, IAEA-CO-8, and IAEA-603 were measured every tenth sample; long-term reproducibility is ±0.08‰. In-house standards Merck $CaCO_3$ and Carm yielded reproducibilities of ±0.12‰ and ±0.08‰, respectively. Results are reported in δ^{13}C notation (‰) relative to VPDB, where $\delta^{13}C = (R\_sample / R\_standard - 1) \times 1000$ and $R = {}^{13}C/{}^{12}C$. Analytical reproducibility based on repeated standard measurements was ±0.06‰. Total carbon is expressed as weight percent of initial sample mass.

2.4 LA-ICP-MS elemental Analyses

LA-ICP-MS/MS analyses were performed using an ESI NWR 213 laser ablation system coupled to an Agilent 8800 triple quadrupole ICP-MS/MS at the Microgeochemistry Laboratory, Department of Earth Sciences, University of Gothenburg. Analyses were conducted during two analytical sessions (251117 and 251118) using identical laser ablation and ICP-MS/MS settings. Reference materials and samples were ablated using a spot diameter of 40 µm, a repetition rate of 10 Hz, and a laser fluence of 5.6 J cm^{-2}. Background signals were collected for 18 s prior to 40 s of ablation and followed by a 22 s wash-out period. Helium was used as the carrier gas (750 mL min^{-1}) and was mixed with nitrogen (4 mL min^{-1}) and argon (780 mL min^{-1}) before introduction into the ICP-MS. Nitrous oxide (N_2O) was used as the reaction gas. Lens settings, analyzed isotopes, and corresponding dwell times are summarized in Table S5 in the Supplementary Information. Primary and secondary reference materials were routinely analyzed and bracketed with between nine to seventeen unknown analyses.

Trace-element mass fractions were calculated using the X_Trace_Element_IS data reduction scheme implemented in *Iolite* version 3.75 (Paton et al. 2011). NIST SRM 610 (Jochum et al. 2011) was used as the primary reference material for major and trace elements in Si-dominated phases (e.g., silicate matrix), with Si used as the internal standard. All elements were assumed to occur as oxides, except Fe and Mn, which were assumed to occur as sulfides. The total mass fractions (oxides plus Fe, Mn, and S) were normalized to 95 wt%, allowing for an additional 5 wt% H_2O. The reference glasses BCR-2G and BHVO-2G (Jochum et al. 2005; Jochum et al. 2007) were used as secondary reference materials to monitor analytical accuracy (see Table S5).

For S-dominated spots, the reference material Po725 (measurement session 251117) or MASS-1 (measurement session 251118) (Wilson et al. 2002) was used as the primary reference material, in conjunction with BCR-2G (Jochum et al. 2005). Po725 or MASS-1 was used to determine the relative Fe/S proportion, whereas BCR-2G was used to quantify all other major and trace elements using Fe as the internal standard. In a second step, all elements were normalized to 100 wt%, including the Fe/S ratio determined from Po725 or MASS-1, to calculate the sulfur mass fraction. Po725 was additionally analyzed during measurement session 251118 as a secondary reference material to assess the accuracy of the Fe/S ratio, whereas a laboratory-internal chalcopyrite standard was used during session 251117 (see Table S5). Because BCR-2G does not contain sulfur, this two-step approach was required. In addition, BCR-2G contains higher Fe and Mn concentrations than NIST SRM 610 and is therefore better suited for Fe- and Mn-rich phases. BHVO-2G (Jochum et al. 2005; Jochum et al. 2007) was used as a secondary reference material to assess analytical accuracy for all other elements.

Some ablation signals showed evidence of inclusions; where possible and where the signal remained stable for several seconds, multiple ablation intervals were defined for a single spot. Uncertainties are reported at the 2 SE level and include only random uncertainties related to signal variability. Note that due to poor signal stability in some spots, the associated 2 SE uncertainties are relatively large (see Table S5).

2.5 Magnetic susceptibility

Magnetic susceptibility measurements at room temperature were performed at Uppsala University, Sweden using an AGICO MFK1-FA magnetic susceptibility meter (agico.cz). Measurements were conducted with field intensities ranging from ~5 A/m up to 700 A/m, using a set frequency of the alternating field at 975 Hz. The magnetic field intensities in units of A/m were subsequently converted into units of microtesla (µT), with the converted units used

as proxy for grain size, shown in Figure 5 (to enable comparison with the control experiments of Worm et al. 1993).

2.6 Raman spectroscopy

The indigenous origin and thermal maturity of carbonaceous material were assessed on selected samples by Raman spectroscopy using a EZRaman-I-Dual analyzer (Enwave Optronics) at Uppsala University. Spectra were acquired using a 532 nm laser on carbonaceous phases identified by optical microscopy and EPMA, targeting areas free of sulfide interference. The laser power was set to 1-5mW, with 20s integrations per spectrum. The presence or absence of modern organic contamination was evaluated based on the characteristic band structure of carbonaceous material: modern and recently deposited organic matter produces a prominent D1 defect band (~1350 cm^{-1}) of intensity comparable to or exceeding the G graphite band (~1580 cm^{-1}), whereas thermally mature Paleoproterozoic carbonaceous material yields G/D1 ratios greater than 1, reflecting advanced structural ordering during metamorphism. G/D1 ratios substantially exceeding 1 indicate a well-ordered graphitic structure inconsistent with recently deposited organic matter, which typically produces D1 intensities comparable to or exceeding G.

2.7 Data processing

Nickel enrichment factors were calculated using equations 2 and 3, employing the local lithogenic baseline of 15.25 derived from Pašava et al. (2019), reflecting the mean geochemical signature of 12 low-TOC, low-sulfur schist samples from the Kainuu Schist Belt. EF values >1 suggests authigenic enrichments and values <1 authigenic depletion (Eq. 2). The proportion of Ni attributed to non-detrital (authigenic) sources, Ni~auth~, is a proxy for authigenic enrichment: it represents the fraction of total Ni in excess of the amount contributed by detrital material, estimated by normalization to Al and Ti concentrations of the upper continental crust (Rudnick and Gao 2003). The Ni excess (Ni_{xs}) was calculated according to Equation 3 and is also based on Pašava et al. 2019, where the same lithogenic background value is used as the local shale value and where Al is used as a normalizing element. Ni_{xs} is expressed in ppm in Table 1.

$$EF\_Ni = (Ni/Al)_{smpl}/(Ni/Al)_{ref} \quad \text{Equation 2}$$

$$Nixs = Ni_{smpl} - Al_{smpl} * (Ni/Al)_{ref} \quad \text{Equation 3}$$

Following Pašava et al (2019), the Ni detrital fraction (Ni_{detr}, %) was estimated using both Ti and Al concentrations, normalized to the composition of the upper continental crust (UCC) as follows: Ni_{detr} = 121.67 × Ti_sample and Ni_det = 5.77 × Al_sample, where 121.67 and 5.77 represent the Ni/Ti and Ni/Al ratios in UCC, respectively (Rudnick and Gao 2003). The average of the two Ni_{detr} estimates was subtracted from the total Ni content to obtain the authigenic nickel fraction (Ni_{auth}). Niauth (%) was then expressed as (Niauth_ppm / Ni_sample) × 100.

The biological fraction of Ni is calculated following the method described by Pašava et al. (2019) and Little et al. (2015), where Ni_{BIO} represents the amount of Ni taken up by a 'standard' phytoplankton, defined as 37 ppm by Little et al. (2015). Ni_{BIO} is calculated as the product of TOC and $Ni_{plankton}$, and its contribution to Ni_{XS} is expressed as the quotient of Ni_{BIO} divided by Ni_{XS}.

To evaluate the contribution of hydrothermal versus detrital components, we calculated the elemental ratios Al/(Al + Fe + Mn) and (Fe + Mn)/Ti, which have been widely used as indicators

of hydrothermal sedimentation (Marchig et al. 1982; Boström 1983; Dias and Barriga 2006; Slack et al. 2009; He et al. 2016; Liao et al. 2018; Lim et al. 2022). The metalliferous index, Al/(Al + Fe + Mn), decreases with increasing hydrothermal input, with pelagic deep-sea sediments typically >0.4 and metal-enriched hydrothermal sediments <0.4 (Boström 1973; Boström 1983). Conversely, high (Fe + Mn)/Ti values indicate authigenic enrichment of Fe and Mn relative to detrital inputs. These ratios, together with ternary plots of Al–Fe–Mn and Si/Al ratios, allow discrimination between hydrothermal, volcaniclastic, and pelagic components, and can be used to quantify the degree of hydrothermal influence in the studied sediments (Dias and Barriga 2006; Liao et al. 2018). In combination, the Ni fractionation approach and the elemental discrimination proxies provide a framework to distinguish detrital, biological, and authigenic (including hydrothermal) contributions to Ni in ancient deep-sea sediments (Lim et al. 2022).

3. Results

3.1 EPMA

The elemental composition of targeted grains at each depth are presented in Table S3.

3.1.1 Elemental spot analyses

The mineralogical composition (Table S3, S4) of the core samples is dominated by pyrite and pyrrhotite between depths of 82 m and 172 m. Pyrite is absent in the deeper intervals (204 m, 237 m, and 272 m), while pentlandite appears in the two deepest samples. Chalcopyrite, sphalerite, and alabandite are present throughout the entire core. The sulfide minerals are embedded within a silicate matrix and are commonly associated with quartz veins. Figure S1 illustrates several features. In the shallowest samples, pyrite occurs as fine-grained crystals (<30 μm), initially formed as framboids and micro-agglomerates that were subsequently metamorphosed. Pyrrhotite in these intervals is commonly found in close association with euhedral pyrites. Framboidal pyrite morphology of the type observed here is commonly associated with biogenic sulfide precipitation under euxinic conditions, as rapid nucleation driven by microbial H_2S production favours the formation of small, spheroidal aggregates (Rickard 2014). However, abiogenic framboid formation is also documented, and morphology alone is insufficient to establish a biological origin without additional textural or geochemical evidence. No other definitive biosignature microstructures, such as mineralized cell walls or organically templated fabrics, were identified in the EPMA or SEM imaging beyond organic carbon associations and fine-grained sulfides. In the deepest samples (237 m and 272 m), chalcopyrite and pyrrhotite dominate, with pentlandite observed along the boundaries of pyrrhotite crystals, forming localized crack infillings (Figure S1).

Spearman correlation plots for Ni vs Mn, Fe, S and P show a moderately strong negative correlation between Ni and Mn and a strong positive correlation with Ni and Fe (Fig. S2) as also shown by LA-ICP-MS data (Fig.7). The correlation between Ni and S varies from mostly positive but shifts to a negative correlation at depth between 120 and 150m. The opposite effect can be observed with P, where a weakly negative correlation shifts towards a strongly positive correlation at the same depth range (Fig. S2).

3.1.2 EPMA Chemical maps

The elemental maps show that Ni is not associated with Mn and occurs almost exclusively in pyrite and pyrrhotite (Fig. S3-7). Where pyrrhotite and pyrite coexist, Ni is consistently enriched in, or crosscuts, pyrrhotite (Fig. S4) and is also concentrated along the margins of the pyrrhotite grains. Ni remains almost entirely dissociated from Mn in all mapped areas.

3.2 Nickel and sulfur isotopes

The δ^{60}Ni isotopic values of the micromilled sites range from -0.43 ± 0.05 to +0.72 ± 0.03‰, with the lightest values (down to -0.43 ± 0.05‰) occurring within the 118.68-152.27 m interval (Table 1, Fig. 2). The δ^{34}S isotopic values range between -13.86 ± 0.05‰ and +10.23 ± 0.07‰ (Fig. 2, Table S6).

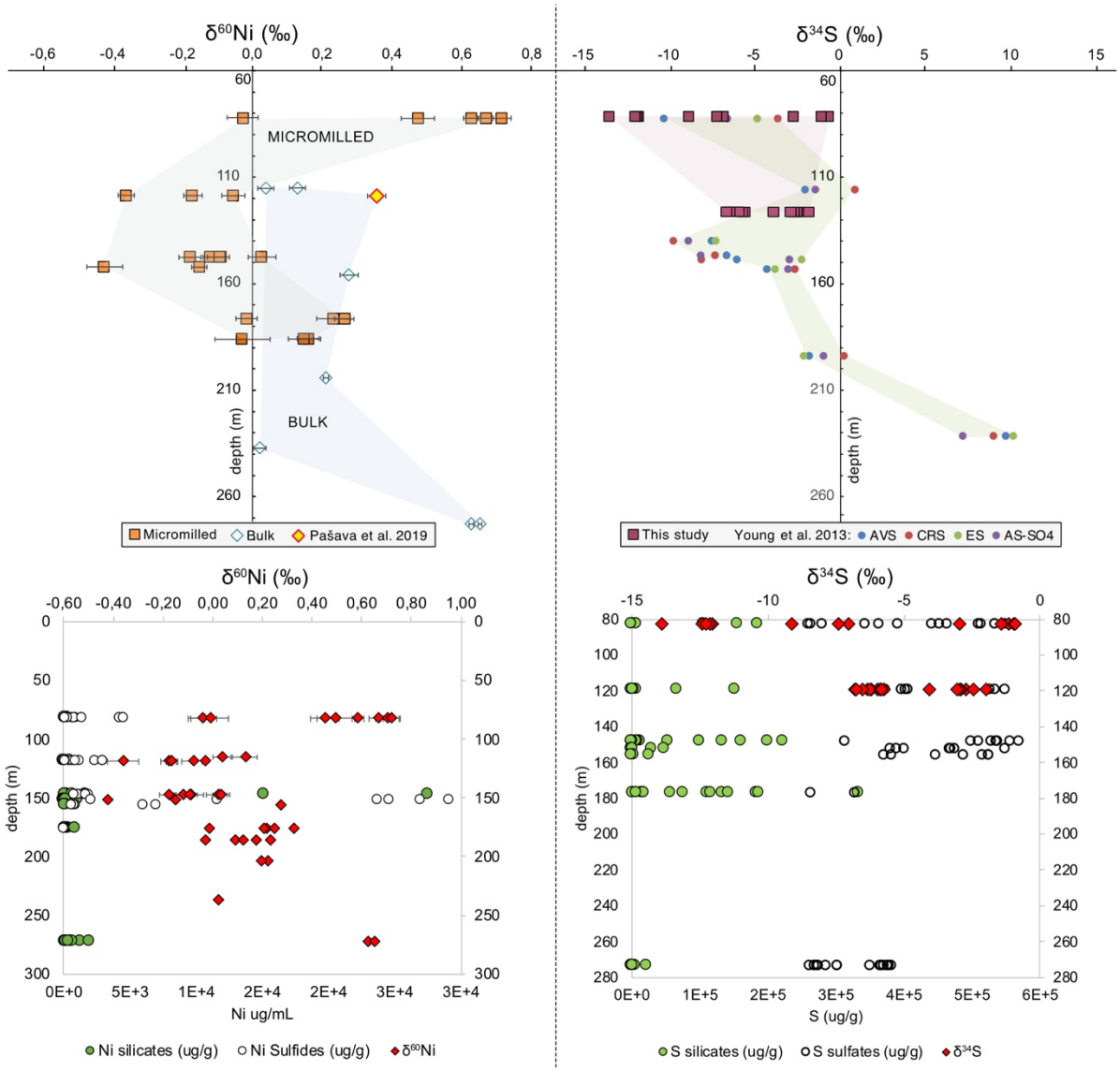

Fig.2. *Upper left panel: the distribution of δ^{60}Ni in the samples downcore of 3344:329, GTK-329, where open markers represent bulk analyses and filled markers micromilled samples. The filled diamond represents measured bulk values by Pašava et al. 2019* (Pašava et al. 2019). *Upper right panel: distribution of δ^{34}S in the samples downcore of 3344:329, GTK-329, where large squares represent in situ analyses from this study (error bars smaller than the symbols) and smaller markers represent bulk data from Young et al. (2013. AVS=Acid-volatile sulfur, CRS=Chromium-reducible sulfur, AS-SO_4=Acid-soluble sulfate, ES=Elemental sulfur. The gray area marks the depth range with the lightest δ^{60}Ni values. Lower left panel: Concentration of Ni in silicates and*

sulfides (µg/g) and δ^{60}Ni (‰) as a function of depth (m). Lower right panel: Concentration of S in silicates and sulfides(µg/g) and δ^{34}S (‰) as a function of depth (m).

Table. 1. *Sample results where *=Ni concentrations measured on each sample prior to isotopic measurements and the **=the measured bulk data* (Loukola-Ruskeeniemi and Heino 1996) *and ***=measured at the Swedish Museum of Natural History and where Ni concentration data are missing*

Sample id	Depth	δ60Ni (‰)	2σ	Ni(ppm) * MICRO MILLED	Ni(ppm) ** BULK	Ni (ppm) Sulfides (LA-ICP-MS) AVERAGE	Ni (ppm) Silicates (LA-ICP-MS) AVERAGE	Niauth (%)	Nidetr (%)	V/Cr	EF_Ni	Nixs	Fraction NiBIO contribution to Nixs
3344/329/84,4	82,4	-0,01	0,07	0,202	796	1077±19.8	68±6.3	98,4	1,6	9,1	3	768	3,28
	82,4	-0,04	0,06	0,199									
	82,4	0,59	0,03	0,104									
	82,4	0,67	0,04	0,104									
	82,4	0,50	0,07	0,100									
	82,4	0,45	0,06	0,094									
	82,4	0,71	0,05	0,151									
	82,4	0,72	0,03	0,140									
3344/329/115,4	115,4	0,038	0,095										
	115,4	0,130	0,019		2970			98,4	1,6	38,3	3	2870	1,96
3344/329/118,68	118,68	-0,08	0,02	0,120	892	1192±14.7	72±8.4	98,9	1,1		4	870	1,19
	118,68	-0,03	0,06	0,120									
	118,68	-0,17	0,04	0,156									
	118,68	-0,18	0,04	0,156									
	118,68	-0,36	0,02	0,475									
3344/329/147,55	147,55	0,03	0,05	0,173									
	147,55	0,02	0,06	0,173									
	147,55	-0,12	0,05	0,283									
	147,55	-0,09	0,01	0,511									
	147,55	-0,18	0,03	0,734									
	147,55	-0,09	0,02	1,519		1334±41.1	1776±301						
3344/329/152,27	152,27	-0,43	0,05	0,613	4866	21486±896.0	105±15.5	99,2	0,8	6,4	5	4767	2,30
	152,27	-0,15	0,02	1,166									
3344/329/176,55	176,55	0,22	0,09	0,185	1080	15±4.3	148±8.0	96,7	3,3	15,4	1	990	1,70
	176,55	0,25	0,04	0,185									
	176,55	0,20	0,05	0,110									
	176,55	0,32	0,03	0,110									
	176,55	-0,02	0,03	0,567									
3344/329/186,15	186,15	0,23	0,06	0,113	610			96,2	3,8	5,1	1	551	1,09
	186,15	0,09	0,04	0,113									
	186,15	0,12	0,07	0,230									
	186,15	0,17	0,06	0,230									
	186,15	-0,03	0,08	2,600									
3344/329/204,4	204,4	0,223	0,032		806			96,5	3,5	7,5	2	755	1,85
	204,4	0,197	0,086										
3344/329/237,3	237,3	0,021	0,013		1250			98,1	2,7	3,9	2	1199	1,38
3344/329/272,8	272,8	0,627	0,004		2720	65505±2017.7	421±7.7	98,8	0,9	28,2	4	2644	1,48
	272,8	0,653	0,006										
3444/321/193,18	*193,18*	*-0,085*	*0,002*		*391*			*91,9*	*8,1*	*5,7*	*4*	*298*	1,06
3344/329/118,68	*118,68*	*0,367*	*0,088*		*420*			*96,4*	*3,6*	*4,3*	*9*	*375*	0,37

Niauth = authigenic Ni enrichment (%), Nidetr = detritic Ni enrichment (%), EF_Ni = Ni authigenic enrichment factor; Nixs = non-detrital Ni excess (calculated according to Pašava et al. 2019). The two lowermost rows (grey) are literature data from Pašava et al. 2019.

3.3 δ^{13}C values

The δ^{13}C values ranged between -26.72 ± 0.05‰ and -24.60 ± 0.05‰ for the sulfides and -26.61 ± 0.05‰ and -25.17 ± 0.05‰ for the silicates. The mass% C ranged between 0.9 to 9.3 C% in the sulfides and 7.79 to 42.93 C% in the silicates (Fig.3. Table S7).

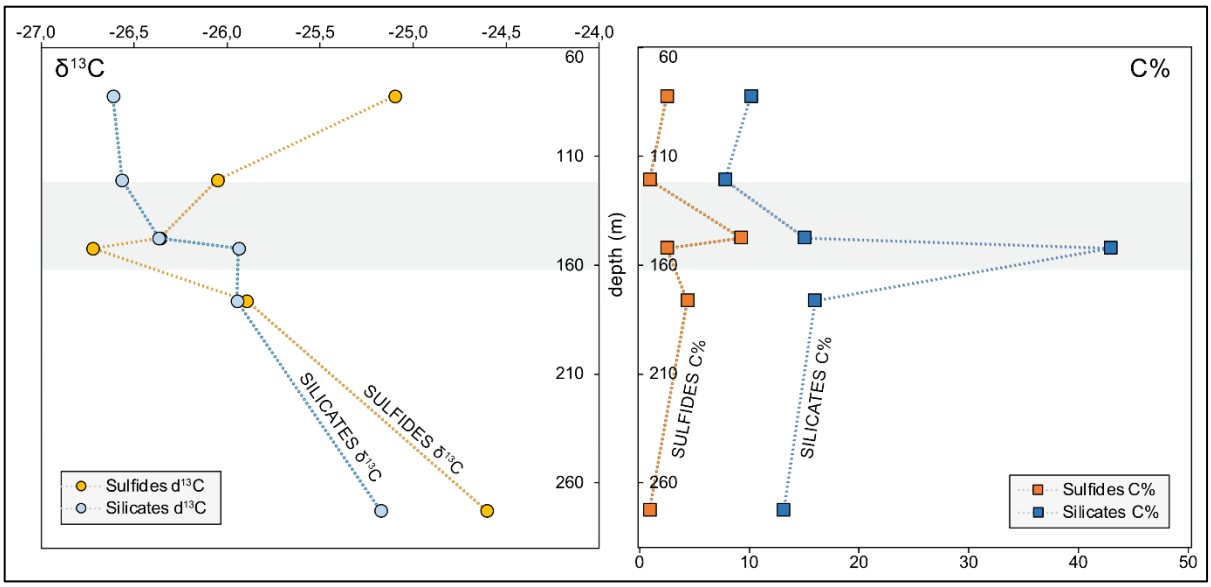

Fig.3. *Left panel: $\delta^{13}C$ values in the samples downcore of 3344:329, GTK-329. Error bars (±0. 08‰) are smaller than the marker size. Right panel: C (%) values in the same samples. Orange symbols denote sulfides and blue symbols indicate silicates. The gray area marks the $\delta^{60}Ni$ deviation field*

3.4 Elemental composition (LA-ICP-MS)

3.4.1 Elemental (including REE) distribution

Trace element concentrations in sulfide and silicate phases vary substantially across the drill core, both in absolute magnitude and in the proportion of analyses above detection limit (Table S2). In sulfide phases, REE concentrations are low throughout most of the section, with the majority of individual spot analyses at b.d.l. for most elements; this is particularly pronounced at 118.68 m and 272.88 m, where more than half of all sulfide analyses yield entirely b.d.l. REE patterns. Where REE are detectable in sulfides, the dominant elements above detection are Y, La, Ce, Pr, and Nd, with MREE and HREE (Sm through Lu) rarely detected except at 82.4 m and the biogenic interval at 155.9 m. At 82.4 m, isolated sulfide grains show anomalously elevated total REE, with one grain yielding Y = 185.6 µg/g and full HREE suites detected (Er up to 20.0, Yb up to 19.3, Dy up to 22.2 µg/g), indicating discrete REE-rich microdomains. At 155.9 m, detectable sulfide grains consistently show HREE-dominated patterns with Y (1.8–3.8 µg/g), Er (0.2–0.5 µg/g), Ho, Tm, and Yb above detection, while LREE and MREE are near or below detection, a pattern distinct from the rest of the section and discussed further below. In silicate phases, REE are detected more frequently and at higher concentrations across all depths. LREE (La, Ce, Pr, Nd) dominate the silicate signal throughout the core and are detected in the majority of analyses at every depth. At 82.4 m, silicate REE are predominantly LREE-dominated with HREE near or below detection. At 118.68 m and 152.27 m, silicates show enrichment across the full REE suite including significant HREE contributions (Er, Tm, Yb, Lu consistently above detection), with individual analyses reaching total REE sums substantially above the section average. Phosphorus is detectable in both phase types but shows a depth-dependent pattern, discussed in relation to Ni–P correlations in section 4.4, with notably elevated values in sulfides at 155.9 m (up to ~130 µg/g).

Rare earth element (REE) distributions differ markedly between silicates and sulfides. Silicates display pronounced Eu anomalies that are absent in the sulfides. They also show LREE enrichment

relative to HREE, whereas the sulfides exhibit the opposite pattern. In addition, the silicates display a slight negative Y anomaly. In the sulfides, the Y anomaly is weak and varies with depth, being absent or negligible in most intervals but present at selected depths, suggesting a mixed signature of microbial influence and $Fe(OH)_3$ precipitation. REE systematics also vary with depth: LREE > HREE shifts to HREE > LREE, before returning to LREE > HREE below 160 m (Fig. 4; Table S2). There is a weak inverse relationship between [Ni] and MREE/HREE. In particular, the correlation between MREE/HREE and [Ni] changes from negligible in silicates ($R^2 = 0.01$) to weakly negative in sulfides ($R = -0.29$, $n = 9$, $p = 0.4$, Fig. 7). Although the correlation between MREE/HREE and [Ni] in sulfides is statistically weak ($R = -0.29$, $n = 9$, $p = 0.4$), the data points showing the most negative deviation are spatially concentrated in the stratigraphic intervals where HREE enrichment is most pronounced (e.g., 118.68–155.9 m), consistent with the broader REE transition documented across the core, and suggesting the trend reflects a primary geochemical signal rather than analytical scatter.

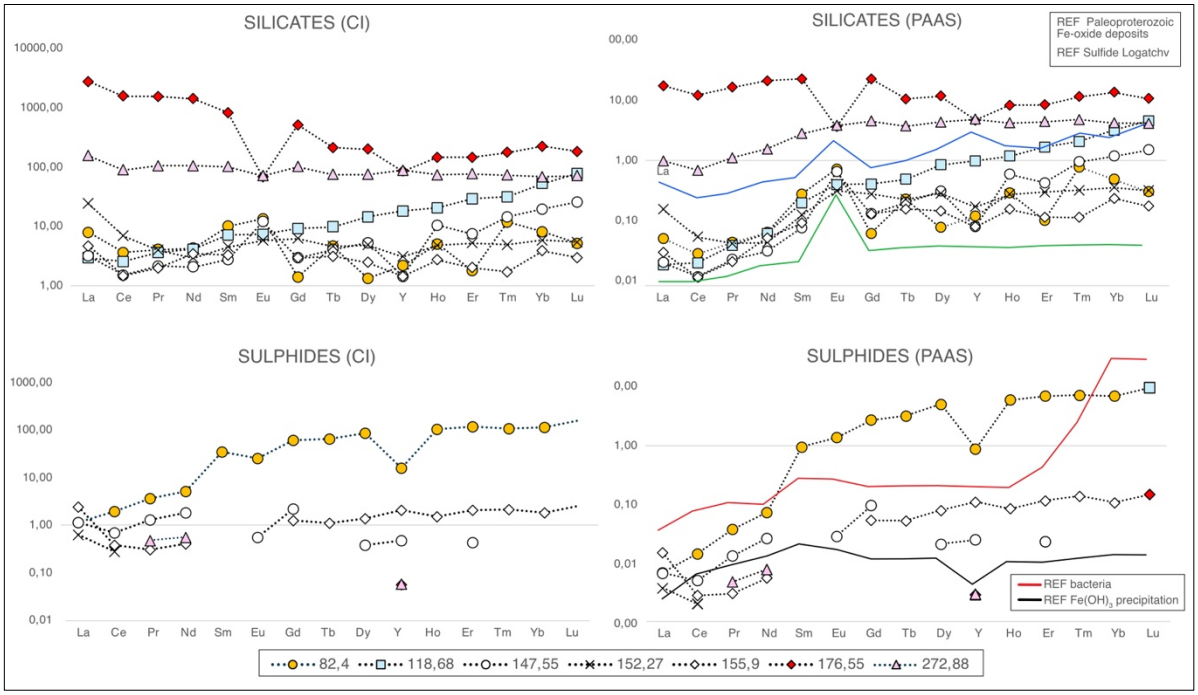

Fig. 4. *REEs in silicates (upper panels) and sulfides (lower panels) normalized to CI (left panels) and PAAS (right panels). The lower left panel also show representative reference values (PAAS normalized) for bacteria* (Martinez et al. 2014) *and the precipitation of* $Fe(OH)_3$ (Bau 1999).

3.5 Magnetic susceptibility

Magnetic susceptibility (MS) measurements reveal systematic stratigraphic variability consistent with changes in both the abundance and grain-size distribution of magnetic sulfides throughout the drill core (80–230 m see Fig.5). Field-dependent susceptibility curves display the characteristic non-linear increase consistent with monoclinic pyrrhotite as a major contributor to the susceptibility signal (Worm et al., 1993; Hrouda et al., 2006). In pyrrhotite, the magnitude of this field dependence varies with grain size, and we therefore use it here to estimate approximate effective grain sizes by comparison with the calibration data of Worm et al. (1993).

Bulk MS values (10 μT and 1 mT) show a pronounced decrease between ~145 and 160 m depth where susceptibility drops by nearly an order of magnitude relative to overlying and underlying intervals. This decrease indicates a reduced concentration of magnetic phases in the mid-core section. The normalized field-dependent susceptibility MS (1 mT)/MS (10 μT) also exhibits a minimum in this interval indicating weaker field dependence and therefore finer effective magnetic grain size in pyrrhotite.

Comparison of the sample ratios with ratios derived from sized experimentally calibrated pyrrhotite curves of Worm et al. (1993) suggests that the upper and lower sections of the core are dominated by coarse-grained pyrrhotite (ca. 50–100 μm) whereas the 140-160 m interval is characterized by significantly finer-grained pyrrhotite (approximately 25-40 μm). These grain sizes should be regarded as approximate calibration-based estimates rather than direct measurements. Overall, the mid-core interval is distinguished by a lower abundance in monoclinic pyrrhotite, and systematically finer pyrrhotite grain size.

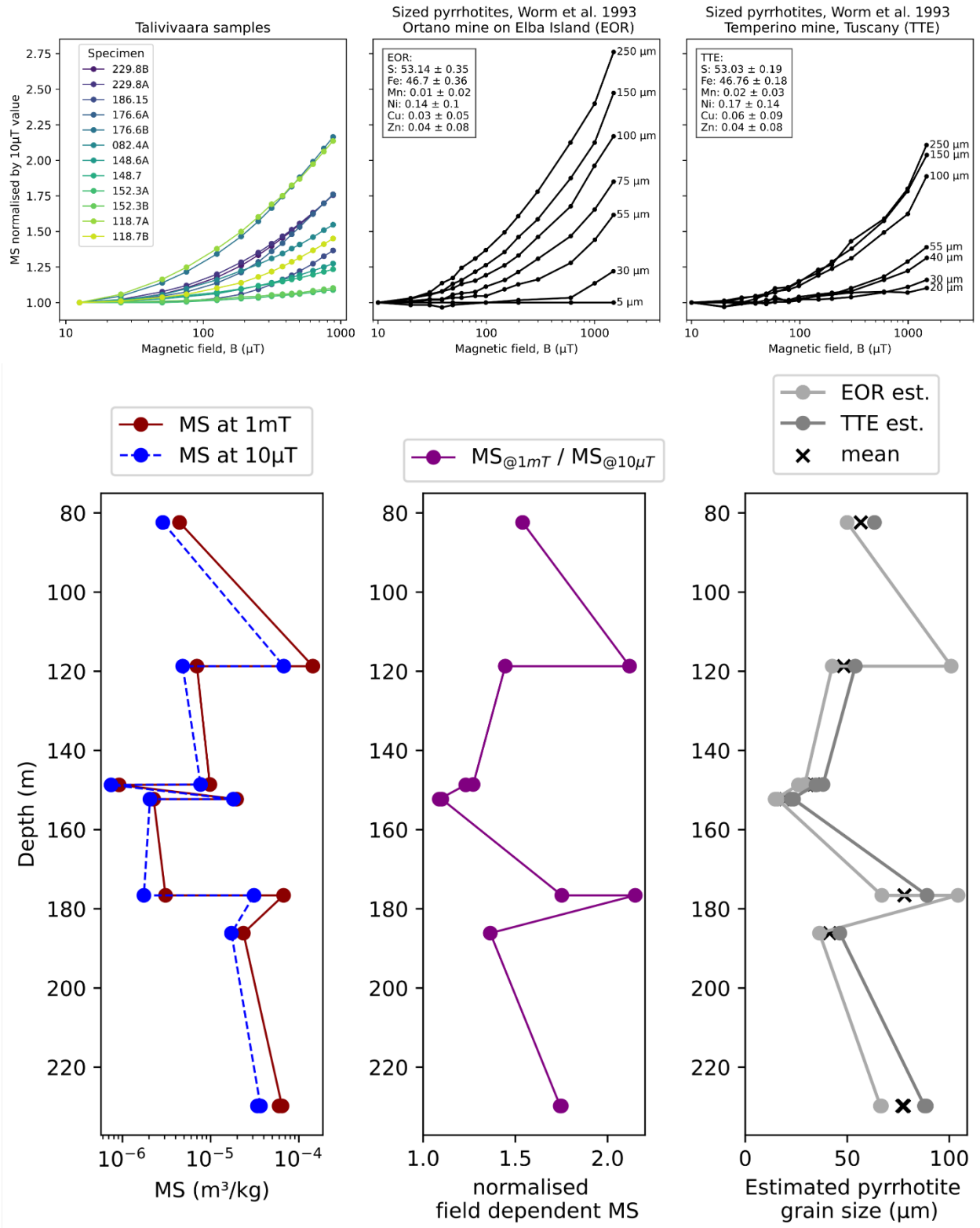

Fig. 5. *Upper panels: MS vs. Field Strength where MS changes (normalized by its value at 10 μT) under an applied magnetic field, B with the increase from 10 to 1000 μT. Upper left panel shows experimental data for the various Talvivaara sample depths showing that an increased field strength increase the mineral susceptibility. The upper middle and right panels show reference*

standards (monoclinic pyrrhotite) from Worm et al. (1993), where larger grains (250 µm) show a steeper increase in susceptibility and finer grains (5 to 20 µm) stay almost flat.

3.6 Raman Spectroscopy

Raman spectra were acquired on samples from 118.68 m, 147.55 m and 152.27 m depth (Fig. S8). All spectra display a peak at ~120 cm^{-1} attributable to stray light, and broad features at ~200–400 cm^{-1} consistent with the principal Raman-active modes of monoclinic pyrrhotite (Lara et al., 2015). A band at ~790 cm^{-1} is attributed to Si-O-Si stretching vibrations of silicate material (Neuville et al., 2021). Due to the fine-grained intergrowth of sulfide and carbonaceous material at the micro-scale, isolation of pure carbonaceous grains was not possible under the available instrumentation. The carbonaceous component is characterized by G bands at ~1558-1560 cm^{-1} and D1 defect bands at ~1394–1400 cm^{-1}, with G/D1 ratios of 1.6, 1.1, and 4.0 across the three depths respectively. A prominent second-order band at ~2490 cm^{-1}, consistent with the 2D overtone of graphitic carbon, is additionally observed in the 147.55 m spectrum (Fig.S8). A peak at ~2329 cm^{-1} present in several spectra is attributed to atmospheric N_2 in the laser path and carries no sample information.

4. Discussion

The δ^{60}Ni values measured in the Talvivaara black shale fall within the range of most black shale deposits (-0.43 to +0.71‰; Fig. 6). Their isotopic compositions overlap with the average black shale signature and with values typical of mafic to ultramafic source rocks. This distribution is consistent with the geological history of the Talvivaara succession, which developed under relatively stable conditions and was primarily influenced by mafic and ultramafic provenance, accompanied by diagenetic Ni redistribution within a redox-stratified basin and without evidence for a focused hydrothermal overprint on the Ni isotope systematics (Kontinen et al. 2013; Pašava et al. 2019). The Talvivaara black shales were deposited in a restricted anoxic to euxinic basin (Loukola-Ruskeeniemi and Heino 1996; Loukola-Ruskeeniemi and Lahtinen 2013; Young et al. 2013; Pašava et al. 2019), which likely facilitated the overall observed Ni isotopic and elemental patterns.

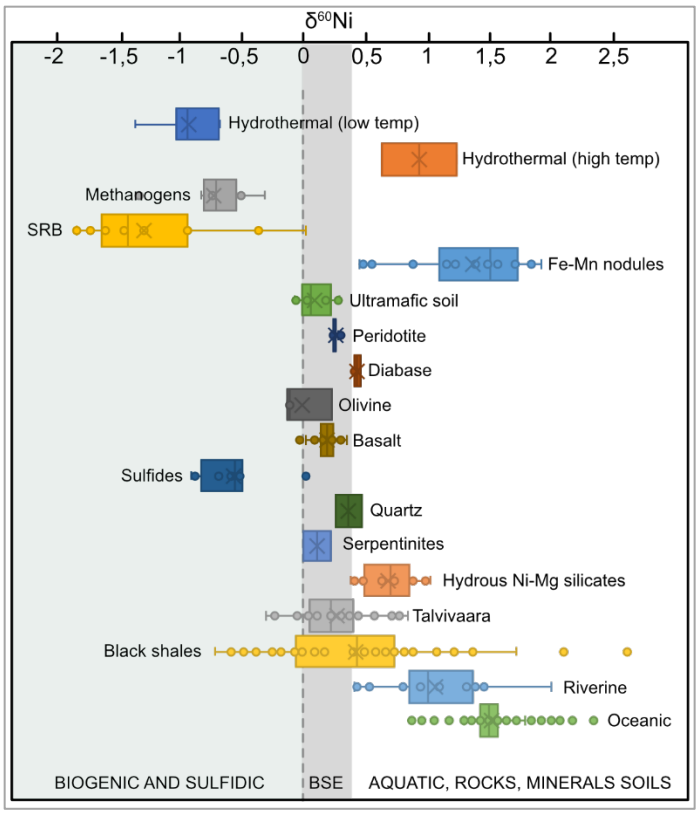

Fig. 6. *Ni isotope composition of the Talvivaara samples in relation to natural and laboratory samples of selected reservoirs (Cameron 2009; Steele et al. 2011; Gall et al. 2012; Gall et al. 2013; Gueguen et al. 2013; Hein et al. 2013; Cameron and Vance 2014; Chernonozhkin et al. 2015; Ratié et al. 2015; Wang and Wasylenki 2017; Spivak-Birndorf et al. 2018; Pašava et al. 2019; Archer et al. 2020; Beunon et al. 2020; Klaver et al. 2020; Sorensen et al. 2020; Gueguen et al. 2021; Ratnayake et al. 2021; Lemaitre et al. 2022; Chen et al. 2023). The gray area represents the BSE $\delta^{60/58}$Ni value modified from Hiebert et al. (2022).*

4.1 Sulfidization

Sulfidization of Fe-bearing minerals concurrent with organic matter represent key diagenetic transformations in the Talvivaara black shales (Large et al. 2014; Peiffer et al. 2015). These reactions preferentially incorporated isotopically light Ni into authigenic sulfide phases, consistent with earlier observations (Pašava et al. 2019). The ternary TOC-S-Fe relationship (Kumar et al. 2024) (Fig. S9) constrains the redox architecture of the depositional environment. Most samples plot above the stoichiometric pyrite line, signifying iron-excess and sulfur-limited conditions characteristic of suboxic to mildly reducing facies where sulfidization remains incomplete. Conversely, the shallowest sampled interval (~82 m) shifts toward more reducing fields, indicating enhanced sulfidization under localized anoxia. This process facilitates pyrite precipitation and the initial sequestration of Ni into the sulfide lattice. Pyrite nucleation kinetics are further accelerated by the presence of Ni, as demonstrated by Morin et al. (2017), reinforcing the link between trace metal enrichment and sulfide mineralogy in these sections. Within the TOC-S-Fe ternary framework, the 118.68-152.27 m interval is distinguishable from the rest of the core. While most samples plot above the stoichiometric pyrite line, consistent with iron-excess and sulfur-limited conditions typical of suboxic to mildly reducing facies, samples from this interval show a systematic shift toward sulfur-enriched compositions, reflecting enhanced sulfidization under

intensified reducing conditions. This shift is accompanied by elevated organic carbon contents (Fig.3) and the strongly negative $\delta^{34}S$ values (Fig.2) characteristic of open-system microbial sulfate reduction, indicating that sulfur supply was transiently augmented by biogenic H_2S production rather than being purely diagenetically controlled. The co-occurrence of these features, sulfur enrichment, elevated TOC, and light sulfur isotopes, within a stratigraphically coherent interval distinguishes the 118.68-152.27 m zone from the background iron-excess trend observed elsewhere in the core and is inconsistent with simple diagenetic sulfidization alone. The geochemical and isotopic character of this interval thus indicates that biological processes transiently overprinted the mineralogical control on Ni isotope systematics. Correlation plots between selected elements in silicates and sulfides as a function of depth (Fig. 7) show a strong shift at the 118.68–152.27 m interval, consistent with the shifts observed in $\delta^{60}Ni$, $\delta^{34}S$, $\delta^{13}C$, C%, and REEs (Figs. 2–4). The overall interpretation is that Mn and P shift from minor to primary scavengers of Ni across this interval, indicating a spike in primary productivity. This shift is further characterized by a transition to a negative correlation between Ni and S in the sulfides, suggesting that intense microbial sulfate reduction decoupled the two elements, with nickel being preferentially sequestered into organic-rich microdomains or microbial biomass rather than the pyrite lattice.

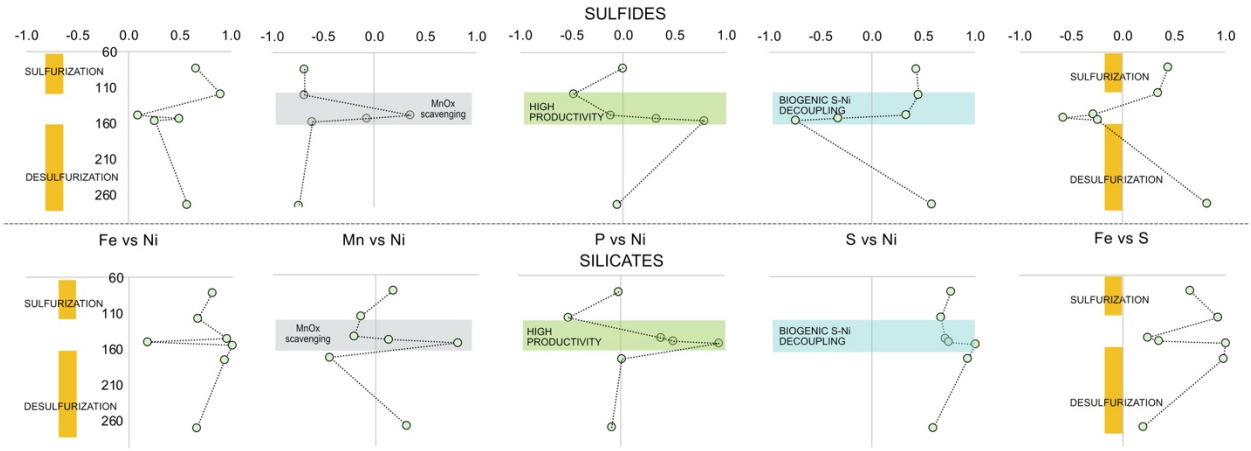

Fig.7. *Spearman correlation plots in LA-ICP-MS data for silicates (upper panels) and sulfides (lower panels).*

4.2 Core-wide desulfurization and mineralogical control on Ni isotopes

The systematic downcore transition from pyrite-dominated assemblages in the shallow intervals (82-172 m) to pyrrhotite- and pentlandite-bearing assemblages in the deepest samples (204-272 m), with pyrite absent below ~172 m (Table S3, S4, Fig. S1), reflects a progressive desulfurization of the sulfide assemblage during diagenesis and low-grade metamorphism. This transition follows the well-established reaction pathway in which pyrite converts to pyrrhotite through loss of sulfur under reducing, sulfur-undersaturated conditions, with subsequent exsolution or recrystallization producing pentlandite along pyrrhotite grain boundaries (Coldebella et al., 2025). The localized occurrence of pentlandite as crack infillings along pyrrhotite margins in the deepest samples (237 m and 272 m; Fig. S1) is consistent with late-stage Ni redistribution during this metamorphic transformation rather than primary precipitation.

Independent Raman spectroscopic analysis provides corroborating mineralogical evidence consistent with the EPMA-based phase assignments (Fig. S8). The carbonaceous component yields G bands at ~1558-1560 cm^{-1} and D1 defect bands at ~1394-1400 cm^{-1}, with G/D1 ratios of 1.6, 1.1, and 4.0 across the three depths respectively. For the 118.68 m sample, the R2 parameter of Beyssac et al. (2002), defined as the area ratio D1/(G+D1+D2), yields a value of ~0.38, consistent with peak metamorphic temperatures of ~470°C and upper greenschist to amphibolite facies conditions (Beyssac et al., 2002; Wopenka & Pasteris, 1993). A second-order band at ~2490 cm^{-1}, consistent with the 2D overtone of graphitic carbon, is additionally observed in the 147.55 m spectrum. The G-dominated spectra are irreconcilable with modern organic contamination, which characteristically produces D1 intensities comparable to or exceeding G (Marshall et al., 2007), confirming that the carbonaceous phases are thermally mature and of indigenous Paleoproterozoic origin, and ruling out modern contamination as a source of the isotopic signals discussed further in Sections 4.3 and 4.4. The independent spectroscopic confirmation strengthens the interpretation that Ni isotope systematics through the isotopic shift section are governed by mineralogical partitioning within a pyrrhotite-dominated sulfide assemblage.

This mineralogical reorganization exerts a first-order control on Ni isotope systematics throughout most of the core. EPMA maps show that Ni is hosted almost exclusively in pyrite and pyrrhotite where both coexist, and that Ni is consistently enriched in pyrrhotite relative to adjacent pyrite (Fig. S4). The $\delta^{60}Ni$ values of micromilled sulfides reflect this mineralogical partitioning: pyrrhotite-hosted Ni is isotopically lighter than coexisting pyrite, with $\delta^{60}Ni$ values around -0.36‰ in pyrrhotite-dominated microdomains versus -0.09‰ to +0.32‰ in near-stoichiometric pyrite. This fractionation is consistent with kinetic and equilibrium isotope effects during sulfide recrystallization, in which isotopically light Ni is preferentially incorporated into the more metal-deficient pyrrhotite structure relative to pyrite (Ciscato et al., 2018; Bruggmann et al., 2024).

Among the pyrrhotite- and pentlandite-bearing intervals, the heaviest $\delta^{60}Ni$ values occur in pentlandite from the deepest samples (272 m; $\delta^{60}Ni$ = +0.63 to +0.65‰), marking a distinct late-stage sink in which Ni released during pyrite-to-pyrrhotite conversion is concentrated into $(Fe,Ni)_9S_8$. Comparable $\delta^{60}Ni$ values (+0.71 to +0.72‰) are also recorded in the shallow pyrite-dominated interval at 82.4 m, where the heavy signature reflects mineralogical partitioning between coexisting pyrite phases rather than metamorphic pentlandite formation, confirming that isotopically heavy Ni is produced by distinct mineralogical mechanisms at different stratigraphic levels. Because pentlandite formation involves selective incorporation of Ni mobilized from the surrounding Fe-sulfide matrix, it preferentially captures the isotopically heavy Ni residual after lighter Ni has already been sequestered into pyrrhotite, driving pentlandite toward the heaviest compositions observed in the section. This desulfurization may also partly explain the relative enrichment in downcore sediments in ^{34}S as compared to those above 152.27 m. Desulfurization of pyrite to pyrrhotite in sedimentary rocks over temperatures between 200 and 400°C may be expected to increase $\delta^{34}S$ by up to +3‰ (Bucholz et al., 2020). Thus, specifically the pyrite–pyrrhotite–pentlandite reaction series, governs Ni isotope systematics through most of the Talvivaara drill core. The occurrence of the heaviest $\delta^{60}Ni$ values at both the shallowest (82.4 m, pyrite-dominated) and deepest (272 m, pentlandite-bearing) intervals, through mechanistically distinct processes, confirms that no single $\delta^{60}Ni$ value can be interpreted without knowing its mineralogical host. Bulk $\delta^{60}Ni$ values in these intervals therefore primarily reflect the integrated isotopic composition of coexisting sulfide phases rather than a direct record of seawater, hydrothermal fluids, or biological activity. The downcore ^{34}S enrichment driven by desulfurization is therefore an expected consequence of mineralogical reorganization, against which the isotopic

excursion at 118.68–152.27 m must be evaluated. Critically, the strongly negative $\delta^{34}S$ values recorded in that interval (approximately -10 to -13‰) are directly at odds with the desulfurization-driven ^{34}S enrichment trend observed elsewhere in the core, and cannot be explained by the pyrite-pyrrhotite reaction series alone. This isotopic reversal marks the 118.68–152.27 m interval as geochemically distinct and points toward an additional process operating at that depth, which is addressed in Sections 4.3 and 4.4.

4.3 Isotopic shift at 118.68-152.27

The observed shift to negative $\delta^{60}Ni$ values between 118.68 and 152.27 m suggests a significant transition in the Ni-isotope mass balance within the basin. The isotopically light $\delta^{60}Ni$ values can originate from mafic-ultramafic sources (e.g. Hiebert et al. 2022), and several studies have already established that the Talvivaara basin received an ultramafic contribution (Loukola-Ruskeeniemi and Lahtinen 2013; Kontinen and Hanski 2015). Comparison with reference materials places the entire drill core within the mafic/ultramafic field (Fig. 8). Although direct mechanical input from ultramafic terranes would elevate detrital Ni, our Ni_{detr} fractions (0.8–3.8%) indicate that most Ni in Talvivaara shales is authigenic (Table 1). This suggests that the ultramafic $\delta^{60}Ni$ signal was likely delivered in dissolved form, potentially through chemical weathering in the catchment or rapid early diagenetic alteration of minor ultramafic debris. Isotopically light Ni released by such weathering could enter riverine or porewater reservoirs and precipitate into authigenic sulfides and organic complexes, leaving little detrital trace. Globally, the period 2.0-1.9 Ga was marked by intensified plume-related mafic/ultramafic plutonism and volcanism (Condie 2001), which could have supplied widespread ultramafic material and weathering solutions rich in S and base metals, contributing to the dissolved Ni that imprinted the authigenic $\delta^{60}Ni$ signal. The likelihood of this scenario is diminished by the fact that the inferred alteration is stratigraphically constrained, whereas the proposed model would necessitate a deposit-wide impact. The stratigraphic specificity of the excursion therefore points toward a locally driven process rather than a basin-wide geochemical event, which is addressed in the following section.

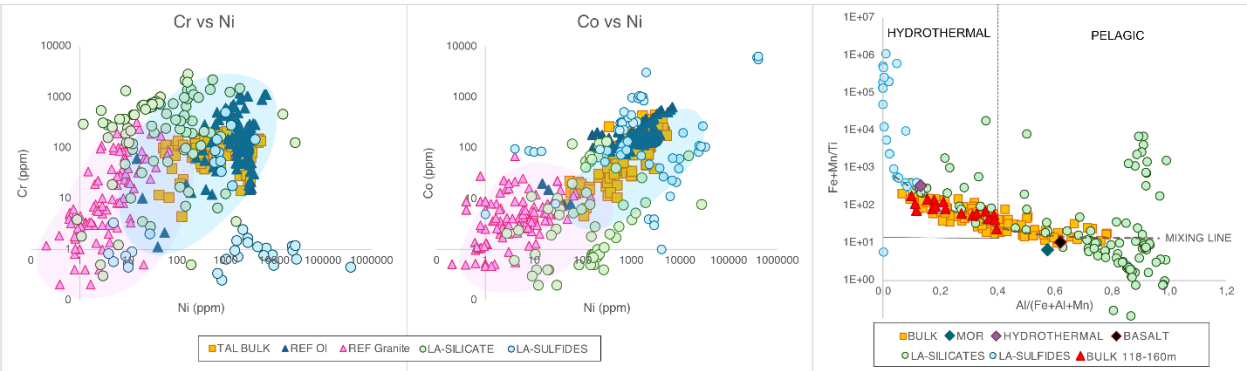

Fig.8*. Left and middle panels display the Cr vs Ni and Co vs Ni for the bulk samples (orange squares), LA-ICP-MS silicate samples (light green circles), LA-ICP-MS sulfide samples (light blue circles), reference granite (pink triangles) and reference olivine (dark blue triangles). Data compiled from Georoc database filtered as mineral composition and concentration of Cr, Co and Ni. Right panel shows the Fe/Ti vs Al/(Fe+Al+Mn). Bulk samples (orange squares), bulk sample depth 118.68–152.27 m (red triangles), LA-ICP-MS silicate samples (light green circles), LA-ICP-*

MS sulfide samples (light blue circles), ref hydrothermal (purple diamond), ref basalt (black diamond), ref MOR (dark turqoise diamond).

4.4 Biogenic controls on the isotopic excursion

The biological uptake of Ni by plankton (Ni_{BIO}; Table 1) is low throughout the section, with only slightly elevated values in the upper interval, indicating that planktonic uptake was not a major control on either Ni accumulation or isotopic fractionation. Moreover, Ni_{BIO} is calculated using a "standard" phytoplankton composition (Little et al. 2015) adapted from Pašava et al. (2019), and even substantial planktonic uptake would have limited impact on sedimentary Ni inventories, as 90–95% of biologically cycled Ni is rapidly recycled back to seawater unless scavenged by sulfides, clays, or Fe-Mn oxides (Collier and Edmond 1984). These authors also emphasized the inherently weak association between Ni and plankton, implying that additional processes are required to generate Ni enrichments in sediments. Because Ni_{BIO} does not account for uptake and retention by other microbial communities, it should be regarded as a minimum estimate of biological Ni cycling. Microbial processes beyond planktonic uptake provide a more plausible mechanism for biological Ni fractionation in the Talvivaara black shale. Methanogens, for example, can accumulate up to ~150 ppm Ni (Scherer et al. 1983), and Cameron et al. (2009) demonstrated that methanogenesis drives isotopically light $\delta^{60}Ni$ values through preferential incorporation of the lighter Ni isotope. In natural samples from the glacial deposits of the Marinoan Nantuo Formation, Zhao et al. (2021) confirmed the involvement of methanogenesis during pyrite precipitation by comparing REE patterns with $\delta^{60}Ni$. Methanogens fractionate REEs and preferentially adsorb HREE over MREE and LREE and concomitantly preferentially accumulate the lighter Ni isotope (Cameron 2009). Thus, microbially formed organic matter is characterized by LREE ≈ MREE < HREE (Martinez et al. 2014), isotopically light Ni (Zhao et al. 2021), whereas iron oxide, that is also characterized by accumulating isotopically light Ni (Elliott and Steele 2017; Wang and Wasylenki 2017; Watkins et al. 2017), is characterized by a flat REE distribution and a weak Y anomaly (Bau 1999). Both the PAAS and CI normalized REEs in Talvivaara sulfides show a pattern indicative of microbial activity with HREE larger than MREE and LREE (Fig.4) and largely devoid of Y anomaly, though weak anomalies are present at selected depths, indicative of a mixed signature of microbial activities and $Fe(OH)_3$ precipitation. The silicate, on the other hand, show a relatively flat REE distribution and both moderately strong negative and, in places, positive Eu anomalies (Fig. 4). This pattern is indicative of ancient Fe-oxide deposits and consistent with an influx of initial Fe-(oxyhydr)oxides that scavenge REEs, locking in an oxide-associated chemical fingerprint before being transported into the deep basin (Virtasalo et al. 2015). Upon reaching the euxinic seafloor, these aggregates reacted with biogenic H_2S and were mineralogically converted into sulfides, preserving the original trace element signature despite the total change in redox state.

Downcore variations in HREE, MREE, P, and the Ni-P correlation reveal a shift between 140-160 m in both silicates and sulfides, where the correlation between Ni and P shifts from very weak to very strong and the HREE dominates over MREE (Fig. 9). This indicates a shift towards increased productivity and that the shift towards isotopically light Ni between 118.68 and 152.27 m may be due to microbial activity. An increased productivity at this depth range should thus also be visible in paleoproductivity indicators, such as P/Ti and Cu/Al (Riboulleau et al. 2003; Altaee et al. 2024). Ratios of P/Ti < 0.34 is indicative of low productivity and values >0.79 indicates high productivity (Algeo et al. 2011). Our values have a mean around 11 that shift to almost 300 at the 118.68-152.27 m depth range (Fig.S10). The Cu/Al ratio is generally low with a mean around 0.086 but

show a strong shift to 27.7 at depths around 150m (Fig.S10), also indicative of high paleoproductivity and exceeding the average shale value of ~$5.1*10^{-4}$ (Wedepohl 1971; Zhao et al. 2016).

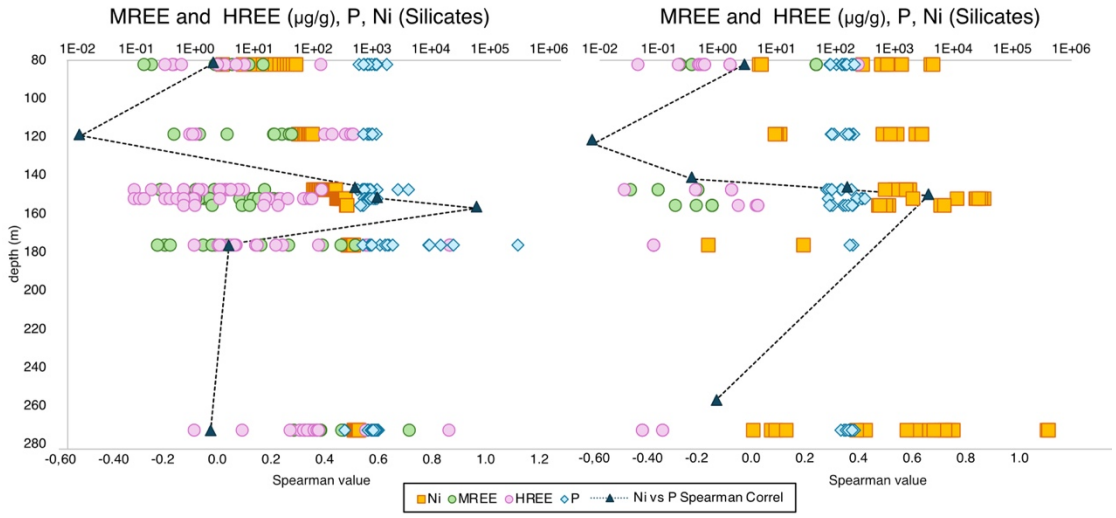

Fig. 9. *The variation of HREE, MREE, P, Ni and Ni vs P correlation as a function of depth in silicates (left panel) and sulfides (right panel).*

Biological and diagenetic control on δ^{60}Ni is further supported by micromilled analyses of δ^{60}Ni, δ^{13}C, and C% (Figs. 2, 3). At the micro-scale, isotopically light Ni (depth interval 118.68-152.27 m) coincides with enhanced negative δ^{13}C, elevated C%, and a strong positive correlation between P and Ni, all consistent with a biogenic Ni signal (Fig. 3, 7). These relationships contrast sharply with downcore bulk trends, where Ni-TOC and δ^{60}Ni-TOC correlations are weak, highlighting the importance of micro-scale heterogeneity (Fig. S11). Bulk carbon measurements show relatively uniform total carbon contents and δ^{13}C values (8.1 ± 2.6 wt% and -28 to -24‰) across the investigated interval (Loukola-Ruskeeniemi 1999; Kontinen and Hanski 2015), whereas micromilled analyses reveal sharp, localized spikes in C% and distinctly lighter δ^{13}C values (Fig.3). This divergence reflects the averaging effect inherent to bulk sampling, which obscures thin, highly reactive horizons that represent only a minor fraction of the total sediment mass. At the mineral scale, sulfide- and silicate-hosted Ni display contrasting behaviours. In sulfide-rich microdomains, C%, δ^{13}C, and δ^{60}Ni are tightly coupled. The C% correlates negatively with δ^{60}Ni, whereas δ^{13}C correlates positively, indicating that organic-rich, ^{13}C-depleted horizons are enriched in isotopically light Ni. These relationships reflect diagenetic conditions dominated by organic matter degradation, microbial respiration, sulfate reduction, and sulfide precipitation, processes that preferentially sequester light Ni isotopes (Parigi et al. 2022b; Parigi et al. 2022a). In contrast, silicate-hosted Ni shows weak or inconsistent correlations with carbon parameters, consistent with a detrital, lattice-bound Ni reservoir whose isotopic composition is largely inherited from primary minerals and only weakly modified during diagenesis.

The depth interval 118.68-152.27 m is characterized by light δ^{34}S values (approximately -1‰ to -13‰, Young et al. 2013), indicative of microbial sulfate reduction (MSR) operating under open-system conditions. Values of -13‰ sulfur isotope signatures are consistent with sustained MSR, allowing for large isotopic fractionation (Fike et al. 2015). Desulfurization processes increasing the δ^{34}S values of sulfides further downcore discussed previously are not expected to produce δ^{34}S

differences on the scale of that observed between the shallowest and deepest sediments, or the range of values represented by sediments above 152.27 m. The co-occurrence of light δ^{60}Ni values suggests that Ni was mobilized into porewaters and subsequently incorporated into newly forming Fe-sulfide phases during early diagenesis. Sulfide minerals preferentially incorporate isotopically light Ni, leading to the observed δ^{60}Ni depletion. The large spread in δ^{34}S values further points to complex sulfur cycling, potentially involving repeated cycles of sulfur disproportionation and oxidation that enhance isotopic heterogeneity (Fike et al. 2015). Geochemical ratios such as Fe+Mn/Ti and Al/(Fe+Mn) indicate a transitional redox zone characterized by reductive dissolution of Fe-Mn oxides and reprecipitation as authigenic sulfides, which efficiently scavenge light Ni (Fig.8). The coupled light δ^{34}S and δ^{60}Ni values, evidence for metal mobilization, and strong micro-scale heterogeneity support interpretation of this interval as a diagenetic redox front marking intensified microbial sulfate reduction and associated Ni sequestration under anoxic conditions. It should be noted that the δ^{60}Ni values in the biogenic interval, while shifted toward lighter compositions, largely overlap with ranges produced by abiogenic mineralogical processes (Fig. 5); the biogenic interpretation therefore rests on the coherent multi-proxy convergence rather than on δ^{60}Ni in isolation, and a larger dataset with more tightly coupled mineral-scale S–C–Ni analyses would strengthen this conclusion.

An additional biological process worth considering in the context of the 118–152 m interval is the anaerobic oxidation of methane (AOM). The continental margin setting of the Talvivaara basin, with high organic matter inputs, anoxic bottom waters, and metal-rich diagenetic fluids, is broadly conducive to AOM, which in modern settings occurs at the sulfate-methane transition zone (SMTZ) where upward-migrating methane meets downward-diffusing sulfate (Rickard 2014). The δ^{13}C values observed here (~−25‰) are too heavy to implicate canonical sulfate-driven AOM, which typically produces strongly ^{13}C-depleted carbon below −50‰ (Zhao et al. 2021). However, metal-dependent AOM — coupled to reduction of Fe or Mn rather than sulfate — may produce less negative δ^{13}C values and has been documented in continental margin and deep marine environments where sulfate is limited and reactive metal oxides are abundant (Riedinger et al. 2014; Beal et al. 2009; Su et al. 2019). Given the age of the Talvivaara sediments (2.1–1.9 Ga), a Paleoproterozoic ocean characterised by low sulfate concentrations and abundant Fe and Mn, and the documented presence of reactive Mn-rich intercalations in GTK-329 below 150 m (Loukola-Ruskeeniemi and Lahtinen 2013; Young et al. 2013), metal-dependent AOM cannot be excluded as a contributing process within or below the SMTZ. The decoupling of Fe and S within sulfides at 147–152 m (Fig. 6) and the elevated Ni and P at depth are consistent with trace element mobilization associated with AOM-driven sulfidization, as shown in modern analogues (Hsu et al. 2014). Furthermore, the Ni-enriched deep biosphere of the neighbouring Outokumpu Palaeoproterozoic sequence, a metasedimentary black shale deposit in a rift basin 150 km south of Talvivaara, has yielded molecular evidence for active methanogens and sulfate reducers throughout the drill core, with geochemical features suggestive of a potential SMTZ between 1200–1500 m depth (Itävaara et al. 2003; Nyyssönen et al. 2014). The similarities in geological history and sulfide mineralogy between the two sequences make the Outokumpu deep biosphere a relevant, if indirect, analogue for considering whether AOM-linked processes may have operated at Talvivaara. We stress that the available dataset is not sufficient to identify AOM as a primary control; the Ni isotope systematics are better described by the diagenetic and biogenic sulfate-reduction controls discussed above. However, the possibility that metal-dependent AOM contributed to Fe–S–Ni decoupling and trace element redistribution in the deeper intervals warrants consideration and further investigation.

4.5 Distinguishing diagenetic from hydrothermal controls at 118.68–152.27 m

While basin-scale hydrothermal metal supply is well documented at Talvivaara (Loukola-Ruskeeniemi and Lahtinen 2013; Young et al. 2013), the geochemical excursion at 118.68–152.27 m does not carry the signatures expected of a focused hydrothermal overprint. Epigenetic features characteristic of hydrothermal reworking are absent. However, the covariation of (Fe+Mn)/Ti, and Al/(Al+Fe+Mn) defines a smooth mixing trend between hydrothermal and non-hydrothermal components, a pattern characteristic of redox-driven diagenetic enrichment, though intervals between 118.68–152.27 m plot near the hydrothermal/diagenetic boundary, consistent with Fe addition via diagenetic remobilization rather than focused hydrothermal input (Dias and Barriga 2006; Tribovillard et al. 2006; Lim et al. 2022) (Fig.8). In this context, high Fe/Al ratios reflect Fe addition via combined hydrothermal and diagenetic processes, whereas high Al/(Al+Fe+Mn) values correspond to clay-rich, detrital sediments (Lim et al. 2022). The correlation between δ^{60}Ni and detrital proxies (Al/(Al+Fe+Mn)) highlights the preferential mobilization of isotopically lighter Ni in Fe-enriched, terrigenous-depleted intervals (Lim et al. 2022). Ni enrichment factors across the section range from EF_Ni 1–5 (Table 1), with values at 118.68-152.27 m consistently at the higher end (4-5). Micro-analytical data from sulfide phases reveal a distinct vertical trend in Fe-S coupling that clarifies these bulk observations. While deeper intervals (272m) show a strong positive correlation (R=0.8) indicative of stoichiometric sulfide precipitation, the 147-152m interval exhibits a significant negative correlation (down to R=-0.6, Fig. 7). This intra-sulfide decoupling suggests that Fe was systematically substituted by other cations, such as Ni, during authigenic mineral growth. Such a relationship is consistent with the observed enrichment factors and negative δ^{60}Ni excursions, as kinetic fractionation of Ni is enhanced during its incorporation into Fe-sulfides under pore-water disequilibrium (Ciscato et al. 2018; Bruggmann et al. 2024). The lack of correlation in the bulk data (R=0.12) reflects competing Fe signatures between these metal-rich sulfides and the surrounding silicate matrix. These negative Fe-S correlations support a model of diagenetic sulfidization mediated by biogenic activity (See section 4.3). In this scenario, Ni was effectively incorporated into authigenic sulfides, decoupling Fe from S as Ni competed for available sulfur sites. These sulfides likely represent a secondary diagenetic sink where metals were redistributed and trapped during early burial. At 118.68-152.27 m, EF_Ni values are relatively high (4-5), compared with lower values (1-3) at other depths (Table 1), indicating enhanced Ni mobilization and incorporation into authigenic phases, consistent with Fe-rich, terrigenous-depleted conditions that favor deposition of lighter Ni isotopes. The non-detrital Ni_{xs} is consistent with authigenic Ni enrichment during diagenesis, without requiring a focused hydrothermal source. However, although basin-scale hydrothermal processes likely contributed metals to the depositional system, the stratigraphically coherent δ^{60}Ni excursion between 118.68-152.27 m does not display mineralogical, magnetic, or textural characteristics consistent with focused hydrothermal overprint or metamorphic resetting. Instead, the integrated isotopic, elemental, and magnetic dataset supports preservation of a primary redox-driven biogeochemical signal, as further constrained by magnetic susceptibility in Section 4.6.

4.6 Magnetic susceptibility

Magnetic susceptibility data provide an independent line of evidence bearing on sulfide abundance and effective magnetic grain size, and on whether the δ^{60}Ni excursion at 118.68-152.27 m reflects mineral proportion effects, metamorphic recrystallization, or hydrothermal overprint. The δ^{60}Ni excursion at 118.68-152.27 m coincides with the lowest bulk MS values in the section and reduced

magnetic sulfide abundance, the opposite of what would be expected if isotopic variability were driven simply by mineral proportions. Metamorphic recrystallization can also be ruled out: rather than the grain coarsening and textural maturation expected from metamorphic Ni redistribution, the excursion interval is defined by the finest pyrrhotite grain sizes in the core (~25-40 μm versus 50-100 μm elsewhere). Hydrothermal overprint likewise finds no support in the MS data, elevated susceptibility and grain coarsening are absent, and the independent geochemical proxies show shifts consistent with sedimentary redox reorganization rather than focused fluid influx (Pandarinath, 2022). Instead, the fine-grained, texturally mixed sulfide assemblage in the excursion interval is consistent with rapid nucleation during intense early diagenetic sulfate reduction, a process known to favor fine-grained precipitates (Rickard & Luther, 2007). Outside this interval, higher MS values and coarser pyrrhotite reflect more advanced diagenetic to low-grade metamorphic textural maturation, under which Ni isotope systematics are governed by mineralogical partitioning between pyrite and pyrrhotite rather than by biological forcing.

The MS data support a two-pool model for Ni in this section. Through most of the core, a diagenetically buffered sulfide-controlled pool dominates, with δ^{60}Ni reflecting near-equilibrium partitioning among Fe-sulfide phases during progressive sulfidization and recrystallization (Raiswell & Canfield, 1996; Wang & Wasylenki, 2017). Superimposed on this background is a biogenic Ni pool, most apparent at 118.68–152.27 m, where intensified microbial activity and organic matter degradation shifted the isotopic composition of dissolved Ni toward lighter values prior to incorporation into rapidly precipitating fine-grained sulfides. The coherent covariance of δ^{60}Ni with δ^{34}S, δ^{13}C, organic carbon content, P-Ni coupling, and REE patterns in this interval indicates that the Ni pool itself was isotopically modified by biologically mediated redox cycling before mineral fixation, rather than by redistribution among sulfide phases. The Ni isotope systematics in the Talvivaara section therefore record the stratigraphically varying balance between mineralogical buffering during stable diagenesis and biological forcing during transient intervals of intensified microbial productivity.

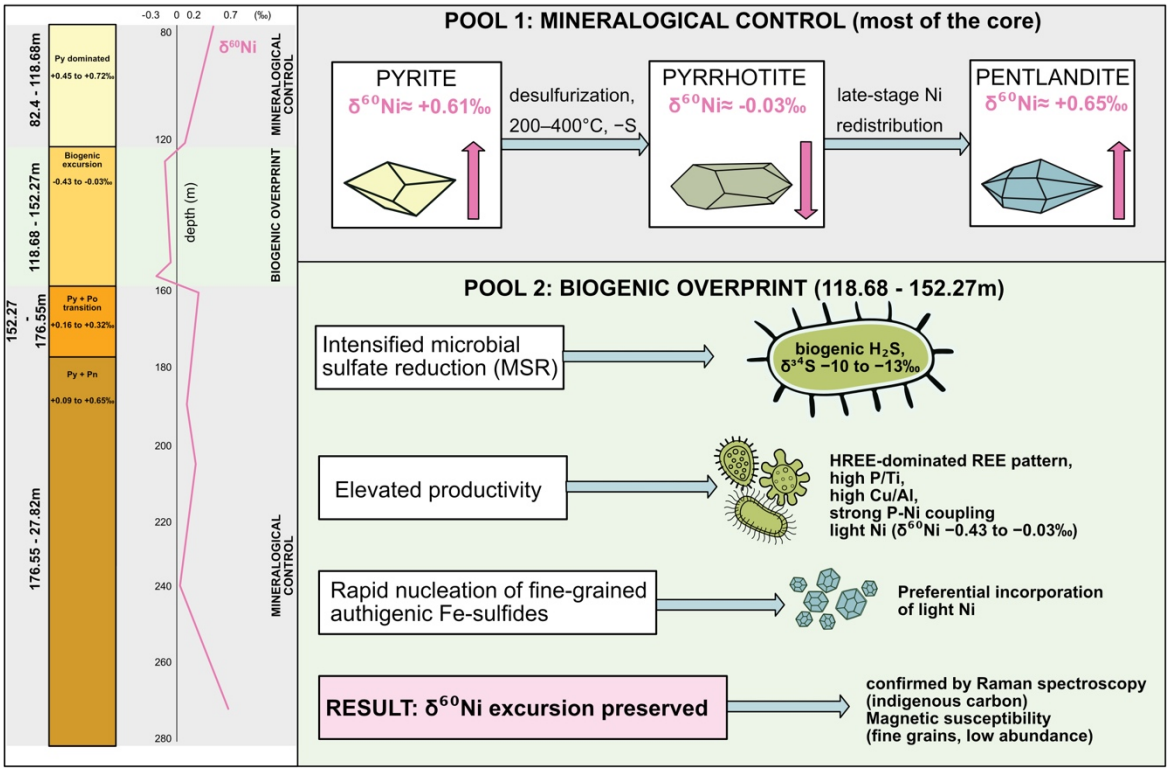

Fig. 10. *Fig. 10. Schematic summary of the two-pool model for nickel isotope fractionation in the Talvivaara drill core. The left panel shows the δ^{60}Ni depth profile from drill core GTK-329, with the biogenic excursion interval at 118.68-152.27 m highlighted in light green. Pool 1 illustrates the mineralogically controlled signal that dominates through most of the section: progressive desulfurization of pyrite to pyrrhotite and late-stage pentlandite formation partition Ni isotopes according to mineral stoichiometry, with isotopically light Ni preferentially incorporated into pyrrhotite and heavy Ni concentrated into coexisting pyrite and pentlandite. Pool 2 illustrates the biogenic overprint at 118.68-152.27 m depth: intensified microbial sulfate reduction generated biogenic H_2S and promoted rapid nucleation of fine-grained authigenic sulfides that preferentially incorporated isotopically light Ni from porewater, producing the observed δ^{60}Ni excursion. Pink arrows indicate the relative isotopic weight of Ni in each mineral phase; horizontal arrows indicate process-to-outcome relationships. δ^{60}Ni values shown are representative of each pool based on micromilled analyses in Table 1.*

5. Conclusions

This micro-scale, multi-proxy study of the Talvivaara Ni-Zn-Cu-Co black shale deposit demonstrates that Ni isotope systematics in Paleoproterozoic metamorphosed sediments are governed by two competing controls. Through most of the section, sulfide mineralogy dominates: pyrite hosts isotopically heavier Ni than coexisting pyrrhotite, and pentlandite in the deepest intervals records late diagenetic to metamorphic Ni redistribution. These mineralogically controlled signals survive low-grade metamorphism and represent the baseline behavior of Ni isotopes in shale-hosted sulfide systems.

Superimposed on this background is a stratigraphically discrete biogenic signal at 118.68-152.27 m depth, where coupled shifts in δ^{60}Ni, δ^{34}S, δ^{13}C, organic carbon content, REE patterns, and paleoproductivity proxies record an episode of intensified microbial sulfate reduction and organic

matter degradation. Magnetic susceptibility data independently confirm that this excursion reflects early diagenetic sulfide precipitation rather than metamorphic recrystallization or hydrothermal overprint. To our knowledge, this represents the first direct micro-scale evidence for a preserved biogenic δ^{60}Ni signature in Paleoproterozoic black shales. These observations support a two-pool model for Ni in the Talvivaara section: a diagenetically buffered sulfide-controlled pool that dominates through most of the core, where δ^{60}Ni reflects near-equilibrium partitioning among Fe-sulfide phases during progressive sulfidization and recrystallization, and a superimposed biogenic pool at 118.68-152.27 m, where intensified microbial activity shifted the isotopic composition of dissolved Ni toward lighter values prior to incorporation into rapidly precipitating fine-grained sulfides (Fig. 10). More broadly, these results suggest that Ni isotopes in ancient metamorphosed black shales carry recoverable biological information, but only when sampled and interpreted at the mineralogical scale. Bulk analyses of systems like Talvivaara will continue to yield ambiguous signals as long as isotopically distinct sulfide populations are averaged together. The multi-proxy micro-scale approach developed here should be transferable to other Paleoproterozoic black shale successions where the question of biogenic signal preservation remains open. Framboidal pyrite morphology in the shallowest intervals is consistent with biogenic sulfide precipitation, though abiogenic formation cannot be excluded without additional evidence. Furthermore, the Fe–S–Ni decoupling and trace element patterns in the deeper intervals raise the possibility that metal-dependent anaerobic oxidation of methane contributed to Ni redistribution at or below the sulfate-methane transition zone, a hypothesis that warrants investigation with targeted geochemical and molecular biological approaches.

Acknowledgements

We thank Haoyi Yao at Stockholm University Stable isotope lab (SIL) for assisting with the carbon isotope analyses. This study was supported by the Swedish research council (VR) project to A.N. (#2017-05018). We also want to thank Olivier Rouxel and Malou Ollivier for access to the Ifremer lab and for the assistance with the nickel isotope preparations and analysis.

Competing interests

The authors have no relevant financial or non-financial interests to disclose.

REFERENCES

Algeo, T. et al. 2011. Spatial variation in sediment fluxes, redox conditions, and productivity in the Permian–Triassic Panthalassic Ocean. *Palaeogeography, Palaeoclimatology, Palaeoecology* 308, pp. 65–83. doi: 10.1016/j.palaeo.2010.07.007.

Altaee, N., Al-Juboury, A., Ghafor, I., Zanoni, G., Rowe, H. and Al-Juboury, A. 2024. Depositional environment of the late Paleocene-early Eocene Sinjar Formation, Iraq: Implications from facies analysis, mineralogical and geochemical proxies. *Heliyon* 10. doi: 10.1016/j.heliyon.2024.e25657.

Archer, C., Vance, D., Milne, A. and Lohan, M.C. 2020. The oceanic biogeochemistry of nickel and its isotopes: New data from the South Atlantic and the Southern Ocean biogeochemical divide. *Earth and Planetary Science Letters* 535, p. 116118. doi: https://doi.org/10.1016/j.epsl.2020.116118.

Bau, M. 1999. Scavenging of dissolved yttrium and rare earths by precipitating iron oxyhydroxide: experimental evidence for Ce oxidation, Y-Ho fractionation, and lanthanide tetrad effect. *Geochimica et Cosmochimica Acta* 63, pp. 67–77. doi: 10.1016/S0016-7037(99)00014-9.

Beal, E.J., House, C.H. and Orphan, V.J. 2009. Manganese- and iron-dependent marine methane oxidation. *Science* 325, pp. 184–187.

Beunon, H., Chernonozhkin, S.M., Mattielli, N., Goderis, S., Doucet, L.-S., Debaille, V. and Vanhaecke, F. 2020. Innovative two-step isolation of Ni prior to stable isotope ratio measurements by MC-ICP-MS: application to igneous geological reference materials. *Journal of Analytical Atomic Spectrometry* 35(10), pp. 2213–2223. doi: 10.1039/D0JA00163E.

Beyssac, O., Goffé, B., Chopin, C., and Rouzaud, J.N., 2002, Raman spectra of carbonaceous material in metasediments: a new geothermometer. Journal of Metamorphic Geology, 20, 859–871

Boström, K. 1973. *The origin and fate of ferromanganoan active ridge sediments.* Stockholm: Almqvist & Wiksell distr.

Boström, K. 1983. Genesis of Ferromanganese Deposits-Diagnostic Criteria for Recent and Old Deposits. In: Rona, P. A., Boström, K., Laubier, L., and Smith, K. L. eds. *Hydrothermal Processes at Seafloor Spreading Centers*. Boston, MA: Springer US, pp. 473–489. Available at: https://doi.org/10.1007/978-1-4899-0402-7_20

Bruggmann, S., McManus, J., Archer, C., Vance, D. and Severmann, S. 2024. Nickel's behaviour in marine sediments under aerobic to anaerobic diagenetic conditions. *Chemical Geology* 662, p. 122234. doi: 10.1016/j.chemgeo.2024.122234.

Bucholz, C.E., Biasi, J.A., Beaudry, P., Ono, S., 2020. Sulfur isotope behavior during metamorphism and anatexis of Archean sedimentary rocks: A case study from the Ghost Lake batholith, Ontario, Canada. Earth Planet. Sci. Lett. 549, 116494. https://doi.org/10.1016/j.epsl.2020.116494.

Cameron, V., 2009, A biomarker based on the stable isotopes of nickel. Proceedings of the National Academy of Sciences, 106, 10944–10948. doi: 10.1073/pnas.0900726106.

Cameron, V. and Vance, D. 2014. Heavy nickel isotope compositions in rivers and the oceans. *Geochimica et Cosmochimica Acta* 128, pp. 195–211. doi: 10.1016/j.gca.2013.12.007.

Chen, L.-M. et al. 2023. Nickel isotope ratios trace the process of sulfide-silicate liquid immiscibility during magmatic differentiation. *Geochimica et Cosmochimica Acta* 353, pp. 1–12. doi: https://doi.org/10.1016/j.gca.2023.05.013.

Chernonozhkin, S.M., Goderis, S., Lobo, L., Claeys, P. and Vanhaecke, F. 2015. Development of an isolation procedure and MC-ICP-MS measurement protocol for the study of stable isotope ratio

variations of nickel. *Journal of Analytical Atomic Spectrometry* 30(7), pp. 1518–1530. doi: 10.1039/C5JA00080G.

Ciscato, E.R., Bontognali, T.R.R. and Vance, D. 2018. Nickel and its isotopes in organic-rich sediments: implications for oceanic budgets and a potential record of ancient seawater. *Earth and Planetary Science Letters* 494, pp. 239–250. doi: 10.1016/j.epsl.2018.04.061.

Coldebella, B., LaFlamme, C., Malta, I. S., Guilmette, C., Barré, G., Beaudoin, G., Martin, L., & Savard, D. (2025). The chemical and isotopic characterization of the pyrite to pyrrhotite desulfidation reaction across the metamorphic gradient of a metasedimentary basin. *Geochimica et Cosmochimica Acta*, *392*, 119–136. https://doi.org/10.1016/j.gca.2024.12.027

Collier, R. and Edmond, J. 1984. The trace element geochemistry of marine biogenic particulate matter. *Progress in Oceanography* 13(2), pp. 113–199. doi: 10.1016/0079-6611(84)90008-9.

Condie, K.C. 2001. *Mantle Plumes and Their Record in Earth History*. Cambridge University Press.

Dias, Á.S. and Barriga, F.J.A.S. 2006. Mineralogy and geochemistry of hydrothermal sediments from the serpentinite-hosted Saldanha hydrothermal field (36°34′N; 33°26′W) at MAR. *Marine Geology* 225(1), pp. 157–175. doi: 10.1016/j.margeo.2005.07.013.

DigiKP. Digital map database of the Precambrian bedrock of Finland.http://gtkdata.gtk.fi/Kalliopera/index.html. (Accessed 26th March 2026).

Elliott, T. and Steele, R. 2017. The Isotope Geochemistry of Ni. *Reviews in Mineralogy and Geochemistry*. Available at: https://pubs.geoscienceworld.org/msa/rimg/article-abstract/82/1/511/302284/The-Isotope-Geochemistry-of-Ni?redirectedFrom=fulltext [Accessed: 12 February 2026].

Fike, D.A., Bradley, A.S. and Rose, C.V. 2015. Rethinking the Ancient Sulfur Cycle. *Annual Review of Earth and Planetary Sciences* 43(1), pp. 593–622. doi: 10.1146/annurev-earth-060313-054802.

Fujii, T., Moynier, F., Dauphas, N. and Abe, M. 2011. Theoretical and experimental investigation of nickel isotopic fractionation in species relevant to modern and ancient oceans. *Geochimica et Cosmochimica Acta* 75(2), pp. 469–482. doi: 10.1016/j.gca.2010.11.003.

Gall, L., Williams, H., Siebert, C. and Halliday, A. 2012. Determination of mass-dependent variations in nickel isotope compositions using double spiking and MC-ICPMS. *Journal of Analytical Atomic Spectrometry* 27(1), pp. 137–145. doi: 10.1039/C1JA10209E.

Gall, L., Williams, H.M., Siebert, C., Halliday, A.N., Herrington, R.J. and Hein, J.R. 2013. Nickel isotopic compositions of ferromanganese crusts and the constancy of deep ocean inputs and continental weathering effects over the Cenozoic. *Earth and Planetary Science Letters* 375.

Gueguen, B., Rouxel, O. and Fouquet, Y. 2021. Nickel isotopes and rare earth elements systematics in marine hydrogenetic and hydrothermal ferromanganese deposits. *Chemical Geology* 560, p. 119999. doi: 10.1016/j.chemgeo.2020.119999.

Gueguen, B., Rouxel, O., Ponzevera, E., Bekker, A. and Fouquet, Y. 2013. Nickel Isotope Variations in Terrestrial Silicate Rocks and Geological Reference Materials Measured by MC-ICP-MS. *Geostandards and Geoanalytical Research* 37(3), pp. 297–317. doi: 10.1111/j.1751-908X.2013.00209.x.

He, C., Ji, L., Wu, Y., Su, A. and Zhang, M. 2016. Characteristics of hydrothermal sedimentation process in the Yanchang Formation, south Ordos Basin, China: Evidence from element geochemistry. *Sedimentary Geology* 345, pp. 33–41. doi: 10.1016/j.sedgeo.2016.09.001.

Hein, J.R., Mizell, K., Koschinsky, A. and Conrad, T.A. 2013. Deep-ocean mineral deposits as a source of critical metals for high- and green-technology applications: Comparison with land-based resources. *Ore Geology Reviews* 51, pp. 1–14. doi: 10.1016/j.oregeorev.2012.12.001.

Hiebert, R.S., Bekker, A., Houlé, M.G. and Rouxel, O.J. 2022. Nickel isotope fractionation in komatiites and associated sulfides in the hart deposit, Late Archean Abitibi Greenstone Belt, Canada. *Chemical Geology* 603, p. 120912. doi: 10.1016/j.chemgeo.2022.120912.

Hogmalm, K.J., Zack, T., Karlsson, A.K.-O., Sjöqvist, A.S.L. and Garbe-Schönberg, D. 2017. In situ Rb–Sr and K–Ca dating by LA-ICP-MS/MS: an evaluation of N2O and SF6 as reaction gases. *Journal of Analytical Atomic Spectrometry* 32(2), pp. 305–313. doi: 10.1039/C6JA00362A.

Hrouda, F., Chlupáčová, M., & Mrázová, Š. (2006). Low-field variation of magnetic susceptibility as a tool for magnetic mineralogy of rocks. *Physics of the Earth and Planetary Interiors*, *154*(3-4), 323-336.

Hsu, H.-H., Liu, C.-S., Morita, S., Tu, S.-L., Chen, S.-C., Ku, C.-Y. and Machiyama, H. 2014. Authigenesis of vivianite as influenced by methane-induced sulfidization in cold-seep sediments off southwestern Taiwan. *Journal of Asian Earth Sciences* 92, pp. 214–221.

Itävaara, M., Nyyssönen, M., Kapanen, A., Nousiainen, A., Ahonen, L. and Kukkonen, I. 2011. Characterization of bacterial diversity to a depth of 1500 m in the Outokumpu deep borehole. *FEMS Microbiology Ecology* 77, pp. 295–309.

Jochum, K.P. et al. 2011. Determination of Reference Values for NIST SRM 610–617 Glasses Following ISO Guidelines. *Geostandards and Geoanalytical Research* 35(4), pp. 397–429. doi: 10.1111/j.1751-908X.2011.00120.x.

Jochum, K.P., Stoll, B., Herwig, K. and Willbold, M. 2007. Validation of LA-ICP-MS trace element analysis of geological glasses using a new solid-state 193 nm Nd:YAG laser and matrix-matched calibration. *Journal of Analytical Atomic Spectrometry* 22(2), pp. 112–121. doi: 10.1039/B609547J.

Jochum, K.P., Willbold, M., Raczek, I., Stoll, B. and Herwig, K. 2005. Chemical Characterisation of the USGS Reference Glasses GSA-1G, GSC-1G, GSD-1G, GSE-1G, BCR-2G, BHVO-2G and BIR-1G Using EPMA, ID-TIMS, ID-ICP-MS and LA-ICP-MS. *Geostandards and Geoanalytical Research* 29(3), pp. 285–302. doi: 10.1111/j.1751-908X.2005.tb00901.x.

Klaver, M., Ionov, D.A., Takazawa, E. and Elliott, T. 2020. The non-chondritic Ni isotope composition of Earth's mantle. *Geochimica et Cosmochimica Acta* 268, pp. 405–421. doi: 10.1016/j.gca.2019.10.017.

Kontinen, A. 2012. F029 Talvivaara Ni-Zn-Cu. In: Eilu, P. (Ed.) Mineral Deposits and Metallogeny of Fennoscandia. Geological Survey of Finland, Special Paper 53, 276-280.

Kontinen, A. and Hanski, E. 2015. Chapter 9.1 - The Talvivaara Black Shale-Hosted Ni-Zn-Cu-Co Deposit in Eastern Finland. In: Maier, W. D., Lahtinen, R., and O'Brien, H. eds. *Mineral Deposits of Finland*. Elsevier, pp. 557–612.

Kontinen, A., Sorjonen-Ward, P., Huhma, H. and Lahtinen, H. 2013. Lithostratigraphy, sedimentary environment and origin of the Talvivaara black schist hosted Ni-Zn-Cu-Co deposit. *Tutkimusraportti - Geologian Tutkimuskeskus*, pp. 86–90.

Kumar, A. et al. 2024. Mineralogical compositions and distributions of trace and rare earth elements in Eocene carbonaceous sediments of Western India: implications for paleoenvironment during peat accumulation. *Environmental Earth Sciences* 83(23), p. 649. doi: 10.1007/s12665-024-11967-7.

Lara, R.H., Monroy, M.G., Mallet, M. *et al.* An experimental study of iron sulfides weathering under simulated calcareous soil conditions. *Environ Earth Sci* **73**, 1849–1869 (2015). https://doi.org/10.1007/s12665-014-3540-y

Large, R.R. et al. 2014. Trace element content of sedimentary pyrite as a new proxy for deep-time ocean–atmosphere evolution. *Earth and Planetary Science Letters* 389, pp. 209–220. doi: 10.1016/j.epsl.2013.12.020.

Lecomte, A. et al. 2014. Uraniferous bitumen nodules in the Talvivaara Ni–Zn–Cu–Co deposit (Finland): influence of metamorphism on uranium mineralization in black shales. *Mineralium Deposita* 49(4), pp. 513–533. doi: 10.1007/s00126-013-0502-3.

Lemaitre, N., Du, J., de Souza, G.F., Archer, C. and Vance, D. 2022. The essential bioactive role of nickel in the oceans: Evidence from nickel isotopes. *Earth and Planetary Science Letters* 584, p. 117513. doi: 10.1016/j.epsl.2022.117513.

Liao, S., Tao, C., Li, H., Zhang, G., Liang, J., Yang, W. and Wang, Y. 2018. Surface sediment geochemistry and hydrothermal activity indicators in the Dragon Horn area on the Southwest Indian Ridge. *Marine Geology* 398, pp. 22–34. doi: 10.1016/j.margeo.2017.12.005.

Lim, D. et al. 2022. Characterization of Geochemistry in Hydrothermal Sediments From the Newly Discovered Onnuri Vent Field in the Middle Region of the Central Indian Ridge. *Frontiers in Marine Science* 9. Available at: https://www.frontiersin.org/journals/marine-science/articles/10.3389/fmars.2022.810949/full [Accessed: 27 January 2025].

Little, S.H., Vance, D., Lyons, T.W. and McManus, J. 2015. Controls on trace metal authigenic enrichment in reducing sediments: Insights from modern oxygen-deficient settings. *American Journal of Science* 315(2). Available at: https://ajsonline.org/article/65645 [Accessed: 11 December 2025].

Loukola-Ruskeeniemi, K. 1999. Origin of black shales and the serpentinite-associated Cu-Zn-Co ores at Outokumpu, Finland. *Economic Geology* 94(7), pp. 1007–1028. doi: 10.2113/gsecongeo.94.7.1007.

Loukola-Ruskeeniemi, K. 2011. Graphite- and sulphide-bearing schists in the Outokumpu R2500 Drill Core: Comparison with the Ni-Cu-Co-Zn-Mn-rich black schists at Talvivaara, Finland. *Special Paper of the Geological Survey of Finland* 2011(51), pp. 229–252.

Loukola-Ruskeeniemi, K. and Heino, T. 1996. Geochemistry and genesis of the black shale-hosted Ni-Cu-Zn deposit at Talvivaara, Finland. *Economic Geology* 91(1), pp. 80–110. doi: 10.2113/gsecongeo.91.1.80.

Loukola-Ruskeeniemi, K. and Lahtinen, H. 2013. Multiphase evolution in the black-shale-hosted Ni–Cu–Zn–Co deposit at Talvivaara, Finland. *Ore Geology Reviews* 52, pp. 85–99. doi: 10.1016/j.oregeorev.2012.10.006.

Marchig, V., Gundlach, H., Möller, P. and Schley, F. 1982. Some geochemical indicators for discrimination between diagenetic and hydrothermal metalliferous sediments. *Marine Geology* 50(3), pp. 241–256. doi: 10.1016/0025-3227(82)90141-4.

Marshall, C.P., Love, G.D., Snape, C.E., Hill, A.C., Allwood, A.C., Walter, M.R., Van Kranendonk, M.J., Bowden, S.A., Sylva, S.P. and Summons, R.E. 2007. Structural characterization of kerogen in 3.4 Ga Archaean cherts from the Pilbara Craton, Western Australia. Precambrian Research 155, pp. 1–23.

Martinez, R.E., Pourret, O. and Takahashi, Y. 2014. Modeling of rare earth element sorption to the Gram positive *Bacillus subtilis* bacteria surface. *Journal of Colloid and Interface Science* 413, pp. 106–111. doi: 10.1016/j.jcis.2013.09.037.

Melezhik, V.A., Fallick, A.E., Rychanchik, D.V. and Kuznetsov, A.B. 2005. Palaeoproterozoic evaporites in Fennoscandia: implications for seawater sulphate, the rise of atmospheric oxygen and local amplification of the δ13C excursion. *Terra Nova* 17(2), pp. 141–148. doi: 10.1111/j.1365-3121.2005.00600.x.

Morin, G., Noël, V., Menguy, N., Brest, J., Baptiste, B., Tharaud, M., Ona-Nguema, G., Ikogou, M., Viollier, E., Juillot, F. (2017) Nickel accelerates pyrite nucleation at ambient temperature. *Geochem. Persp. Let.* 5, 6–11.

Moynier, F., Blichert-Toft, J., Telouk, P., Luck, J.-M. and Albarede, F. 2007. Comparative stable isotope geochemistry of Ni, Cu, Zn, and Fe in chondrites and iron meteorites. *Geochimica et Cosmochimica Acta* 71(17), pp. 4365–4379. doi: 10.1016/j.gca.2007.06.049.

Neubeck, A., Callac, N., Isaksson, S. and Schnürer, A. 2025a. Growth of hydrogenotrophic methanogen Methanoculleus bourgensis MAB1 in the presence of dunite. *Anaerobe* 92, p. 102945. doi: https://doi.org/10.1016/j.anaerobe.2025.102945.

Neubeck, A., Szymczak, P., Cameron, V., Buczko, D. and Ivarsson, M. 2025b. Mixed fluid processes in FeMn dendrite formation and associated carbon and nickel isotope fractionation. *Geochemistry* 85(3), p. 126303. doi: 10.1016/j.chemer.2025.126303.

Neuville, D.R. *et al.* (2021). Structure Characterizations and Molecular Dynamics Simulations of Melt, Glass, and Glass Fibers. In: Li, H. (eds) Fiberglass Science and Technology. Springer, Cham. https://doi.org/10.1007/978-3-030-72200-5_2

Nyyssönen, M. et al. 2014. Taxonomically and functionally diverse microbial communities in deep crystalline rocks of the Fennoscandian shield. *ISME Journal* 8, pp. 126–138.

Pandarinath, K. (2022). Impacts of Hydrothermal Alteration on Magnetic Susceptibility and Some Geochemical Properties of Volcanic Rocks from Geothermal Areas. In: Armstrong-Altrin, J.S.,

Pandarinath, K., Verma, S.K. (eds) Geochemical Treasures and Petrogenetic Processes. Springer, Singapore. https://doi.org/10.1007/978-981-19-4782-7_16

Parigi, R., Chen, N., Reid, J.W., Ptacek, C.J. and Blowes, D.W. 2022a. Nickel isotope fractionation during precipitation of Ni secondary minerals and synchrotron-based analysis of the precipitates. *Geochimica et Cosmochimica Acta* 317, pp. 91–105. doi: 10.1016/j.gca.2021.10.027.

Parigi, R., Pakostova, E., Reid, J.W., Saurette, E.M., McBeth, J.M., Ptacek, C.J. and Blowes, D.W. 2022b. Nickel Isotope Fractionation As an Indicator of Ni Sulfide Precipitation Associated with Microbially Mediated Sulfate Reduction. *Environmental Science & Technology* 56(12), pp. 7954–7962. doi: 10.1021/acs.est.2c00523.

Parviainen, A., Mäkilä, M. and Loukola-Ruskeeniemi, K. 2014. Pre-mining acid rock drainage in the Talvivaara Ni–Cu–Zn–Co deposit (Finland): Natural peat layers as a natural analog to constructed wetlands. *Journal of Geochemical Exploration* 143, pp. 84–95. doi: 10.1016/j.gexplo.2014.03.024.

Pašava, J., Chrastný, V., Loukola-Ruskeeniemi, K. and Šebek, O. 2019. Nickel isotopic variation in black shales from Bohemia, China, Canada, and Finland: a reconnaissance study. *Mineralium Deposita* 54, pp. 719–742. doi: 10.1007/s00126-018-0839-8.

Paton, C., Hellstrom, J., Paul, B., Woodhead, J. and Hergt, J. 2011. Iolite: Freeware for the visualisation and processing of mass spectrometric data. *Journal of Analytical Atomic Spectrometry* 26(12), pp. 2508–2518. doi: 10.1039/C1JA10172B.

Peiffer, S., Behrends, T., Hellige, K., Larese-Casanova, P., Wan, M. and Pollok, K. 2015. Pyrite formation and mineral transformation pathways upon sulfidation of ferric hydroxides depend on mineral type and sulfide concentration. *Chemical Geology* 400, pp. 44–55. doi: 10.1016/j.chemgeo.2015.01.023.

Raiswell, R., & Canfield, D. E. (1996). Rates of reaction between silicate iron and dissolved sulfide in Peru Margin sediments. *Geochimica et Cosmochimica Acta*, *60*(15), 2777–2787. https://doi.org/10.1016/0016-7037(96)00141-X

Ratié, G. et al. 2015. Nickel isotope fractionation during tropical weathering of ultramafic rocks. *Chemical Geology* 402, pp. 68–76. doi: https://doi.org/10.1016/j.chemgeo.2015.02.039.

Ratnayake, D.M., Tanaka, R. and Nakamura, E. 2021. Novel nickel isolation procedure for a wide range of sample matrices without using dimethylglyoxime for isotope measurements using MC-ICP-MS. *Analytica Chimica Acta* 1181, p. 338934. doi: 10.1016/j.aca.2021.338934.

Riboulleau, A., Baudin, F., Deconinck, J.-F., Derenne, S., Largeau, C. and Tribovillard, N. 2003. Depositional conditions and organic matter preservation pathways in an epicontinental environment: the Upper Jurassic Kashpir Oil Shales (Volga Basin, Russia). *Palaeogeography, Palaeoclimatology, Palaeoecology* 197(3), pp. 171–197. doi: https://doi.org/10.1016/S0031-0182(03)00460-7.

Rickard, D. 2014. The Sedimentary Sulfur System: Biogeochemistry and Evolution through Geologic Time. In: Holland, H.D. and Turekian, K.K. (eds.) *Treatise on Geochemistry*, 2nd edition, vol. 9, pp. 267–326.

Rickard, D., & Luther, G. W. (2007). Chemistry of Iron Sulfides. *Chemical Reviews*, *107*(2), 514–562. https://doi.org/10.1021/cr0503658

Riedinger, N., Formolo, M.J., Lyons, T.W., Henkel, S., Beck, A. and Kasten, S. 2014. An inorganic geochemical argument for coupled anaerobic oxidation of methane and iron reduction in marine sediments. *Geobiology* 12, pp. 172–181.

Rösel, D. and Zack, T. 2022. LA-ICP-MS/MS Single-Spot Rb-Sr Dating. *Geostandards and Geoanalytical Research* 46(2), pp. 143–168. doi: 10.1111/ggr.12414.

Rudnick, R.L. and Gao, S. 2003. Composition of the Continental Crust. *Treatise on Geochemistry* 3, p. 659. doi: 10.1016/B0-08-043751-6/03016-4.

Scherer, P., Lippert, H. and Wolff, G. 1983. Composition of the major elements and trace elements of 10 methanogenic bacteria determined by inductively coupled plasma emission spectrometry. *Biological Trace Element Research* 5(3), pp. 149–163. doi: 10.1007/BF02916619.

Slack, J.F., Grenne, T. and Bekker, A. 2009. Seafloor-hydrothermal Si-Fe-Mn exhalites in the Pecos greenstone belt, New Mexico, and the redox state of ca. 1720 Ma deep seawater. *Geosphere* 5(3), pp. 302–314. doi: 10.1130/GES00220.1.

Sorensen, J.V., Gueguen, B., Stewart, B.D., Peña, J., Rouxel, O. and Toner, B.M. 2020. Large nickel isotope fractionation caused by surface complexation reactions with hexagonal birnessite. *Chemical Geology* 537, p. 119481. doi: 10.1016/j.chemgeo.2020.119481.

Spivak-Birndorf, L.J., Wang, S.-J., Bish, D.L. and Wasylenki, L.E. 2018. Nickel isotope fractionation during continental weathering. *Chemical Geology* 476, pp. 316–326. doi: 10.1016/j.chemgeo.2017.11.028.

Steele, R.C.J., Elliott, T., Coath, C.D. and Regelous, M. 2011. Confirmation of mass-independent Ni isotopic variability in iron meteorites. *Geochimica et Cosmochimica Acta* 75(24), pp. 7906–7925. doi: 10.1016/j.gca.2011.08.030.

Su, G. et al. 2019. Manganese/iron-supported sulfate-dependent anaerobic oxidation of methane by archaea in lake sediments. *Science of the Total Environment* 657, pp. 1574–1583.

Tribovillard, N., Algeo, T.J., Lyons, T. and Riboulleau, A. 2006. Trace metals as paleoredox and paleoproductivity proxies: An update. *Chemical Geology* 232(1–2), pp. 12–32. doi: 10.1016/j.chemgeo.2006.02.012.

Virtasalo, J.J., Laitala, J.J., Lahtinen, R. and Whitehouse, M.J. 2015. Pyritic event beds and sulfidized Fe (oxyhydr)oxide aggregates in metalliferous black mudstones of the Paleoproterozoic Talvivaara formation, Finland. *Earth and Planetary Science Letters* 432, pp. 449–460. doi: 10.1016/j.epsl.2015.09.010.

Wang, S.-J. and Wasylenki, L.E. 2017. Experimental constraints on reconstruction of Archean seawater Ni isotopic composition from banded iron formations. *Geochimica et Cosmochimica Acta* 206, pp. 137–150. doi: 10.1016/j.gca.2017.02.023.

Watkins, J.M., DePaolo, D.J. and Watson, E.B. 2017. Kinetic Fractionation of Non-Traditional Stable Isotopes by Diffusion and Crystal Growth Reactions. *Reviews in Mineralogy and Geochemistry* 82(1), pp. 85–125. doi: 10.2138/rmg.2017.82.4.

Wedepohl, K.H. 1971. Environmental influences on the chemical composition of shales and clays. *Physics and Chemistry of the Earth* 8, pp. 305–333. doi: 10.1016/0079-1946(71)90020-6.

Wilson, S.A., Ridley, W.I. and Koenig, A.E. 2002. Development of sulfide calibration standards for the laser ablation inductively-coupled plasma mass spectrometry technique. *Journal of Analytical Atomic Spectrometry* 17(4), pp. 406–409. doi: 10.1039/B108787H.

Wopenka B., Pasteris, J. D.; Structural characterization of kerogens to granulite-facies graphite: Applicability of Raman microprobe spectroscopy. *American Mineralogist* 1993;; 78 (5-6): 533–557.

Worm, D. Clark, M. J. Dekkers, Magnetic susceptibility of pyrrhotite: grain size, field and frequency dependence, *Geophysical Journal International*, Volume 114, Issue 1, July 1993, Pages 127–137, https://doi.org/10.1111/j.1365-246X.1993.tb01472.x

Yang, Y.-H. et al. 2014. Sr and Nd isotopic compositions of apatite reference materials used in U–Th–Pb geochronology. *Chemical Geology* 385, pp. 35–55. doi: 10.1016/j.chemgeo.2014.07.012.

Young, S., Loukola-Ruskeeniemi, K. and Pratt, L. 2013. Reactions of hydrothermal solutions with organic matter in Paleoproterozoic black shales at Talvivaara, Finland: Evidence from multiple sulfur isotopes. *Earth and Planetary Science Letters* 367, pp. 1–14. doi: 10.1016/j.epsl.2013.02.004.

Zack, T. and Hogmalm, J. 2016. Laser ablation Rb/Sr dating by online chemical separation of Rb and Sr in an oxygen-filled reaction cell. *Chemical Geology* 437. doi: 10.1016/j.chemgeo.2016.05.027.

Zhao, J., Jin, Z., Jin, Z., Geng, Y., Wen, X. and Yan, C. 2016. Applying sedimentary geochemical proxies for paleoenvironment interpretation of organic-rich shale deposition in the Sichuan Basin, China. *International Journal of Coal Geology* 163, pp. 52–71. doi: https://doi.org/10.1016/j.coal.2016.06.015.

Zhao, Z. et al. 2021. Active methanogenesis during the melting of Marinoan snowball Earth. *Nature Communications* 12(1), p. 955. doi: 10.1038/s41467-021-21114-6.

SUPPLEMENTARY MATERIAL

Title: Nickel Isotope Systematics in the Talvivaara Paleoproterozoic Black Shale Deposit Reveal Mineralogy-Controlled Fractionation with a Preserved Biogenic Signal

Neubeck A[1], Loukola-Ruskeeniemi K[2], Cameron V.[1], Rösel D.[3], Roud, S.[4], Jonathan A. Lewis[1], John Manrique Carreño[1], Buczko D[1], Bohlin M[5], Tranchet P-A[6], Almqvist B.[1]

[1]Department of Earth Sciences, Uppsala University, Sweden
[2]Geological Survey of Finland
[3]Department of Earth Sciences, University of Gothenburg, Sweden
[4]GFZ Helmholtz Center for Geosciences, Telegrafenberg, 14473 Potsdam, Germany
[5]Department of geological Sciences, Stockholm University, Sweden
[6]Institute of Geology, University of Hamburg, Germany

Table S1.

	P		**S**		**Mn**		**Fe**		**Ni**	
Depth (m) SILICATES	µg/g	2se	µg/g	2se	µg/g	2se	µg/g	2se	µg/g	2se
82,4	175,00	22,00	2667,00	619,00	26,00	7,00	2020,00	322,00	19,90	4,10
82,4	137,00	19,00	156021,00	6337,00	11590,00	815,00	82468,00	16629,00	268,10	66,20
82,4	148,00	20,00	7563,00	1220,00	174,00	26,00	7066,00	1056,00	28,90	4,50
82,4	122,00	9,00	1469,00	289,00	7490,00	408,00	15826,00	845,00	19,00	2,30
82,4	104,00	8,00	1163,00	409,00	9798,00	318,00	21937,00	1196,00	45,80	3,60
82,4	176,00	30,00	185222,00	4665,00	119,00	10,00	137528,00	12246,00	271,30	33,90
82,4	265,00	28,00	7409,00	1560,00	103,00	49,00	3723,00	710,00	4,80	1,40
82,4	160,00	15,00	531,00	332,00	6114,00	350,00	12481,00	756,00	12,90	1,50
82,4	190,00	24,00	105251,00	9086,00	227,00	29,00	81044,00	6606,00	117,10	10,80
82,4	183,00	21,00			171,00	8,00	1480,00	143,00	8,70	1,20
82,4	140,00	11,00	833,00	333,00	366,00	27,00	2019,00	184,00	9,90	1,80
82,4	121,00	10,00	611,00	467,00	922,00	80,00	2046,00	203,00	3,80	0,70
118,7	143,00	17,00	1035,00	253,00	5061,00	162,00	2100,00	102,00	1,20	0,60
118,7	136,00	23,00	67527,00	8039,00	4532,00	556,00	103798,00	16081,00	489,80	65,80
118,7	145,00	10,00	1279,00	275,00	5953,00	128,00	2705,00	77,00		
118,7	157,00	9,00	694,00	124,00	5433,00	153,00	2162,00	94,00	3,10	0,60
118,7	120,00	30,00	7946,00	3871,00	7946,00	405,00	18617,00	5801,00	8,90	0,50
118,7	120,00	28,00	152323,00	36557,00	2277,00	518,00	130127,00	35489,00	60,60	14,80
118,7	163,00	13,00	4518,00	802,00	3917,00	355,00	5938,00	443,00	2,80	1,90
118,7	184,00	10,00	816,00	113,00	1000,00	84,00	681,00	170,00	5,30	1,20
118,7	161,00	12,00	2387,00	281,00	7139,00	155,00	4802,00	286,00	3,90	0,80
147,6	136,00	15,00	221999,00	19088,00	156,00	6,00	280353,00	34457,00	1660,20	156,60
147,6	126,00	6,00			6626,00	93,00	8141,00	143,00	31,00	1,30
147,6	122,00	25,00			6897,00	505,00	8281,00	91,00	30,30	6,80
147,6	124,00	9,00			6882,00	133,00	8841,00	165,00	32,30	1,90
147,6	135,00	9,00	970,00	210,00	6239,00	146,00	7787,00	195,00	31,70	1,10
147,6	120,00	10,00	904,00	297,00	6747,00	93,00	8267,00	133,00	29,30	1,20
147,6	113,00	13,00	1353,00	304,00	7195,00	230,00	9510,00	268,00	45,90	3,80
147,6	147,00	15,00	53971,00	1861,00	6079,00	76,00	43331,00	3416,00	154,60	13,50
147,6	189,00	11,00	13876,00	2952,00	1393,00	188,00	10506,00	2765,00	142,70	16,90
147,6	386,00	68,00	10391,00	3205,00	1518,00	125,00	9292,00	2958,00	64,90	7,70
147,6	188,00	22,00	8082,00	1816,00	405,00	43,00	7228,00	1925,00	19,40	3,40
147,6	552,00	143,00	199802,00	28919,00	4056,00	568,00	154133,00	22714,00	210,90	30,80
147,6	117,00	9,00	762,00	305,00	5780,00	137,00	6954,00	245,00	26,10	1,60
147,6	119,00	14,00	535,00	59,00	6448,00	108,00	8290,00	216,00	30,20	2,30
147,6	125,00	25,00	1005,00	1216,00	5240,00	224,00	6682,00	160,00	21,00	1,50

147,6	140,00	13,00	614,00	228,00	6483,00	146,00	8443,00	175,00	32,20	1,90
147,6	128,00	12,00	582,00	280,00	7416,00	190,00	9453,00	257,00	37,60	2,40
147,6	155,00	11,00	100226,00	3282,00	2808,00	154,00	97220,00	12720,00	27530,40	7813,90
147,6	127,00	31,00	1939,00	762,00	8995,00	412,00	13961,00	1124,00	166,80	40,30
147,6	119,00	26,00	133603,00	6620,00	2309,00	38,00	149301,00	10238,00	15049,50	307,10
147,6	121,00	8,00	643,00	398,00	6604,00	173,00	8363,00	327,00	31,40	1,40
147,6	117,00	8,00	465,00	191,00	6277,00	108,00	7678,00	127,00	30,60	1,20
147,6	145,00	11,00	1108,00	127,00	6982,00	199,00	8948,00	152,00	34,20	2,30
147,6	149,00	12,00	723,00	115,00	8199,00	192,00	10624,00	250,00	43,40	2,00
147,6	98,00	12,00	605,00	138,00	6727,00	154,00	8320,00	134,00	31,40	1,80
147,6	123,00	11,00	161742,00	26266,00	943,00	154,00	161338,00	47132,00	654,40	42,60
152,3	143,00	6,00	986,00	59,00	8972,00	172,00	2271,00	34,00	11,30	0,50
152,3	125,00	9,00	48912,00	9982,00	10382,00	671,00	25434,00	6335,00	1021,20	208,00
152,3	146,00	8,00	29394,00	3253,00	9971,00	498,00	12849,00	1893,00	177,30	13,90
152,3	141,00	7,00	1382,00	87,00	7469,00	238,00	8294,00	156,00	3,10	0,50
152,3	146,00	5,00	1004,00	88,00	8097,00	128,00	7915,00	119,00		
152,3	138,00	6,00	1120,00	72,00	9354,00	260,00	12125,00	214,00	6,40	1,50
152,3	148,00	4,00	948,00	78,00	5252,00	105,00	2231,00	61,00	12,30	0,90
152,3	124,00	15,00	727,00	125,00	8909,00	87,00	5236,00	182,00	0,90	0,40
152,3	124,00	11,00	925,00	177,00	8541,00	215,00	5842,00	122,00	1,10	0,50
152,3	136,00	11,00	845,00	155,00	6266,00	70,00	7462,00	130,00		
152,3	153,00	10,00	1425,00	173,00	11506,00	545,00	15433,00	273,00		
152,3	144,00	9,00	998,00	182,00	8466,00	162,00	8808,00	221,00	2,70	0,40
152,3	148,00	5,00	1123,00	197,00	4332,00	264,00	1912,00	122,00	9,10	1,00
152,3	179,00	17,00	1598,00	224,00	4651,00	142,00	1945,00	40,00	11,50	0,80
152,3	177,00	12,00	1141,00	308,00	4287,00	119,00	1858,00	64,00	9,30	1,20
152,3	187,00	7,00	1291,00	782,00	3887,00	193,00	1734,00	34,00	12,50	4,70
152,3	149,00	8,00	744,00	117,00	9226,00	451,00	10327,00	506,00		
152,3	167,00	22,00	1692,00	441,00	8755,00	200,00	12232,00	546,00	194,80	61,90
155,9	116,00	10,00	3447,00	2872,00	11113,00	229,00	20189,00	331,00	13,60	2,40
155,9	119,00	18,00	25559,00	1370,00	10943,00	180,00	24902,00	1437,00	135,30	15,60
155,9	109,00	13,00	1133,00	216,00	10777,00	394,00	17449,00	508,00	8,40	1,50
155,9	109,00	9,00	919,00	285,00	8941,00	105,00	12863,00	255,00	6,80	0,50
176,6	145,00	56,00	183656,00	28383,00	303,00	62,00	195135,00	38369,00	218,20	48,20
176,6	210,00	3,00	15562,00	2697,00	4228,00	161,00	23577,00	4161,00	34,50	6,90
176,6	248,00	74,00	19511,00	2573,00	2323,00	206,00	25462,00	2581,00	30,50	6,20
176,6	1653,00	188,00	112172,00	18003,00	811,00	69,00	107685,00	20034,00	209,10	36,30
176,6	286,00	21,00	7506,00	2172,00	577,00	104,00	6230,00	813,00	33,50	3,50
176,6	268,00	38,00	133317,00	11296,00	1432,00	27,00	107654,00	13578,00	143,50	13,60
176,6	150,00	16,00	116676,00	12614,00	2801,00	323,00	98591,00	10470,00	143,10	19,20
176,6	148,00	13,00	2976,00	529,00	3616,00	198,00	7254,00	539,00	22,80	2,70
176,6	22443,00	2577,00	143118,00	13630,00	1646,00	83,00	136320,00	24105,00	156,30	15,80
176,6	155,00	33,00	76009,00	8776,00	3037,00	291,00	40095,00	7117,00	61,70	3,50
176,6	117,00	15,00	334823,00	17772,00	966,00	183,00	251954,00	18883,00	314,50	24,80
176,6	2555,00	735,00	1856,00	382,00	2975,00	128,00	1587,00	95,00	10,50	2,30
176,6	158,00	12,00	57360,00	11836,00	1688,00	364,00	42877,00	4130,00	115,40	30,40
176,6	160,00	31,00	1794,00	359,00	1060,00	38,00	780,00	80,00	4,70	1,50
176,6	327,00	38,00	19420,00	1826,00	851,00	44,00	20245,00	8755,00	119,00	32,80
176,6	1102,00	398,00	7963,00	2059,00	9025,00	3185,00	12741,00	2522,00	95,60	37,20
176,6	1120,00	35,00	187765,00	12909,00	1541,00	154,00	144109,00	15408,00	806,60	99,70
272,9	139,00	25,00	881,00	675,00	19399,00	925,00	99081,00	3047,00	153,60	6,20
272,9	196,00	13,00	1506,00	268,00	6076,00	102,00	7378,00	166,00	167,40	6,30
272,9	185,00	26,00	5841,00	363,00	4300,00	162,00	4862,00	200,00	200,30	7,50
272,9	177,00	15,00	877,00	225,00	5403,00	147,00	6229,00	183,00	149,50	12,80
272,9	170,00	15,00	504,00	209,00	5641,00	77,00	7176,00	180,00	84,90	2,50
272,9	189,00	19,00	802,00	229,00	6509,00	301,00	8824,00	492,00	220,60	11,90
272,9	158,00	13,00	1118,00	416,00	7285,00	212,00	10622,00	309,00	487,40	27,40
272,9	155,00	14,00	1136,00	592,00	7143,00	493,00	10084,00	521,00	279,50	17,40
272,9	199,00	17,00	1097,00	238,00	5322,00	91,00	6800,00	245,00	169,50	10,90
272,9	190,00	15,00	803,00	180,00	5146,00	128,00	5018,00	119,00	144,70	10,10
272,9	163,00	12,00	1257,00	137,00	5014,00	76,00	6314,00	99,00	163,90	10,80
272,9	159,00	15,00	2096,00	363,00	12533,00	817,00	47165,00	4441,00	1224,90	66,60
272,9	167,00	13,00	2357,00	264,00	15042,00	849,00	55379,00	6967,00	1963,30	51,80
272,9	182,00	7,00	966,00	177,00	7282,00	127,00	8282,00	164,00	552,70	21,80
272,9	180,00	33,00	21942,00	2186,00	1067,00	70,00	56830,00	7152,00	682,30	65,70
272,9	63,00	19,00	1714,00	197,00	1649,00	295,00	3043,00	362,00	150,10	45,60
272,9	166,00	57,00	1606,00	442,00	3311,00	106,00	10763,00	500,00	365,20	34,10

	P		**S**		**Mn**		**Fe**		**Ni**	
	µg/g	2se	µg/g	2se	µg/g	2se	µg/g	2se	µg/g	2se
Depth (m)	SULFIDES									
82,4	128,6	25,2	441495	41576	45,0	8,4	465777,0	60679,4	598	46
82,4	102,2	9,7	513849	11678	0,5	0,2	484303,0	31348,9	625	26
82,4	136,0	25,9	343643	17335	44,0	4,4	539519,1	22435,3	4144	216

82,4	126,9	10,8	509710	36936	160,8	8,5	384612,6	11965,9	735	20
82,4	193,2	18,6	463330	26340	213,3	12,9	357823,3	13541,7	671	17
82,4	142,6	10,6	534670	21473	87,3	6,1	379310,4	14211,9	831	24
82,4	151,9	13,3	391491	7295			602895,5	8715,9	4498	121
82,4	79,8	8,4	534351	13259			464121,8	26366,0	598	32
82,4	81,7	9,0	549517	21763			449034,1	19213,9	762	39
82,4	130,5	10,2	364448	6396	22647,6	1061,6	221167,9	16643,8	284	17
82,4	147,4	12,9	259480	3071	34897,6	421,2	58494,1	4604,2	5	1
82,4	182,2	8,3	263218	3953	36753,4	717,6	64074,9	5561,0	5	1
82,4	155,4	31,6	279558	6135	35754,7	1104,8	60704,0	6988,9	5	1
82,4	210,3	68,0	452883	10892	2474,0	680,4	309254,3	58742,1	1317	93
118,88	84,1	6,6	526347	23627			472208,7	30172,8	637	34
118,88	94,6	5,6	534130	22675	1,0	0,4	463929,9	24598,1	1094	60
118,88	87,3	7,2	548485	18503			449757,4	21022,1	856	41
118,88	197,3	16,7	365841	11128	572777,8	14349,3	59788,9	7035,4	12	1
118,88	198,9	9,0	371791	7887	568270,4	7720,4	58488,1	5131,9	10	1
118,88	199,0	8,9	373830	5775	569756,4	13199,0	54995,8	5154,8	9	1
118,88	174,0	10,8	396369	4913	42,2	2,6	600102,2	5161,2	2291	44
118,88	146,9	13,0	403553	8973	28,1	2,0	592301,0	7384,5	2921	63
118,88	162,7	9,4	406262	8986	31,8	1,2	589660,5	9596,7	2900	72
147,55	87,6	6,8	570093	27996	21,1	5,1	425126,6	34948,2	1726	111
147,55	123,1	17,6	536305	15411	367,6	84,4	439769,8	50453,8	1794	211
147,55	84,4	11,9	538546	16690	1,7	0,4	458533,8	43372,9	1031	44
147,55	128,0	23,3	557091	15083	16,9	3,2	415430,4	40554,5	1388	125
147,55	69,7	6,0	499266	25756			497840,0	30041,8	1455	90
147,55	185,6	65,5	314199	79257	5621,8	2456,1	272904,1	19637,4	999	136
147,55	77,7	8,7	510580	29547	11,0	2,8	485780,6	21465,8	1583	75
147,55	85,5	8,5	528424	20535	3,3	0,9	469542,9	25486,7	696	39
152,27	281,0	39,8	381181,1	14466,1	625,80	48,9	568912,9	7023,4	32656	3413,5
152,27	284,7	19,4	389327,4	42993,2	838,14	92,2	569391,4	9982,8	23687	1252,7
152,27	279,5	42,2	401095,4	19383,8	216250,56	79116,1	263720,2	71678,6	11551	1740,6
152,27	267,0	24,5	467314	21574	724,8	89,0	489077,6	8675,2	24552	2054
152,27	225,3	20,0	475640	18639	785,6	47,7	477271,2	6907,1	29018	4009
152,27	308,5	22,6	469780	16120	471,6	30,5	491255,8	12835,5	26921	1670
152,27										
152,27										
152,27	73,9	5,3	548983	21720	0,1	0,1	445460,8	19330,4	2021	60
155,9	132,7	15,3	515751	14795	171,8	8,4	383571,7	18030,5	598	24
155,9	147,1	12,1	447313	28117	235,9	14,9	355294,0	19308,5	613	35
155,9	162,6	10,1	488147	17494	204,4	8,6	359834,0	26488,6	795	29
155,9	80,4	8,5	525552	21844			472996,5	23357,9	713	42
155,9	90,0	8,5	524878	23100			473890,1	26576,1	532	46
155,9	78,5	4,7	525618	18536			473055,8	23360,8	568	27
155,9	197,9	10,0	370387	6743	3,4	0,3	622249,4	8188,8	5974	162
155,9	192,8	9,8	381761	7669	3,6	0,3	610054,0	6484,4	6955	171
176,55	195,1	29,8	329089	1843	33238,8	4134,2	82683,5	15062,8	28	9
176,55	175,9	10,8	262752	4157	49237,3	293,5	81518,7	3811,1	1	0
272,88	179,5	15,5	272964	9080	1103,9	187,2	322780,5	15004,4	380235	18076
272,88	144,6	11,0	302774	7522	15,0	5,8	289149,3	11096,4	401339	15036
272,88	137,4	29,1	303299	18331	147,7	49,0	285101,1	9679,8	402563	30221
272,88	206,7	14,9	367848	5016	27,5	1,6	622582,2	7606,9	8355	174
272,88	179,5	8,8	364985	5872	30,1	2,5	626861,1	10094,2	6858	364
272,88	188,8	15,9	376631	7010	21,1	0,9	612966,4	9835,2	9317	454
272,88	187,3	9,8	379279	4115	15,2	1,0	609690,4	11797,2	9755	1341
272,88	188,5	13,7	368301	7683	13,2	0,7	624269,8	7061,8	6243	187
272,88	183,2	15,7	268550	2416	41481,2	272,0	71568,6	4030,8	8	3
272,88	121,8	12,8	286213	6001	37567,6	2639,9	101534,1	17346,3	325	61
272,88	187,2	16,9	381603	15977	116,6	9,8	603886,6	16879,7	7065	1087
272,88	149,0	22,0	350495	6397	12781,3	567,1	423222,2	28300,8	2328	203
272,88	170,2	12,8	268865	3737	37108,8	1134,9	90069,9	5618,1	225	23
272,88	172,2	19,7	376625	11556	418,1	245,9	614841,1	10381,7	3812	320
272,88	166,7	26,4	261428	1752	36710,4	722,5	69474,6	4672,8	4	1
272,88	174,7	16,1	303250	4460	27009,0	9769,2	287329,5	49608,2	1598	109
272,88	204,7	21,2	272167	2732	44584,6	742,8	75798,4	1783,5	10	2
272,88	162,1	12,5	370911	10324	1,3	0,3	623130,1	8831,2	4549	70
272,88	189,6	17,5	274766	2298	47155,8	430,3	79682,0	3789,9	14	1

***Table S2**. Variation of REE values (normalized to PAAS and CI) of silicates and sulfides with depth.*

SILICATES

NORMALISED	La	Ce	Pr	Nd	Sm	Eu	Gd	Tb	Dy	Y	Ho	Er	Tm	Yb	Lu
REF data (Palme & O´Neil 2014)	0,2414	0,6194	0,0939	0,4737	0,1536	0,05883	0,2069	0,03797	0,2558	1,46	0,05644	0,1655	0,02609	0,1687	0,02503
82,4	7,954	3,660	4,100	4,285	10,156	13,466	1,402	4,609	1,329	2,178	5,079	1,782	11,882	8,121	5,194
118,68	2,937	2,571	3,674	4,159	7,227	7,394	9,199	9,850	14,504	18,138	20,801	29,257	31,736	52,756	78,466
147,55	3,167	1,521	2,159	2,088	2,778	12,069	2,964	4,082	5,317	1,449	10,454	7,492	14,565	19,621	25,969
152,27	24,243	6,922	3,970	2,932	4,525	5,817	6,277	4,609	4,882	3,096	4,828	5,249	4,919	5,891	5,443
155,9	4,722	1,481	1,988	3,494	3,320	-	2,932	3,160	2,489	1,449	2,746	2,014	1,725	3,883	2,996
176,55	2758,353	1572,510	1558,772	1425,339	831,105	68,267	515,453	214,731	201,964	84,979	146,567	147,039	176,313	225,390	184,828
272,88	155,446	89,357	105,958	105,440	102,348	71,392	102,575	75,639	75,030	88,959	74,439	76,838	73,181	69,374	71,461
NORMALISED	La	Ce	Pr	Nd	Sm	Eu	Gd	Tb	Dy	Y	Ho	Er	Tm	Yb	Lu
REF data PAAS	38	80	8,9	32	5,6	1,1	4,7	0,77	4,4		1	2,9	0,4	2,8	0,433
82,4	0,051	0,028	0,043	0,063	0,279	0,720	0,062	0,227	0,077	0,118	0,287	0,102	0,775	0,489	0,300
118,68	0,019	0,020	0,039	0,062	0,198	0,395	0,405	0,486	0,843	0,981	1,174	1,670	2,070	3,179	4,536
147,55	0,020	0,012	0,023	0,031	0,076	0,645	0,130	0,201	0,309	0,078	0,590	0,428	0,950	1,182	1,501
152,27	0,154	0,054	0,042	0,043	0,124	0,311	0,276	0,227	0,284	0,167	0,273	0,300	0,321	0,355	0,315
155,9	0,030	0,011	0,021	0,052	0,091	#DIV/0!	0,129	0,156	0,145	0,078	0,155	0,115	0,113	0,234	0,173
176,55	17,523	12,175	16,446	21,099	22,796	3,651	22,691	10,589	11,741	4,595	8,272	8,391	11,500	13,580	10,684
272,88	0,987	0,692	1,118	1,561	2,807	3,818	4,515	3,730	4,362	4,810	4,201	4,385	4,773	4,180	4,131

SULFIDES

NORMALISED	La	Ce	Pr	Nd	Sm	Eu	Gd	Tb	Dy	Y	Ho	Er	Tm	Yb	Lu
REF data (Palme & O´Neil 2014) CA	0,2414	0,6194	0,0939	0,4737	0,1536	0,05883	0,2069	0,03797	0,2558	1,46	0,05644	0,1655	0,02609	0,1687	0,02503
82,4	1,157	1,968	3,683	5,119	34,772	25,730	62,064	65,078	86,896	16,230	104,961	120,616	109,582	114,493	164,243
118,68	-	-	-	-	-	-	-	-	-	-	-	-	-	-	-
147,55	1,132	0,689	1,315	1,867	-	0,561	2,243	-	0,379	0,476	-	0,429	-	-	-
152,27	0,635	0,280	-	-	-	-	-	-	-	-	-	-	-	-	-
155,9	2,476	0,388	0,309	0,402	-	-	1,252	1,106	1,402	2,065	1,536	2,081	2,185	1,838	2,624
176,55	-	-	-	-	-	-	-	-	-	0,057	-	-	-	-	-
272,88	0,000	0,000	0,485	0,562	-	-	-	-	-	0,058	-	-	-	-	-
NORMALISED	La	Ce	Pr	Nd	Sm	Eu	Gd	Tb	Dy	Y	Ho	Er	Tm	Yb	Lu
REF data PAAS	38	80	8,9	32	5,6	1,1	4,7	0,77	4,4	26.7	1	2,9	0,4	2,8	0,433
82,4	0,007	0,015	0,039	0,076	0,954	1,376	2,732	3,209	5,052	0.89	5,924	6,883	7,148	6,898	9,494
118,68	-	-	-	-	-	-	-	-	-	-	-	-	-	-	-
147,55	0,007	0,005	0,014	0,028	-	0,030	0,099	-	0,022	0.03	-	0,024	-	-	-
152,27	0,004	0,002	-	-	-	-	-	-	-	-	-	-	-	-	-
155,9	0,016	0,003	0,003	0,006	-	-	0,055	0,055	0,082	0.11	0,087	0,119	0,143	0,111	0,152
176,55	-	-	-	-	-	-	-	-	-	-	-	-	-	-	-
272,88	0,000	0,000	0,005	0,008	-	-	-	-	-	-	-	-	-	-	-

Table S3. *EPMA spot element analyses.*

Sample	Si(Mass%)	As(Mass%)	S(Mass%)	P(Mass%)	Ni(Mass%)	Mn(Mass%)	Fe(Mass%)	Total (Mass%)
depth_82.40mA_point1	0	0,07	54,933	0,003	0,081	0	47,395	102,482
depth_82.40mA_point2	0	0,11	54,84	0,005	0,061	0,003	46,969	101,988
depth_82.40mA_point3	0,005	0,081	54,886	0	0,069	0,002	47,284	102,327
depth_82.40mA_point4	0,022	0,123	54,777	0	0,041	0,001	46,951	101,915
depth_82.40mA_point5	0,012	0,072	54,902	0,004	0,055	0	47,114	102,159
depth_82.40mA_point6	0,013	0,068	54,053	0,001	0,036	0,003	46,726	100,9
depth_82.40mA_point7	0,028	0	40,049	0	0,305	0	59,792	100,174
depth_82.40mA_point8	0,023	0,081	54,974	0	0,022	0,005	47,44	102,545
depth_82.40mA_point9	0,006	0,054	54,73	0	0,07	0	47,399	102,259
depth_82.40mB_point10	0,016	0,067	55,272	0,003	0,066	0,001	47,343	102,768
depth_82.40mB_point11	0,021	0,076	55,201	0,001	0,043	0	47,336	102,678
depth_82.40mB_point12	0,013	0,106	55,218	0,002	0,052	0	46,88	102,271
depth_82.40mB_point13	0,014	0,051	55,169	0	0,047	0	47,49	102,771
depth_82.40mB_point14	0,005	0,122	54,872	0	0,039	0	47,064	102,102
depth_82.40mB_point15	0,023	0,151	54,951	0,002	0,023	0	46,952	102,102
depth_82.40mB_point16	0,02	0	29,021	0	0	5,876	11,14	46,057
depth_82.40mB_point17	0,024	0,128	54,477	0	0,052	0,005	46,902	101,588
depth_82.40mC_point18	0,01	0,03	54,665	0	0,009	0,009	47,034	101,757
depth_82.40mC_point19	0,009	0,095	54,672	0	0,044	0	47,108	101,928
depth_82.40mC_point20	0	0,13	54,302	0	0,083	0,01	46,877	101,402
depth_82.40mC_point21	0,033	0	28,019	0,004	0,007	5,724	10,454	44,241
depth_82.40mC_point22	0,021	0	28,786	0,003	0,009	6,04	10,333	45,192
depth_82.40mC_point23	0,026	0	28,819	0,001	0,018	5,923	10,463	45,25
depth_82.40mC_point24	0,027	0,095	54,488	0	0,054	0,029	46,708	101,401
depth_82.40mC_point25	0,002	0,094	55,35	0	0,069	0,021	47,415	102,951
depth_82.40mC_point26	0,008	0,091	54,866	0,002	0,062	0,047	47,014	102,09
depth_82.40mA_point27	0,015	0	28,655	0	0	6,047	10,553	45,27
depth_82.40mA_point28	0,004	0,095	54,777	0,004	0,056	0	47,314	102,25
depth_82.40mA_point29	0	0,116	54,929	0,003	0,057	0,007	47,5	102,612
depth_82.40mA_point30	0	0,081	54,588	0	0,038	0	47,473	102,18
depth_82.40mA_point31	0,01	0,097	54,838	0	0,063	0,005	46,862	101,875
depth_82.40mA_point32	0,03	0,093	55,299	0,003	0,062	0	47,337	102,824
depth_82.40mA_point33	0,032	0	29,037	0,004	0,001	5,956	10,468	45,498
depth_82.40mA_point34	0,027	0,004	28,64	0,006	0	5,506	10,498	44,681
depth_82.40mA_point35	0,011	0	28,573	0,003	0	5,661	10,216	44,464
depth_82.40mA_point36	0,034	0	28,495	0,001	0,008	5,789	10,311	44,638
depth_82.40mA_point37	0,01	0,125	54,558	0	0,116	0,004	47,025	101,838
depth_82.40mA_point38	0,008	0,159	54,629	0	0,195	0,003	46,682	101,676
depth_82.40mA_point39	0,006	0,18	54,49	0,001	0,157	0,002	47,156	101,992

Sample	Si(Mass%)	As(Mass%)	S(Mass%)	P(Mass%)	Ni(Mass%)	Mn(Mass%)	Fe(Mass%)	Zn(Mass%)	Cu(Mass%)	Total(Mass%)
depth_82.40mD_point1	0,224	0	40,193	0,009	0,338	0	58,327	0,019	0,018	99,128
depth_82.40mD_point2	0,026	0,055	55,174	0	0,058	0	47,778	0,018	0	103,109
depth_82.40mD_point3	0,032	0,011	40,69	0,007	0,321	0	60,432	0,012	0	101,505
depth_82.40mD_point4	0,309	0,029	54,607	0	0,028	0,005	45,74	0,011	0,01	100,739
depth_82.40mD_point5	0,064	0,837	53,919	0	0,149	0,004	46,747	0,02	0,033	101,773
depth_82.40mD_point6	0,084	0,062	54,9	0	0,213	0,008	47,183	0	0	102,45
depth_82.40mD_point7	0,02	0,068	54,307	0,001	0,074	0	47,105	0	0	101,575
depth_82.40mD_point8	0,087	0	34,872	0	0,001	4,63	9,02	53,844	0,014	102,468
depth_82.40mD_point9	0,079	0,153	55,182	0	0,087	0,043	46,764	0,606	0,004	102,918

Sample	Si(Mass%)	As(Mass%)	S(Mass%)	P(Mass%)	Ni(Mass%)	Mn(Mass%)	Fe(Mass%)	Total (Mass%)
depth_118.68m_1	0,091	0	37,521	0,001	0,007	56,754	6,42	100,794
depth_118.68m_2	0,128	0,003	37,693	0	0,002	57,019	6,459	101,304
depth_118.68m_3	0,132	0,002	37,452	0	0	57,385	5,609	100,58
depth_118.68m_4	0,09	0,04	40,248	0	0,334	0	59,701	100,413
depth_118.68m_5	0,118	0,035	40,407	0	0,309	0,004	60,257	101,13
depth_118.68m_6	0,067	0,012	40,822	0,002	0,311	0,005	59,887	101,106
depth_118.68m_7	0,328	0,048	40,526	0,004	0,281	0,005	59,95	101,142
depth_118.68m_8	0,033	0,183	54,866	0,004	0,087	0,008	46,578	101,759
depth_118.68m_9	0,061	0,062	55,369	0,001	0,033	0,096	47,419	103,041
depth_118.68m_10	0,057	0,18	55,209	0	0,112	0,005	47,063	102,626
depth_118.68m_11	0,108	0,162	54,924	0	0,092	0,001	46,623	101,91
depth_118.68m_12	0,101	0	37,647	0,001	0,007	56,624	5,875	100,255
depth_118.68m_13	0,156	0	37,398	0,002	0,004	56,751	5,941	100,252
depth_118.68m_14	0,066	0,149	55,37	0,005	0,119	0	46,803	102,512
depth_118.68m_15	0,11	0,193	55,031	0	0,113	0,005	47,102	102,554
depth_118.68m_16	0,058	0,089	55,434	0,001	0,041	0,017	47,227	102,867
depth_118.68m_17	0,06	0,134	55,258	0	0,011	0	46,87	102,333
depth_118.68m_18	0,062	0	37,691	0,001	0,004	56,626	5,981	100,365
depth_118.68m_19	0,114	0	37,735	0	0,001	57,139	5,903	100,892
depth_118.68m_20	0,147	0,03	40,922	0	0,238	0,083	60,397	101,817
depth_118.68m_21	0,099	0,021	40,584	0	0,261	0,081	59,901	100,947
depth_118.68m_22	0,084	0,049	40,608	0,002	0,347	0	59,936	101,026
depth_118.68m_23	0,226	0,013	37,678	0,002	0	57,197	5,873	100,989
depth_118.68m_24	0,364	0,15	55,464	0,001	0,067	0,006	47,169	103,221
depth_118.68m_25	0,082	0,085	55,067	0	0,019	0	47,302	102,555
depth_118.68m_26	0,175	0	29,17	0,004	0,002	5,446	9,5	44,297
depth_118.68m_27	0,167	0	28,703	0	0	5,227	9,397	43,494
depth_118.68m_28	0,105	0	28,745	0	0	5,629	9,691	44,17
depth_118.68m_29	0,12	0,259	54,483	0	0,087	0	47,04	101,989
depth_118.68m_30	0,047	0,114	55,432	0,001	0,042	0	46,857	102,493
depth_118.68m_31	0,28	0,038	54,806	0,001	0,014	0	47,037	102,176

Sample	Si(Mass%)	As(Mass%)	S(Mass%)	P(Mass%)	Ni(Mass%)	Mn(Mass%)	Fe(Mass%)	Total(Mass%)
depth_147.55m_1	0	0	40,014	0,003	0,403	0	59,564	99,984
depth_147.55m_2	0	0,034	40,454	0,002	0,346	0,009	59,852	100,697
depth_147.55m_3	0,044	0,004	40,673	0	0,385	0	59,234	100,34
depth_147.55m_4	0,092	0	40,547	0,002	0,439	0,006	59,315	100,401
depth_147.55m_5	0,001	0,15	54,35	0,004	0,135	0,004	46,992	101,636
depth_147.55m_6	0	0,133	54,283	0	0,075	0,002	46,828	101,321
depth_147.55m_7	0	0,191	54,386	0	0,086	0	47,023	101,686
depth_147.55m_8	0	0,019	54,366	0	0,08	0	46,895	101,36
depth_147.55m_9	0,02	0,142	54,475	0	0,142	0,01	47,197	101,986
depth_147.55m_10	0	0,134	54,212	0,001	0,084	0,004	46,996	101,431
depth_147.55m_11	0,033	0,073	54,251	0,046	0,066	0	46,761	101,23
depth_147.55m_12	0,029	0,061	54,605	0	0,197	0	46,838	101,73
depth_147.55m_13	0,003	0,125	54,772	0,006	0,144	0	47,318	102,368
depth_147.55m_14	0,007	0,333	54,966	0	0,849	0,008	46,437	102,6
depth_147.55m_15	0,004	0,12	54,894	0,002	0,121	0,01	47,123	102,274
depth_147.55m_16	0,012	0,026	40,206	0	0,348	0,012	59,905	100,509
depth_147.55m_17	0,001	0,02	40,452	0	0,337	0,014	60,077	100,901
depth_147.55m_18	0,016	0,111	55,095	0	0,056	0	46,911	102,189
depth_147.55m_19	0	0,163	54,77	0	0,124	0,001	46,612	101,67
depth_147.55m_20	0,002	0	28,126	0	0,054	4,831	8,57	41,583

depth_147.55m_21	0	0	28,158	0,002	0,016	5,002	8,322	41,5
depth_147.55m_22	0,009	0,013	39,772	0	0,364	0,006	58,455	98,619
depth_147.55m_23	0	0,08	54,697	0	0,03	0	47,069	101,876
depth_147.55m_24	0,018	0,055	54,356	0	0,043	0,004	46,86	101,336
depth_147.55m_25	0,035	0	28,677	0	0,015	4,896	8,832	42,455
depth_147.55m_26	0,033	0	28,278	0,002	0,015	5,167	8,824	42,319
depth_147.55m_27	0,032	0	29,437	0	0,023	4,961	8,699	43,152
depth_147.55m_28	0,011	0,062	54,957	0	0,089	0,004	46,751	101,874
depth_147.55m_29	0,045	0,034	40,88	0,002	0,354	0	59,248	100,563
depth_147.55m_30	0,048	0	40,552	0,001	0,361	0,009	59,698	100,669
depth_147.55m_31	0,037	0,018	40,624	0	0,369	0,002	59,783	100,833
depth_147.55m_32	0,014	0,016	40,453	0,006	0,229	0	60,242	100,96
depth_147.55m_33	0	0,031	40,289	0	0,221	0,045	60,138	100,724
depth_147.55m_34	0,002	0	27,944	0,002	0,043	4,768	8,619	41,378
depth_147.55m_35	0,005	0	28,403	0,001	0,012	5,083	8,524	42,028
depth_147.55m_36	0,008	0,032	40,508	0,007	0,347	0	60,39	101,292
depth_147.55m_37	0,002	0,168	54,889	0,001	0,098	0,011	47,217	102,386
depth_147.55m_38	0,012	0,031	40,391	0,008	0,398	0	60,18	101,02
depth_147.55m_39	0,043	0,167	54,865	0,005	0,126	0	46,804	102,01
depth_147.55m_40	0	0,147	55,051	0,003	0,101	0,004	47,394	102,7
depth_147.55m_41	0	0,139	54,462	0	0,137	0	46,653	101,391
depth_147.55m_42	5,14	0	0,193	0,085	0,027	0,329	1,106	6,88
depth_147.55m_43	0	0,155	54,546	0,001	0,114	0	46,921	101,737
depth_147.55m_44	0	0,115	54,764	0,005	0,155	0,014	47,382	102,435
depth_147.55m_45	0	0,164	54,561	0	0,136	0	46,831	101,692
depth_147.55m_46	0,01	0,115	54,312	0	0,116	0,008	46,623	101,184
depth_147.55m_47	0,014	0,077	54,774	0,002	0,035	0	47,307	102,209
depth_147.55m_48	0,003	0,003	32,628	0,055	0	0,015	33,023	65,727
depth_147.55m_49	0,1	0,038	40,36	0	0,195	0	60,33	101,023
depth_147.55m_50	0,022	0,121	55,527	0,002	0,069	0,002	47,246	102,989
depth_147.55m_51	0,009	0,153	54,723	0	0,134	0,003	47,214	102,236
depth_147.55m_52	0,013	0	40,576	0	0,391	0,002	60,225	101,207
depth_147.55m_53	0	0,098	55,098	0	0,06	0	47,225	102,481

Sample	Si(Mass%)	As(Mass%)	S(Mass%)	P(Mass%)	Ni(Mass%)	Mn(Mass%)	Fe(Mass%)	Total(Mass%)
depth_152.27m_1	0,0	0,0	40,8	0,0	0,2	0,0	60,7	101,8
depth_152.27m_2	0,0	0,0	40,5	0,0	0,2	0,0	60,2	100,9
depth_152.27m_3	0,0	0,0	40,1	0,0	0,2	0,0	59,8	100,1
depth_152.27m_4	0,0	0,0	40,3	0,0	0,5	0,0	59,9	100,7
depth_152.27m_5	0,0	0,0	37,6	0,0	0,0	59,3	3,9	100,8
depth_152.27m_6	0,0	0,0	40,5	0,0	0,3	0,0	59,9	100,7
depth_152.27m_7	0,0	0,2	54,9	0,0	0,1	0,0	47,1	102,4
depth_152.27m_8	0,0	0,2	55,1	0,0	0,2	0,0	47,3	102,7
depth_152.27m_9	0,0	0,2	55,1	0,0	0,2	0,0	47,0	102,5
depth_152.27m_10	0,0	0,0	37,4	0,0	0,0	57,9	5,2	100,5
depth_152.27m_11	0,0	0,0	37,5	0,0	0,0	59,1	4,3	100,9
depth_152.27m_12	0,0	0,4	54,4	0,0	0,2	0,1	46,5	101,7
depth_152.27m_13	0,0	0,0	37,2	0,0	0,0	58,8	4,3	100,3
depth_152.27m_14	0,0	0,2	54,8	0,0	0,1	0,0	47,1	102,3
depth_152.27m_15	0,0	0,4	54,5	0,0	0,1	0,0	46,7	101,8
depth_152.27m_16	0,0	0,0	54,7	0,0	0,2	0,0	46,8	101,7
depth_152.27m_17	0,0	0,1	54,8	0,0	0,2	0,0	47,3	102,3
depth_152.27m_18	0,0	0,1	54,6	0,0	0,2	0,0	46,7	101,7
depth_152.27m_19	0,0	0,1	40,4	0,0	0,2	0,0	60,5	101,2
depth_152.27m_20	0,0	0,0	40,6	0,0	0,2	0,0	60,5	101,3
depth_152.27m_21	0,0	0,0	55,1	0,0	0,1	0,0	47,4	102,7

Sample	Si(Mass%)	As(Mass%)	S(Mass%)	P(Mass%)	Ni(Mass%)	Mn(Mass%)	Fe(Mass%)	Total(Mass%)
depth_176.55m_1	0,092	0,074	54,911	0,002	0,062	0,005	47,02	102,166
depth_176.55m_2	0,076	0,075	54,804	0	0,059	0	47,12	102,134
depth_176.55m_3	0,093	0,087	54,875	0,004	0,059	0	46,718	101,836
depth_176.55m_4	0,164	0	37,383	0	0	56,854	5,791	100,192
depth_176.55m_5	0,084	0	37,493	0,001	0	56,789	5,965	100,332
depth_176.55m_6	0,169	0	37,292	0	0,011	57,255	5,765	100,492
depth_176.55m_7	0,025	0	29,184	0	0	6,668	11,445	47,322
depth_176.55m_8	0,036	0	29,313	0	0,006	6,636	11,221	47,212
depth_176.55m_9	0,044	0	28,48	0,002	0,006	5,734	10,11	44,376
depth_176.55m_10	0,05	0	28,538	0	0,014	5,715	10,163	44,48
depth_176.55m_11	0,142	0,117	54,785	0,001	0,085	0,004	47,051	102,185
depth_176.55m_12	0,737	0	30,36	0	0	6,218	10,82	48,135
depth_176.55m_13	0,111	0	28,694	0	0,009	5,774	10,432	45,02
depth_176.55m_14	0,041	0,106	54,84	0	0,013	0	47,105	102,105
depth_176.55m_15	0,083	0	29,05	0	0	6,258	11,199	46,59
depth_176.55m_16	0,075	0	29,069	0,002	0,007	6,323	11,291	46,767
depth_176.55m_17	0,067	0,102	54,66	0	0,04	0	46,798	101,667
depth_176.55m_18	0,091	0,087	54,466	0	0,047	0,006	46,875	101,572
depth_176.55m_19	0,095	0,126	55,01	0,001	0,026	0	47,269	102,527
depth_176.55m_20	0,089	0	29,202	0,004	0	6,445	12,003	47,743
depth_176.55m_21	0,087	0,001	28,995	0	0	6,311	11,782	47,176
depth_176.55m_22	0,009	0	29,498	0	0,02	9,365	10,599	49,491
depth_176.55m_23	0,014	0	29,285	0	0	7,842	11,341	48,482
depth_176.55m_24	0,13	0,089	54,282	0,004	0,083	0,056	46,551	101,195
depth_176.55m_25	0,038	0	29,04	0	0,022	7,04	10,883	47,023
depth_176.55m_26	0,039	0,087	54,247	0	0,052	0	46,454	100,879
depth_176.55m_27	0,442	0,072	54,29	0	0,055	0,006	46,964	101,829
depth_176.55m_28	0,284	0	32,553	0,059	0,006	0,012	33,334	66,248
depth_176.55m_29	2,11	0,018	30,803	0,064	0,002	0,058	31,911	64,966

Sample	Si(Mass%)	As(Mass%)	S(Mass%)	P(Mass%)	Ni(Mass%)	Mn(Mass%)	Fe(Mass%)	Zn(Mass%)	Cu(Mass%)	Total(Mass%)
depth_204.40m_1	0,048	0,016	40,403	0,005	0,289	0,004	59,707	0,053	0,027	100,552
depth_204.40m_2	0,059	0	40,642	0	0,305	0	59,936	0,024	0,029	100,995
depth_204.40m_3	0,064	0	36,037	0,067	0	0	30,903	0,095	34,561	101,727
depth_204.40m_4	0,058	0,001	36,038	0,046	0	0,23	30,817	0,075	34,349	101,614
depth_204.40m_5	0,036	0	37,844	0,001	0,01	57,27	5,856	0,008	0,153	101,178
depth_204.40m_6	0,032	0	37,656	0	0,004	57,047	5,884	0,007	0,061	100,691
depth_204.40m_7	0,034	0	37,519	0,001	0	57,423	5,484	0,035	0,008	100,504
depth_204.40m_8	0,056	0	37,454	0	0	56,748	6,151	0,007	0,005	100,421
depth_204.40m_9	0,047	0	37,588	0	0,012	56,073	6,779	0,028	0	100,527
depth_204.40m_10	0,027	0	40,674	0,003	0,278	0	59,971	0,03	0,107	101,09
depth_204.40m_11	0,008	0	35,835	0,054	0	0,017	30,876	0,077	34,389	101,256
depth_204.40m_12	0,067	0,023	40,348	0,005	0,303	0,008	58,778	0,039	0,006	99,577
depth_204.40m_13	0,057	0,02	40,5	0,001	0,297	0	58,941	0,011	0,007	99,834
depth_204.40m_14	0,027	0,015	40,623	0	0,34	0,012	59,94	0,026	0	100,983
depth_204.40m_15	0,043	0,01	40,848	0,003	0,332	0,012	59,873	0,011	0	101,132
depth_204.40m_16	0,046	0	40,53	0,007	0,33	0,017	59,706	0,022	0	100,658
depth_204.40m_17	0,089	0,004	35,885	0,062	0	0,017	30,87	0,071	34,246	101,244
depth_204.40m_18	0,063	0	35,947	0,063	0	0,02	30,831	0,051	34,312	101,287
depth_204.40m_19	0,051	0,003	35,992	0,062	0	0,087	30,292	0,069	34,134	100,69

depth_204.40m_20	0,036	0	35,907	0,05	0	0,072	29,992	0,048	34,101	100,206
depth_204.40m_21	0,037	0,01	36,017	0,066	0,002	0,013	30,855	0,084	34,456	101,54
depth_204.40m_22	0,039	0	35,955	0,069	0,002	0,015	30,65	0,069	34,451	101,25
depth_204.40m_23	0,081	0	35,796	0,061	0	0,019	30,955	0,055	34,316	101,283
depth_204.40m_24	0,046	0,033	40,375	0,005	0,317	0,001	59,88	0,022	0,072	100,751
Sample	**Si(Mass%)**	**As(Mass%)**	**S(Mass%)**	**P(Mass%)**	**Ni(Mass%)**	**Mn(Mass%)**	**Fe(Mass%)**	**Zn(Mass%)**	**Cu(Mass%)**	**Total**
depth_237.30m_1	0,096	0,011	39,821	0,004	0,564	0,014	59,571	0,027	0	100,108
depth_237.30m_2	0,062	0,023	39,76	0	0,539	0	60,062	0,032	0,068	100,546
depth_237.30m_3	1,213	0,008	33,774	0,044	0	0,005	28,761	0,066	32,809	96,68
depth_237.30m_4	0,29	0	34,407	0,009	0,01	4,678	7,526	55,743	0	102,663
depth_237.30m_5	0,557	0	34,507	0,005	0	4,77	7,418	55,489	0	102,746
depth_237.30m_6	0,06	0,026	39,581	0,002	0,637	0	60,082	0,024	0	100,412
depth_237.30m_7	0,085	0	39,737	0	0,64	0,003	59,965	0,002	0,001	100,433
depth_237.30m_8	0,252	0	34,508	0	0,001	4,037	7,77	56,474	0,003	103,045
depth_237.30m_9	0,079	0,01	39,553	0	0,629	0,004	60,311	0,011	0	100,597
depth_237.30m_10	0,146	0	33,711	0	35,538	0,001	30,796	0	0	100,192
depth_237.30m_11	0,099	0	33,755	0	35,867	0,004	30,22	0	0	99,945
depth_237.30m_12	0,143	0	33,449	0,009	35,683	0	30,917	0,006	0	100,207
depth_237.30m_13	0,081	0,024	39,672	0,003	0,699	0,008	60,282	0,014	0	100,783
depth_237.30m_14	0,473	0	33,948	0	0,014	4,075	8,224	55,443	0,021	102,198
depth_237.30m_15	0,177	0,021	39,776	0	0,631	0	60,039	0,02	0	100,664
depth_237.30m_16	0,424	0,011	34,511	0	0,017	4,052	7,875	55,835	0,057	102,782
depth_237.30m_17	0,298	0,033	39,493	0	0,607	0,005	59,731	0,038	0	100,205
depth_237.30m_18	0,152	0	33,806	0	35,594	0,008	30,996	0	0	100,556
depth_237.30m_19	0,207	0	34,715	0	0,713	4,238	7,944	55,499	0	103,316
depth_237.30m_20	0,327	0	34,449	0,005	0,267	4,135	7,65	55,822	0,096	102,751

Sample	**Si(Mass%)**	**As(Mass%)**	**S(Mass%)**	**P(Mass%)**	**Ni(Mass%)**	**Mn(Mass%)**	**Fe(Mass%)**	**Total(Mass%)**
depth_272.80m_1	0,025	0,009	40,849	0	0,705	0	60,45	102,038
depth_272.80m_2	0,12	0,031	40,292	0,006	0,706	0,004	60,802	101,961
depth_272.80m_3	0,053	0	28,768	0	0,009	5,511	9,61	43,951
depth_272.80m_4	0,129	0	27,992	0,004	0,009	5,186	9,604	42,924

Sample	**Si(Mass%)**	**As(Mass%)**	**S(Mass%)**	**P(Mass%)**	**Ni(Mass%)**	**Mn(Mass%)**	**Fe(Mass%)**	**Zn(Mass%)**	**Cu(Mass%)**	**Total (Mass%)**
depth_272.80m_5	0,008	0	33,399	0,001	35,955	0	30,942	0,021	0	100,326
depth_272.80m_6	0,004	0	33,529	0	35,746	0	31,119	0	0	100,398
depth_272.80m_7	0,008	0,054	39,798	0	0,342	0,009	60,31	0,044	0	100,565
depth_272.80m_8	0,005	0	40,146	0,005	0,319	0	60,045	0,029	0,008	100,557
depth_272.80m_9	0,003	0	39,267	0	0,671	0	60,51	0,013	0,008	100,472
depth_272.80m_10	0,015	0	39,432	0,003	0,634	0,004	60,234	0,037	0	100,359
depth_272.80m_11	0,086	0,028	39,201	0	0,352	0,005	60,042	0,109	0	99,823
depth_272.80m_12	0,041	0	39,451	0	0,328	0,005	60,384	0,227	0	100,436
depth_272.80m_13	0	0	34,238	0,001	0,017	4,879	8,804	54,384	0,02	102,343
depth_272.80m_14	0	0,018	39,91	0	0,36	0,006	59,733	0,301	0	100,328
depth_272.80m_15	0,011	0,025	39,449	0,004	0,631	0,042	60	1,088	0	101,25
depth_272.80m_16	0	0	34,359	0,001	0,021	4,83	8,581	54,998	0	102,79
depth_272.80m_17	0,004	0,037	39,671	0,003	0,547	0,038	60,03	0,812	0	101,142
depth_272.80m_18	0	0	34,552	0	0,004	4,733	8,316	55,443	0	103,048
depth_272.80m_19	0	0,024	39,497	0	0,641	0,05	60,164	0,883	0	101,259
depth_272.80m_20	0,011	0	34,539	0,002	0,015	4,563	8,176	55,785	0	103,091
depth_272.80m_21	0,004	0,026	39,52	0	0,634	0,021	60,189	0,408	0	100,802
depth_272.80m_22	0,01	0	34,972	0	0,021	4,625	8,309	55,744	0,018	103,699
depth_272.80m_23	0,014	0,029	40,122	0	0,267	0,01	60,14	0,26	0	100,842
depth_272.80m_24	0	0	34,181	0	0,002	3,942	8,01	56,595	0	102,73
depth_272.80m_25	0	0,033	39,674	0	0,469	0,043	60,043	0,922	0	101,184
depth_272.80m_26	0	0	34,286	0,004	0	3,456	6,755	58,61	0,007	103,118
depth_272.80m_27	0	0	34,273	0	0	3,814	7,023	57,752	0	102,862
depth_272.80m_28	0,018	0,043	40,104	0,006	0,041	0,007	59,917	0,046	0,739	100,921
depth_272.80m_29	0,012	0,026	35,48	0,058	0,007	0	30,972	0	34,596	101,151
depth_272.80m_30	0,006	0	34,818	0,002	0,002	5,382	10,061	51,967	0,654	102,892
depth_272.80m_31	0,012	0	34,598	0,012	0,002	5,336	9,944	52,48	0,575	102,959
depth_272.80m_32	0,011	0	35,436	0,068	0	0,02	30,877	0,243	34,565	101,22
depth_272.80m_33	0,007	0	35,381	0,056	0	0,006	30,98	0,058	34,716	101,204

Table S4. *Abundance of minerals within the sampled depths, where red asterisks represent dominating mineralogy, black asterisks abundant minerals and asterisks within brackets occasional abundance, and where Py=pyrite, Pyh=pyrrhotite, Abd=alabandite, Cpy=chalcopyrite, Pn=pentlandite, Sl=sphalerite, Ap=apatite, Phl=phlogopite, Qz=quartz, Or=orthoclase*

Sample depth (m)	Py	Pyh	Abd	Cpy	Pn	Sl	Ap	Phl	Qz	Or
82,4	*	*				*			*	
115,4									*	
118,68	*	*	*							
147,55	*	*	(*)			*		*	*	
152,27	*	*	*						*	
155,9										
176,55	*									*
186,15	*									*
204,4		*	(*)	*						
237,3		*			*					
272,8		*		*	*	*				

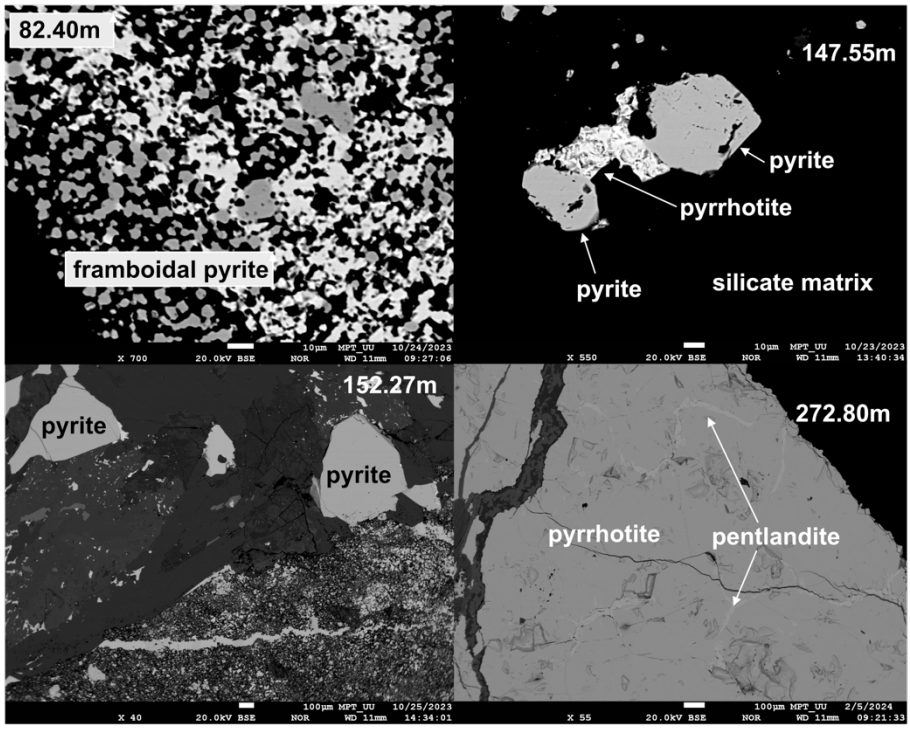

Fig.S1. *Left panel: Image of euhedral pyrites with anhedral pyrrhotites at sample depth 147.55m. Right panel: Pyrrhotites with pentlandite crack infillings at sample depth 272.80m.*

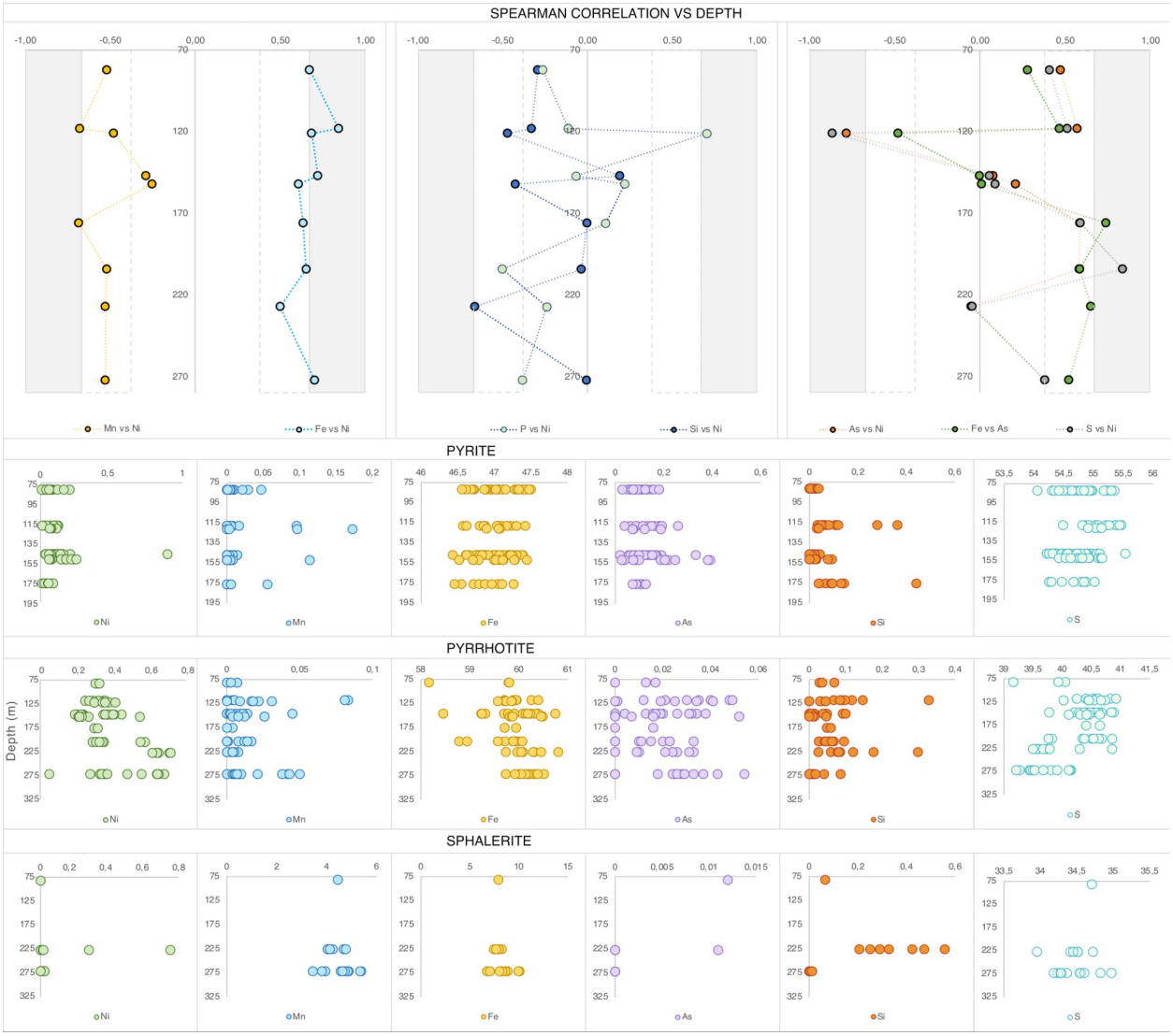

Fig. S2. *EPMA elemental spot analyses. Upper panel: Spearman correlations as a function of depth where the gray area represents a very strong correlation and the dotted vertical line marks the threshold for moderate correlation. Lower panels show the element (wt%) variation in selected sulfides as a function of depth. Note the different x-axis scales.*

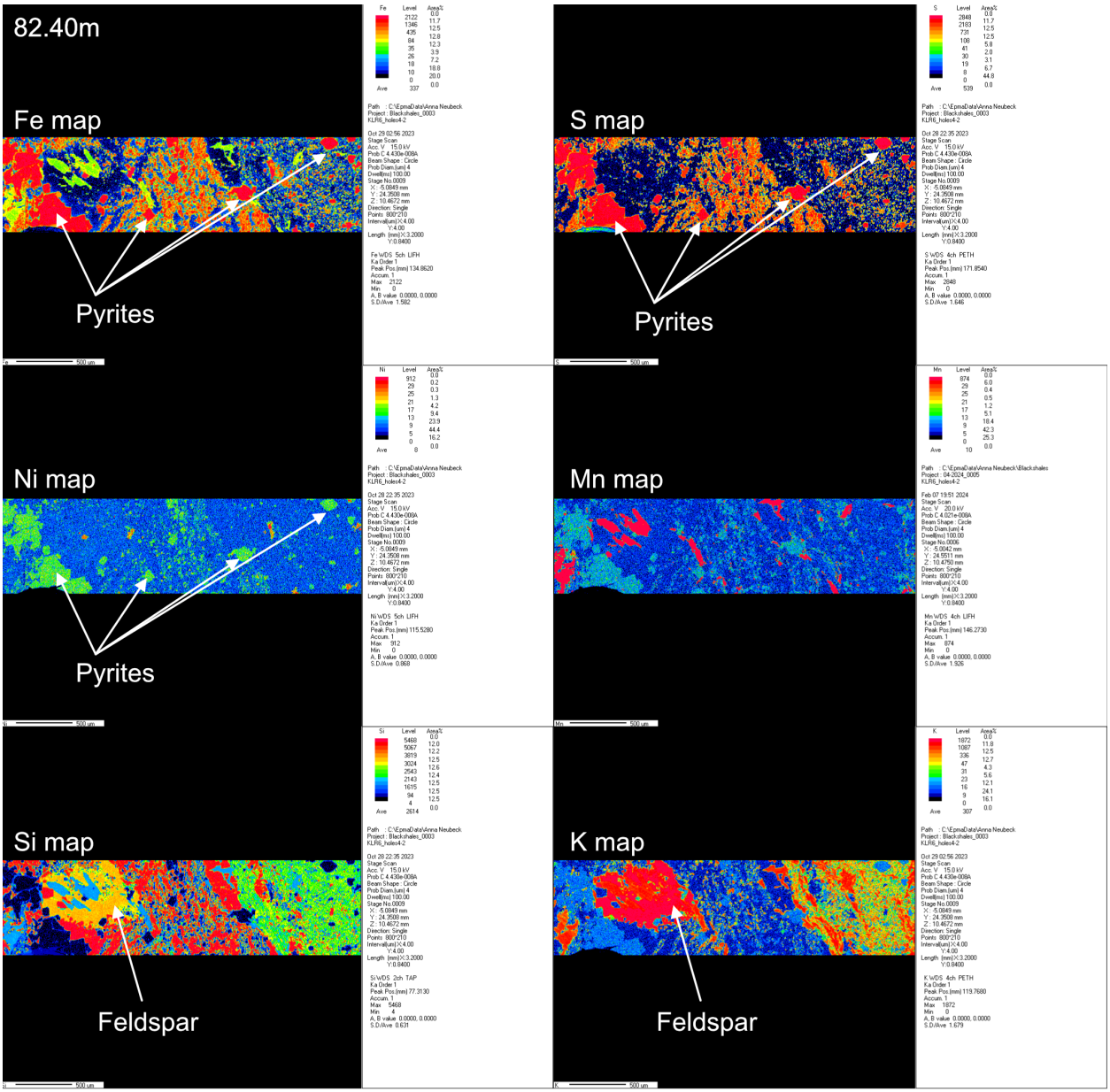

Fig. S3. *EPMA elemental maps for sample 82,40m.*

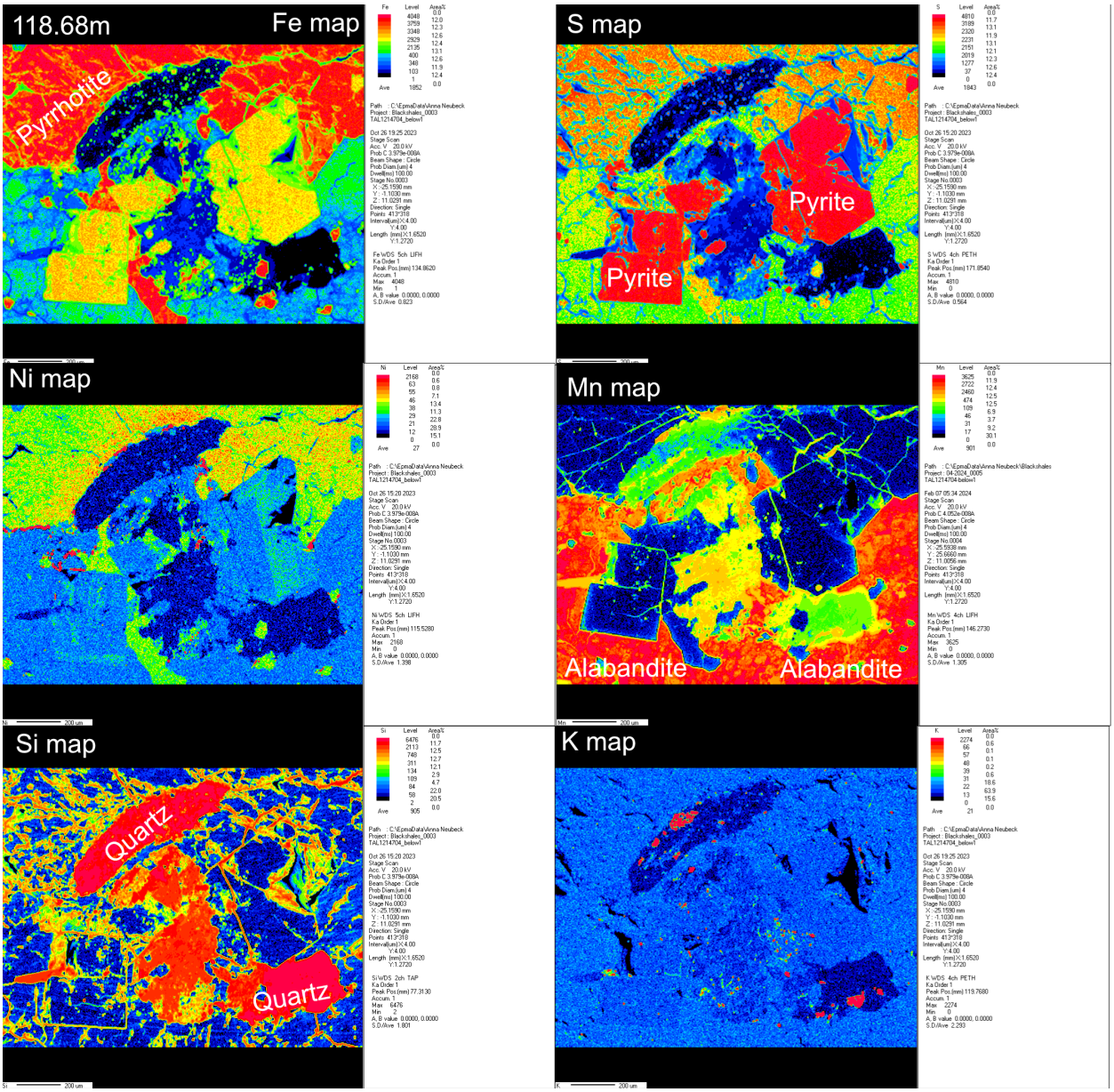

Fig. S4. *EPMA elemental maps for sample 118,68m.*

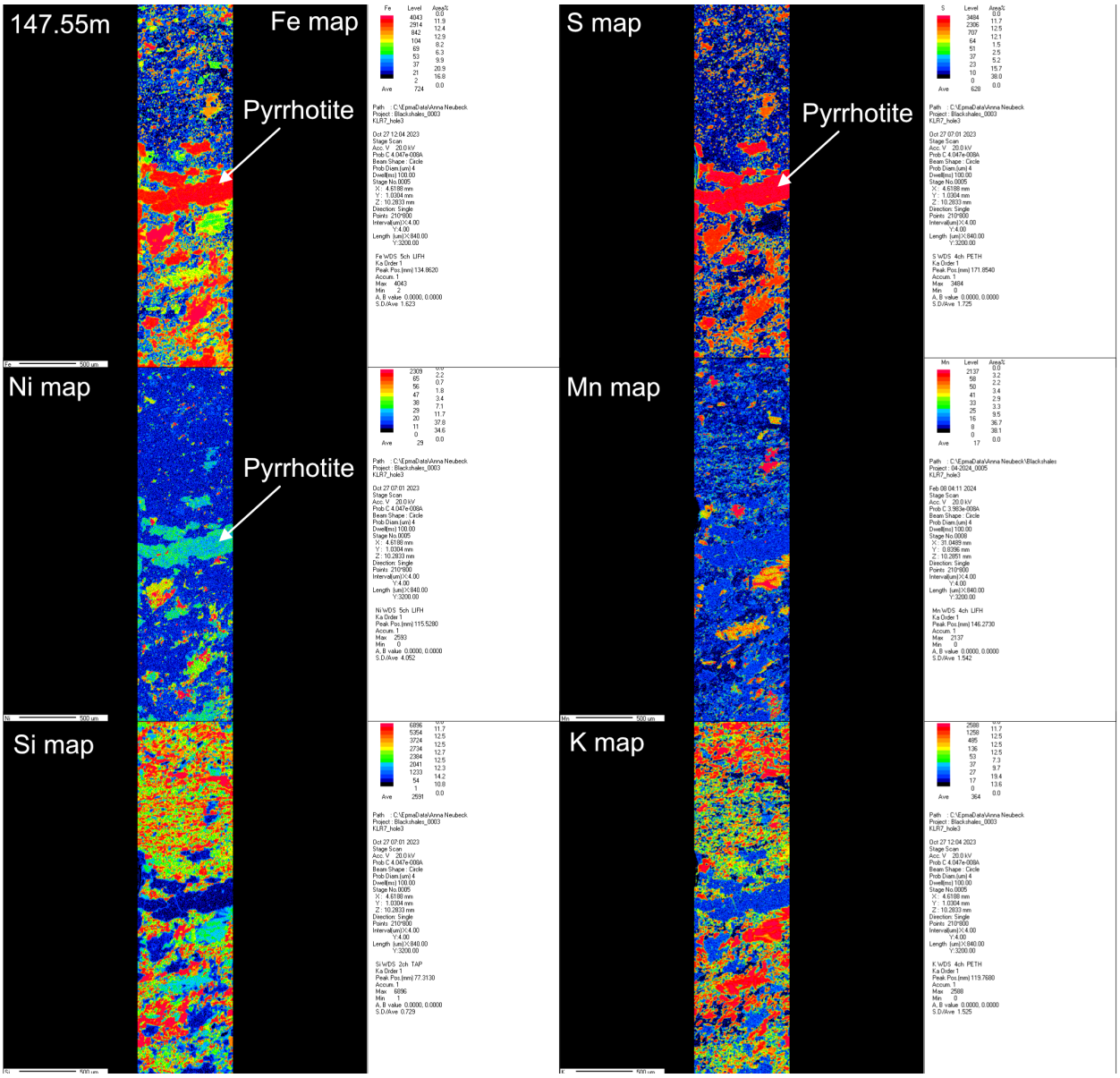

Fig. S5. *EPMA elemental maps for sample 147,55m.*

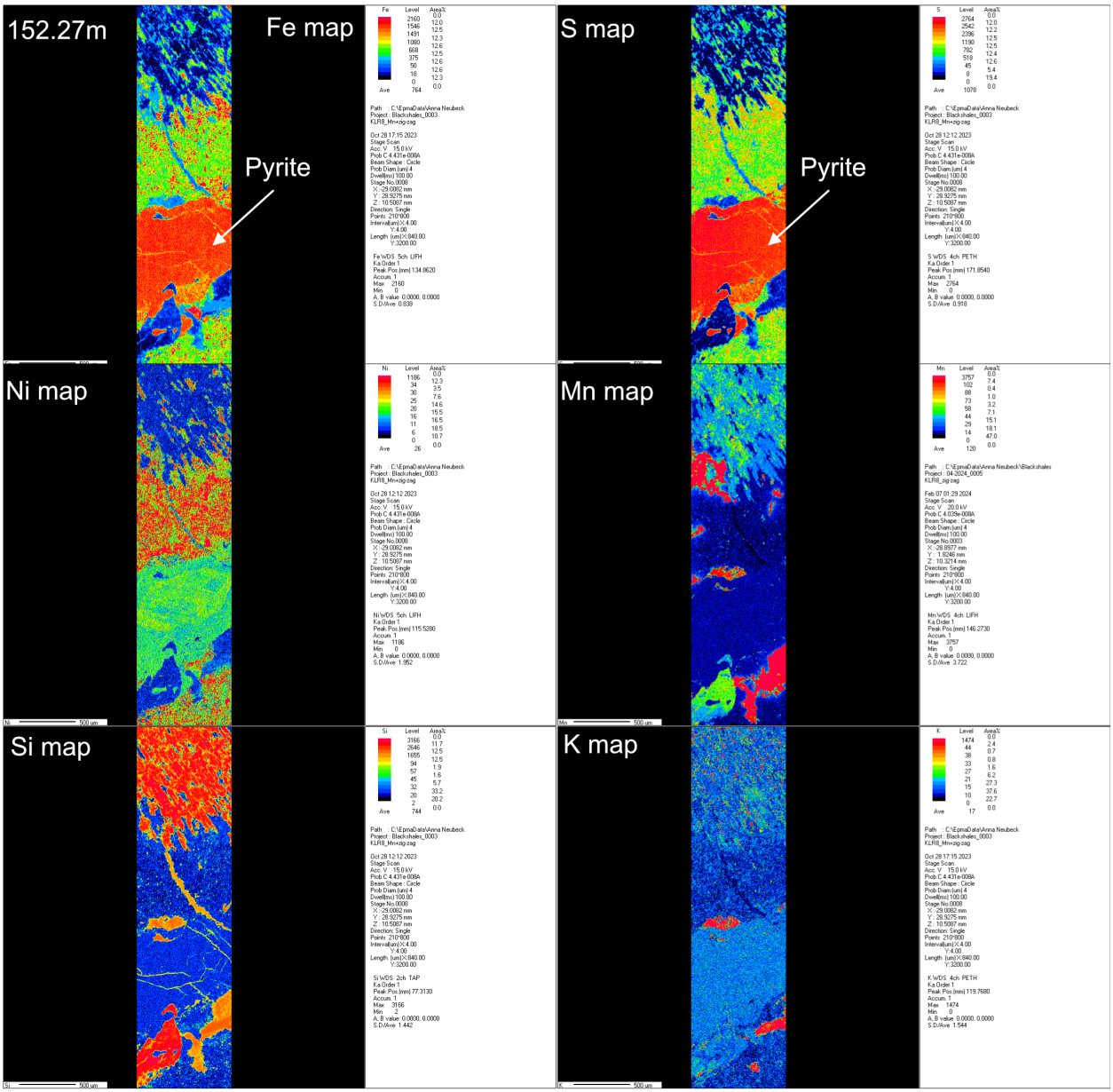

Fig. S6. *EPMA elemental maps for sample 152,27m.*

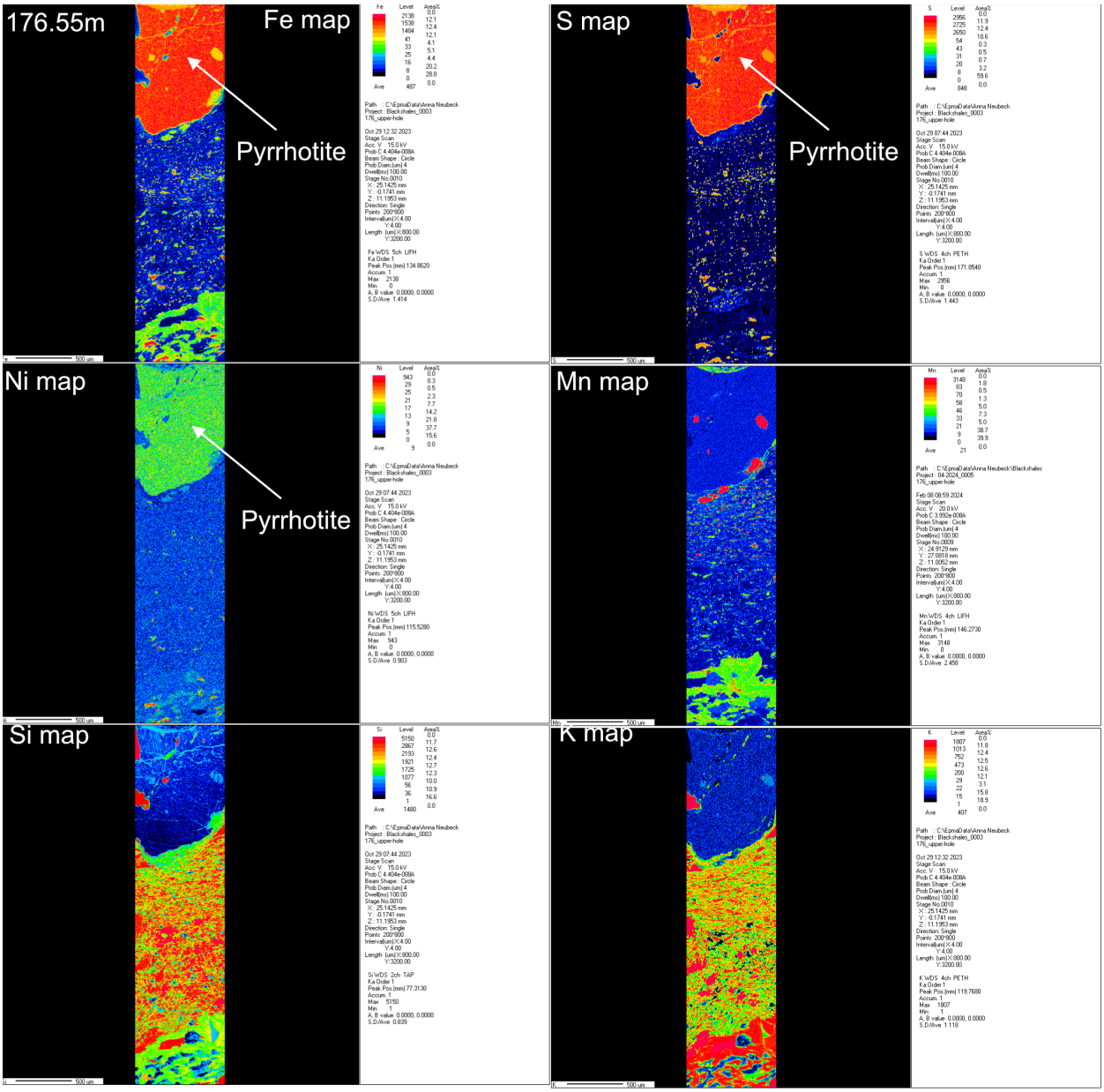

Fig. S7. *EPMA elemental maps for sample 176,55m.*

Table S5. *LA-ICP-MS, measured isotopes and dwell times*

Element	Q1 (m/z)	Q2 (m/z)	Dwell time (in ns)	
session			251117	251118
Na	23	23	2	2
Mg	24	24	2	2
Al	27	27	2	2
Si	28	60	2	2
P	31	47	2	2
S	32	64	2	2
K	39	39	2	2
Ca	44	60	2	2
Sc	45	61	5	5
Ti	48	80	2	2
V	51	83	2	2
Cr	52	52	5	5
Mn	55	55	2	2
Fe	56	72	2	2
Co	59	59	5	5
Ni	60	60	5	5
Cu	63	63	2	2
Zn	66	66	2	2
Ga	69	69	2	2
Ge	72	88	2	2
As	75	91	2	2
Se	80	96	2	2
Rb	**85**	**85**	**5**	**10**
Sr	**86**	**102**	**50**	**75**
Sr	86	103	2	2
Sr	**87**	**103**	**60**	**90**
Y	89	105	5	5
Zr	90	122	2	2
Nb	93	125	2	2
Mo	95	95	2	2
Rh	103	103	5	5
Pd	105	105	5	5
Pd	106	106	5	5
Ag	107	107	2	2
Cd	111	111	2	2

In	115	115	2	2
Sn	118	118	2	2
Sb	121	137	2	2
Te	128	128	2	2
Ba	138	154	5	5
La	139	155	5	5
Ce	140	156	5	5
Pr	141	157	5	5
Nd	146	162	5	5
Sm	147	163	5	5
Eu	153	169	5	5
Gd	157	173	5	5
Tb	159	175	5	5
Dy	163	179	5	5
Ho	165	181	5	5
Er	166	182	5	5
Tm	169	185	5	5
Yb	172	188	5	5
Lu	175	191	5	5
Au	197	197	5	5
Hg	202	202	5	5
Tl	205	205	2	2
Pb	208	208	2	2
U	238	254	2	2

***Table S5**. Variation of isotopic values of sulfides with depth*

Depth (m)	δ34S	± ‰	Mineral
82,4	-9,12	0,05	pyrite
82,4	-13,86	0,06	pyrite
82,4	-12,40	0,05	pyrite
82,4	-7,02	0,05	pyrite
82,4	-7,39	0,05	pyrite
82,4	-12,02	0,05	pyrite
82,4	-12,12	0,05	pyrite
82,4	-12,24	0,05	pyrite
82,4	-2,95	0,05	pyrite
82,4	-1,13	0,05	pyrite
82,4	-0,93	0,05	pyrite
82,4	-0,92	0,05	pyrite
82,4	-1,43	0,05	pyrite
118,68	-2,69	0,05	pyrite
118,68	-2,44	0,05	pyrite
118,68	-2,89	0,05	pyrite
118,68	-2,94	0,05	pyrite
118,68	-6,18	0,05	pyrite
118,68	-6,80	0,06	pyrite
118,68	-6,32	0,05	pyrite
118,68	-5,96	0,06	pyrite
118,68	-5,88	0,05	pyrite
118,68	-6,21	0,06	pyrite
118,68	-5,74	0,05	pyrite
118,68	-6,50	0,05	pyrite
118,68	-5,88	0,05	pyrite
118,68	-5,80	0,05	pyrite
118,68	-6,72	0,04	chalcopyrite
118,68	-1,97	0,05	chalcopyrite
118,68	-3,02	0,05	pyrrhotite
118,68	-4,06	0,05	pyrrhotite

***Table S7**. Variation of $\delta^{13}C$ with depth*

	Depth	**δ13C vs VPDB ‰**	**cal C%**
Sulfides	82,4	-25,10	2,50
	121	-26,1	0,9
	147,55	-26,4	9,3
	152,27	-26,7	2,5
	176,55	-25,9	4,4
-0,45	272,8	-24,6	0,9
Silicates	82,4	-26,61	10,14
	121	-26,56	7,79
	147,55	-26,37	15,05
	152,27	-25,94	42,93
	176,55	-25,95	16,00
0,25	272,8	-25,17	13,14

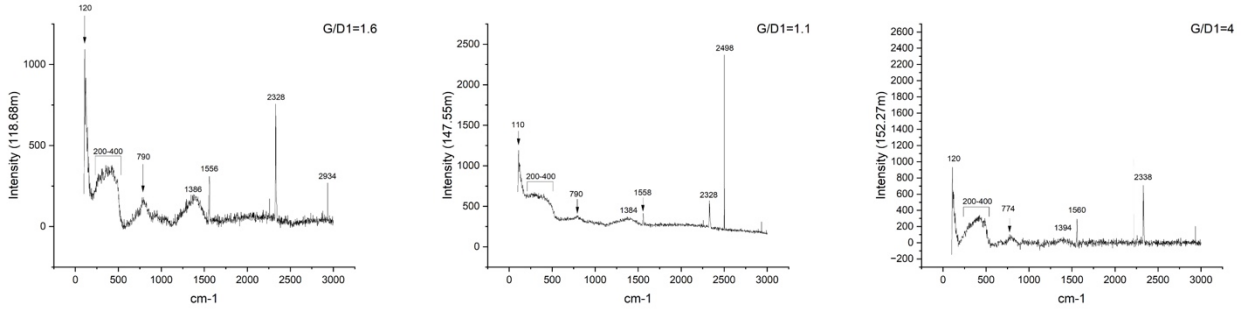

Fig. S8. *Raman plots of three selected drill core depths (118.68, 147.55 and 152.27m), showing the Raman spectra of the sulfides (200-400cm^{-1}, Lara et al. 2014), Si-O-Si stretching vibrational bands (~790 cm^{-}, Neuville et al. 2021[1]), atmospheric N2 (~2300 cm^{-1}) and mature carbonaceous matter (~1400, ~1560 and ~2900 cm^{-1}). Added is also the G/D1 peak ratio based on the ~1400cm^{-1} vs ~1560 cm^{-1} peak intensity ratio. The extra peak at ~120 cm^{-1} is due to stray light.*

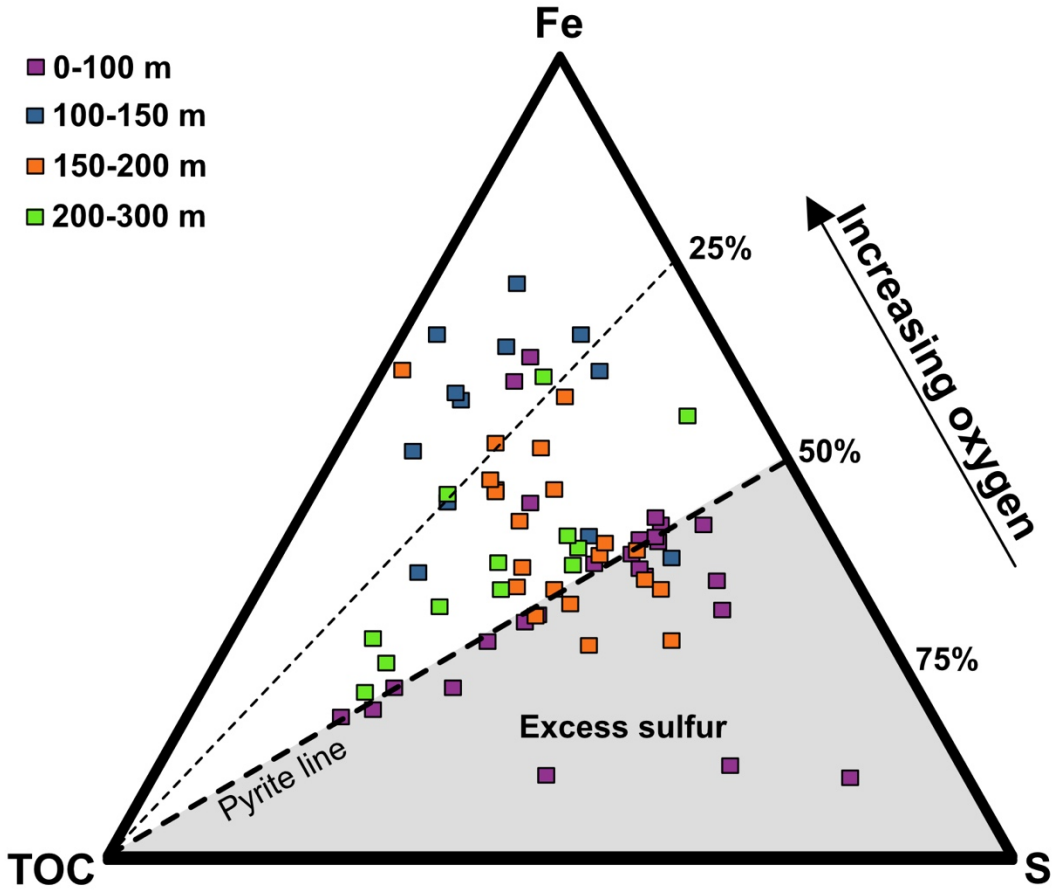

Fig.S9 Sulfurization

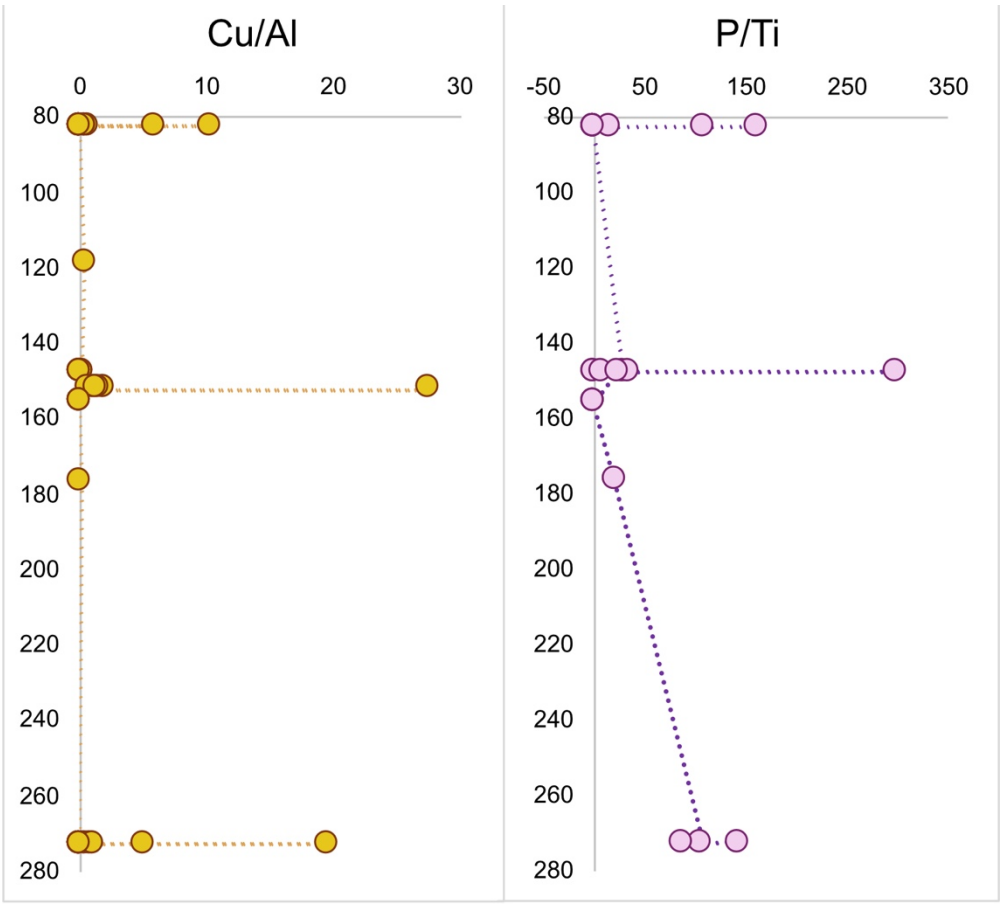

Fig.S10. *Paleoproductivity proxies Cu/Al (left panel) and P/Ti (right panel) indicative of a productivity shift at approximatelt 155m depth.*

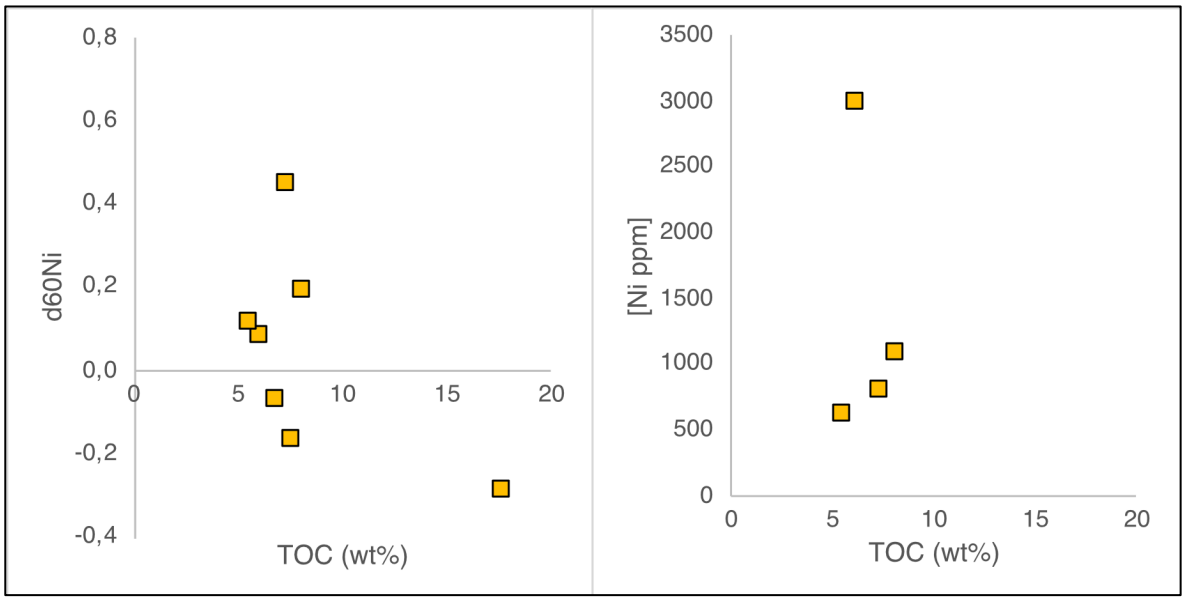

***Fig. S11**. Correlation between TOC and $d^{60}Ni$ (left panel) and [Ni] ppm (right panel).*

Neuville, D.R. *et al.* (2021). Structure Characterizations and Molecular Dynamics Simulations of Melt, Glass, and Glass Fibers. In: Li, H. (eds) Fiberglass Science and Technology. Springer, Cham. https://doi.org/10.1007/978-3-030-72200-5_2

Lara, R.H., Monroy, M.G., Mallet, M. *et al.* An experimental study of iron sulfides weathering under simulated calcareous soil conditions. *Environ Earth Sci* **73**, 1849–1869 (2015). https://doi.org/10.1007/s12665-014-3540-y